VYSOKÉ UČENÍ TECHNICKÉ V BRNĚ

Středoevropský technologický institut VUT

DIZERTAČNÍ PRÁCE

Brno, 2024 Mgr. Michela Sanna, M.Sc.

VYSOKÉ UČENÍ TECHNICKÉ V BRNĚ

BRNO UNIVERSITY OF TECHNOLOGY

STŘEDOEVROPSKÝ TECHNOLOGICKÝ INSTITUT VUT

CENTRAL EUROPEAN INSTITUTE OF TECHNOLOGY BUT

2D MATERIÁLY PRO ELEKTROKATALÝZU A PŘÍPRAVU VODÍKU JAKO ČISTÉHO ZDROJE ENERGIE

2D MATERIALS FOR ELECTROCATALYSIS AND HYDROGEN GENERATION AS CLEAN ENERGY SOURCE

DIZERTAČNÍ PRÁCE
DOCTORAL THESIS

AUTOR PRÁCE
AUTHOR

Mgr. Michela Sanna, M.Sc.

ŠKOLITEL
SUPERVISOR

prof. RNDr. Martin Pumera, Ph.D.

BRNO 2024

Acknowledgments

I wish to express my sincere gratitude to my PhD supervisor, Prof. Martin Pumera, for his guidance and support throughout my PhD journey. Thank you for giving me the opportunity to work with exceptional scientists and utilize cutting-edge facilities here at CEITEC. I learned many valuable lessons during these four years that will stay with me throughout my lifetime. In a society that prioritizes success above all else, you have shown me that failure and rejection are inevitable parts of the journey, and without attempting, neither failure nor success can be realized. Thank you for believing in my potential and trusting my capabilities.

I would like to thank Dr. Dogukan Apaydin and the group of Molecular Materials Chemistry at the Technical University of Wien for warmly welcoming me to their research group for three months. I enjoyed the time spent in Wien working with you, and I hope to collaborate or meet with you again in the future.

I want to acknowledge Dr. Siowwoon Ng for her mentorship during my PhD. I am deeply thankful for all the scientific discussions over good coffee and all the valuable memories we shared. Thank you for giving me direction when I felt lost and always believing in me, I will be forever grateful for it.

I cannot forget to mention my precious PhD buddies, Katarina and Cagatay. Thank you for all the crazy moments we went through together, all the laughs and challenges we faced during these years. You were a fundamental part of my PhD and I hope our friendship will continue for a long time. I am grateful to have found such amazing friends and shared this part of my life with you.

Thanks also to all the fantastic people I met in these four years, starting with my colleagues at the Future Energy and Innovation Lab and CEITEC, and continuing with all the amazing friends I encountered in Brno, particularly my Italian buddies. All of you contribute to making this journey easier and more enjoyable from different points of view.

I want to thank my family for all the support I constantly get. It is not easy to be far from home, but I know that you are all proud of me and that I will always have you on my side. A special thanks to my husband, Alessio, who has shared with me the joy and, more often, the struggles of the PhD life. I love you, and I will not be here without your love and support.

I would like to thank all my lifelong friends, the kind of friends that maybe you do not manage to speak with so often anymore, but you know they will always be there for you when you need them most. In particular, my soul mate Federica will always have her own place in my acknowledgments. I am grateful to have you in my life and to share with you another key moment of my life. You have always been there for me and you will always be.

Last but not least, I would like to thank my beloved Vipers teammates for the incredible two years we spent playing together. Your support has been invaluable, and I truly believe it played a significant role in preserving my mental sanity... or what is left of it, anyway.

Bibliographic citation

SANNA, M. 2D materials for electrocatalysis and hydrogen generation as clean energy source, Brno 2024, Brno University of Technology, Central European Institute of Technology BUT, 122 p., Supervisor: prof. RNDr. Martin Pumera, Ph.D..

DECLARATION

I certify, that I performed dissertation work independently, under the supervision of prof. RNDr. Martin Pumera, Ph.D.. All technical literature and other information sources presented in this work are properly cited in the text and listed in the reference list.

Brno 2024 Mgr. Michela Sanna, M.Sc.

Table of Contents

Author publications and other outputs 1

Abstract 4

Organization of the Thesis 8

1. Objectives of the Thesis 9

2. Introduction to the challenges 11

3. Literature Review 14

3.1. Theory and background 14

3.1.1. Hydrogen as energy source 14

3.1.2. Water electrolysis 16

3.1.3. Photoelectrochemical hydrogen generation 17

3.2. State of the art 19

3.2.1. 2D layered materials for electrochemical hydrogen production 19

3.2.2. Photoelectrochemical hydrogen production 23

3.2.3. Additive manufacturing 24

4. Methods 27

4.1. Materials and synthesis 27

4.1.1. Fluorination of MAX phases 28

4.1.2. Preparation of 3D-printed carbon electrode 28

4.1.3. Atomic layer deposition of TiO_2, SiO_2, and Al_2O_3 29

4.2. Materials characterization 31

4.2.1 Morphology and composition 31

4.2.2 Optical characterization 33

4.3. Electrochemical measurements 34

4.3.1. Electrode preparation 35

4.3.2. Photoelectrochemical measurements 35

5. Layered transition metal selenophosphites for visible light photoelectrochemical production of hydrogen 38

5.1. Motivation for the study 38

5.2. Paper conclusion 39

5.3. Author contribution 39

6. Fluorinated MAX phases for photoelectrochemical hydrogen evolution 45

6.1. Motivation for the study 45
6.2. Paper conclusion 46
6.3. Author contribution 47
7. The unexpected photoelectrochemical activity of MAX phases: the role of oxide impurities 57
7.1. Motivation for the study 57
7.2. Paper conclusion 57
7.3. Author contribution 58
8. Heterolayered carbon allotrope architectonics via multi-material 3D printing for advanced electrochemical devices 71
8.1. Motivation for the study 71
8.2. Paper conclusion 72
8.3. Author contribution 72
9. Engineering 3D-printed carbon structures with atomic layer deposition coatings as photoelectrocatalysts for water splitting 87
9.1. Motivation for the study 87
9.2. Paper conclusion 88
9.3. Author contribution 88
10. Conclusions 98
11. References 102

Author publications and other outputs

Publications

Included in the thesis

1. **Sanna, M.**; Novčić, K.A.; Ng, S.; Černý, M.; Pumera, M., The unexpected photoelectrochemical activity of MAX phases: the role of oxide impurities, *J. Mater. Chem. A*, **2023**,11, 3080-3090, **IF 11.9**;
2. **Sanna, M**.; Ng, S.; Vaghasiya, J. V.; Pumera, M. Fluorinated MAX Phases for Photoelectrochemical Hydrogen Evolution. *ACS Sustain. Chem. Eng.* **2022**, *10* (8), 2793–2801, **IF 9.2**;
3. **Sanna, M**.; Ng, S.; Pumera, M. Layered Transition Metal Selenophosphites for Visible Light Photoelectrochemical Production of Hydrogen. Electrochem. Commun. **2021**, 129 (May), 107077, **IF 5.4**;
4. Ng, S.; **Sanna, M.**; Redondo, E.; Pumera, M., Engineering 3D-printed carbon structures with atomic layer deposition coatings as photoelectrocatalysts for water splitting, ***J. Mater. Chem. A***, **2024**,**12**, 396-404, **IF 11.9**;
5. Palacios-Corella, M.; **Sanna, M.**; Muñoz, J.; Ghosh, K.; Wert, S.; Pumera, M., Heterolayered carbon allotrope architectonics via multi-material 3D printing for advanced electrochemical devices, *Virtual and Physical Prototyping*, **2023**, 18:1, **IF 10.6**;

Not included in the thesis

6. Nittoor-Veedu, R.; Ng, S.; **Sanna, M.**; Pumera, M., 2D Methyl Germanane Enhanced 3D Printed Photoelectrodes, *Adv. Mater. Interfaces* **2023**, 2300557, **IF 5.4**.

Conferences

- **Sanna, M.**; Ng, S.; Vaghasiya, J. V.; Pumera, M., "Fluorinated MAX Phases for Photoelectrochemical Hydrogen Evolution", CEITEC PhD Retreat, 20 September 2022, Telč, best oral contribution;
- **Sanna, M.**; Ng, S.; Vaghasiya, J. V.; Pumera, M., "Fluorinated MAX Phases for Photoelectrochemical Hydrogen Evolution", X NyNA 2022: International Conference on Analytical Nanosciences and Nanotechnologies, 5-8 September 2022, Ciudad Real, poster and flash talk contribution;
- **Sanna, M.**; Ng, S.; Pumera, M., "Metal Phosphorous Trichalcogenides ($MPCh_3$) for photoelectrochemical energy conversion", CEITEC PhD Retreat, 21 September 2021, online, oral contribution;
- **Sanna, M.**; Pumera, M., "Breaking the wall of 3D printing for energy application", Finalist of the Falling Walls Lab Czech Republic competition, 14 September 2021, Prague, oral contribution;
- **Sanna, M.**; Ng, S.; Pumera, M., "Metal Phosphorous Trichalcogenides ($MPCh_3$) for photoelectrochemical energy conversion", 3rd Cross-Border Seminar on Electroanalytical Chemistry, 8-9 April 2021, online, oral contribution;
- **Sanna, M.**; Ng, S.; Pumera, M., "2D materials for photoelectrochemical energy conversion", Yonsei-BUT International Workshop: Nanomaterials for Chemical Engineering, 2nd February 2021, online, oral contribution.

Grants and financial support

- Specific Research Project 2022 of CEITEC BUT, "Hybrid MXene-based electrode for photoelectrochemical water splitting" (CEITEC VUT-J-22-8084), **200,000 CZK**, **Sanna M. (PI)**;
- Quality Internal Grant 2021 of the Brno University of Technology, "Modified 3D-printed electrodes with hybrid materials for the photoelectrochemical degradation of microplastics", **960,000 CZK** (2021-2023), OP RDE reg. no. CZ.02.2.69/0.0/0.0/19_073/0016948, **Sanna M. (PI)**;
- Winner of the Brno PhD Talent 2020 competition, "Organic functionalization of atomic layer deposited materials on 3D-printed electrodes for energy applications", **300,000** CZK (2020-2024), **Sanna M. (PI)**.

Abstract

The electrochemical production of hydrogen from water is gaining more attention as a clean and renewable energy source in response to the alarming environmental issues caused by the exploitation of fossil fuels during the last centuries. However, the process can be considered an environmentally friendly alternative only if it is fuelled using renewable sources of energy, like solar energy, the largest carbon-free resource available on our planet. Solar energy can be converted to electricity via solar panels and electrical energy be used for water splitting via electrocatalysts, such as platinum. Alternatively, the water splitting to hydrogen can be carried out directly via solar light energy. However, the yields of direct photochemical water splitting are low. The combination of both approaches, also called photoelectrochemical water splitting, combines the best of both worlds – electrocatalytic water splitting with the aid of photons. For these reason, the study of novel materials based on earth-abundant elements that can be applied as photoelectrocatalysts for hydrogen generation is fundamental to guiding society toward more sustainable energy production.

This thesis explores the potential of the emerging two-dimensional (2D) materials and related layered compounds, alongside investigations into the utility of 3D printing for fabricating functional electrodes in the field of photoelectrochemistry. The study of several transition metal selenophosphites confirmed their potential as photoelectrocatalysts for hydrogen generation, in particular under the influence of visible light. MAX phases were modified through exposure to fluorine gas and the properties of the obtained fluorinated MAX were investigated, starting from their morphology to their potential as photoelectrocatalysts for the hydrogen evolution reaction. The fluorinated phases showed better performances compared to the untreated MAX phases. The improved catalytic activity was attributed to photoactive oxyfluorides that formed as a consequence of the fluorination process. The photoactivity of the MAX phases was further

investigated both by theoretical and experimental approaches, to understand the origin of the photocatalytic behaviour. The results showed that the presence of oxide impurities on the phases plays a crucial role in the photoelectrochemical production of hydrogen. The role of the oxides in the photocatalytic activity of these compounds inspired the fabrication and investigation of 3D printed electrodes and their modification with atomic layer deposited oxides, like TiO_2, SiO_2, and Al_2O_3. Also in this case, the presence of a thin layer of oxide on the surface of the electrode contributed to significantly better performances under the influence of visible light. The obtained results demonstrated the importance of the fundamental study of novel 2D materials for application in the photoelectrochemical production of hydrogen and open new insights into the fabrication of innovative 3D printed conductive devices that can be modified with functional materials for energy conversion.

Keywords

Hydrogen generation, 2D materials, photoelectrochemistry, transition metal selenophosphites, MAX phases, 3D printing, atomic layer deposition

Abstrakt

Elektrochemická výroba vodíku z vody získává stále více pozornosti jako čistý a obnovitelný zdroj energie v reakci na alarmující environmentální problémy způsobené těžbou fosilních paliv během posledních století. Proces však lze považovat za ekologicky šetrnou alternativu pouze tehdy, pokud je poháněn obnovitelnými zdroji energie, jako je solární energie, největší uhlíkově neutrální zdroj dostupný na naší planetě. Solární energie lze přeměnit na elektřinu pomocí solárních panelů a elektrická energie může být využita k rozkladu vody za pomocí elektrokatalyzátorů, jako je platina. Alternativně lze rozklad vody na vodík provádět přímo pomocí solární energie. Nicméně výtěžky přímého fotochemického rozkladu vody jsou nízké. Kombinace obou přístupů, nazývaná fotoelektrochemický rozklad vody, kombinuje nejlepší z obou světů - elektrokatalytický rozklad vody s pomocí fotonů. Z tohoto důvodu je studium nových materiálů založených na hojně se vyskytujících prvků, které lze použít jako fotoelektrokatalyzátory pro tvorbu vodíku, zásadní pro navádění společnosti k udržitelnější výrobě energie. Tato práce zkoumá potenciál těchto nových dvourozměrných (2D) materiálů a souvisejících sloučenin, spolu s výzkumem využití 3D tisku pro výrobu funkčních elektrod v oblasti fotoelektrochemie. Studium několika přechodných kovových selenofosfitů potvrdilo jejich potenciál jako fotoelektrokatalyzátorů pro tvorbu vodíku, zejména za působení viditelného světla. MAX fáze byly modifikovány expozicí fluorovému plynu a vlastnosti získaných fluorovaných MAX byly zkoumány, začínaje jejich morfologií až po jejich potenciál jako fotoelektrokatalyzátorů pro reakci vývoje vodíku. Fluorované fáze vykazovaly lepší výkony ve srovnání s neošetřenými fázemi MAX. Zlepšená katalytická aktivita byla přičítána fotoaktivním oxyfluoridům, které vznikaly v důsledku procesu fluorace. Fotoaktivita fází MAX byla dále zkoumána jak teoreticky, tak experimentálně, aby bylo možné porozumět původu fotokatalytického chování. Výsledky ukázaly, že přítomnost oxidových nečistot na fázích hraje klíčovou roli v fotoelektrochemické tvorbě vodíku. Role oxidů v fotokatalytické aktivitě těchto

sloučenin inspirovala výrobu a zkoumání 3D tištěných elektrod a jejich modifikaci s oxidy deponovanými atomovou vrstvou (ALD), jako je TiO_2, SiO_2 a Al_2O_3. I v tomto případě přítomnost tenké vrstvy oxidu na povrchu elektrody významně přispěla ke zlepšení výkonu za působení viditelného světla. Získané výsledky prokázaly důležitost základního studia nových 2D materiálů pro aplikaci v fotoelektrochemické výrobě vodíku a otevřely nové pohledy na výrobu inovativních 3D tištěných vodivých zařízení, která lze modifikovat s funkčními materiály pro přeměnu energie.

Klíčová slova

Výroba vodíku, 2D materiály, fotoelektrochemie, selenofosfity přechodných kovů, MAX fáze, fluorace, 3D tisk, nanášení atomární vrstvy

Organization of the Thesis

This thesis is organized into ten chapters. **Chapter 1** briefly describes the objectives and main motivations of the thesis. Subsequently, the global energy crisis and challenges faced in sustainable energy generation will be described in **Chapter 2**, together with a brief introduction about layered transition metal selenophosphites ($MPCh_3$), MAX phases, and 3D printing technologies. A comprehensive description of the theoretical background and prior studies concerning these materials and their photo- and electrochemical applications are included in individual subchapters of **Chapter 3**. All the experimental methods employed for the development of this thesis work are briefly described in **Chapter 4**. **Chapters 5-7** include the published papers related to the study of 2D materials and related layered compounds, particularly $MPCh_3$ and MAX phases. Following, the published version of the papers connected to the development of 3D printed electrodes and their modification for the application as sensors and in energy-related fields are appended in **Chapters 8** and **9**.

This work will be concluded in **Chapter 10** with a summary of the results and a perspective on the potential future applications of the described materials and techniques.

1. Objectives of the Thesis

Given the severe environmental issues that our planet is facing and the limited amount and high cost of fossil fuels, it is predictable that our society will soon radically change in favor of more environmentally friendly energy sources. Photoelectrochemical (PEC) hydrogen production would, therefore, play a crucial role in exploiting solar energy, the largest renewable source available, for the production of carbon-free fuel. The past years have seen a surge in the discovery of promising new materials, in particular 2D layered materials, that can be applied in energy-related fields thanks to their outstanding electrochemical properties. However, only some of them have been extensively studied for the photoelectrochemical production of hydrogen, and the factors that can influence their performance are still not fully understood. This thesis aims to investigate emerging 2D materials and related layered compounds, including $MPCh_3$ and MAX phases, for application as electrodes in PEC hydrogen production and further understanding their photo- and electrochemical properties. In particular, the focus is to study cost-effective materials that are stable in the dark and under illumination, to efficiently use the solar energy absorbing principally in the visible spectral region. Furthermore, this thesis aims to evaluate how the modification of the abovementioned materials can lead to better PEC properties and, consequently, to better performances in facilitating hydrogen production. The investigation of the photoactivity of these materials contributes to a better understanding of their photocatalytic behavior, which is fundamental for the development of new promising photoelectrocatalysts.

The fabrication of 3D printing devices has emerged rapidly during the last decades for application in different fields, like aerospace, construction industry, etc. However, the utilization of this technique in energy-related fields is still really limited by the difficulty of producing conductive electrodes with the desired electrical and mechanical properties. The

fabrication of carbon-based nanocomposites, which combine the electrical properties of carbon additives with the benefits of the mechanical stability of thermoplastics, is a promising route towards rapid and low-cost manufacturing of customized-shaped electronic devices with minimized waste. Following this direction, the second objective of this thesis is the study of the electrochemical properties of conductive 3D-printed carbon devices, the optimization of their characteristics through the control of the printing process and post-printing treatments, and their surface modifications by atomic layer deposition (ALD) of photoactive oxides to enhance their performance in photoelectrochemical applications.

The aims of this thesis can be summarized in the following two points:

- The investigation of emerging 2D materials and layered compounds, their application as photoelectrocatalysts for hydrogen production under the influence of visible light, and the evaluation of the effect of common material modifications, like fluorination, and the presence of defects or impurities on their photoelectrochemical properties;

- The development of functional 3D-printed carbon electrodes and their modification through ALD of photoactive compounds for application in photo- and electrochemical processes.

2. Introduction to the challenges

The global energy demand is rapidly increasing due to the growing human population and rising living standards. The high rate of depletion, non-homogeneous distribution, slow formation, and the alarming environmental issues caused by the exploitation of fossil fuels during the last century pose a serious challenge to finding alternative sustainable energy sources. For this reason, the production of carbon-free fuels using affordable materials and renewable sources is at the forefront of research. Hydrogen is considered the perfect candidate for building a society based on clean energy production also because the combustion of this material leads to the generation of water, a harmless by-product for lands and air. However, most hydrogen is still produced from the reforming of methane, that is, from fossil sources. The generation of hydrogen from water is a promising solution. Still, it can be considered an environmentally friendly alternative only if the process is fuelled by exploiting renewable energy sources, such as solar, wind, hydrothermal, or hydroelectric energy. In particular, solar energy is the largest renewable carbon-free resource amongst the other renewable energy options. The water splitting to hydrogen can be carried out directly via solar light energy, however, the yields of direct photochemical water splitting are low. Alternatively, solar energy is converted to electricity via solar panels and the produced electrical energy is used for water splitting via electrocatalysts, such as Pt or transition metal dichalcogenides. The combination of both approaches, also called photoelectrochemical water splitting, combines the best of both worlds – electrocatalytic water splitting with the aid of photons. For this reason, the study of novel materials based on earth-abundant elements that can be applied as photoelectrocatalysts for hydrogen generation is fundamental to guiding society toward more sustainable energy production.

Since 2004, when a simple procedure to obtain single-layer graphene was proposed by Novoselov et al.[1], two-dimensional (2D) layered materials, such as graphene[2,3], graphitic carbon nitride (g-C_3N_4)[4,5], transition metal dichalcogenides[6], transition metal trichalcogenphosphites ($MPCh_3$)[7], monoelemental compounds (Xenes)[8–10], and transition metal carbides (MXenes), emerged as novels and promising electrocatalysts for energy conversion. The common feature of 2D materials is their peculiar structure: in their bulk form, they present stacked layers, one on top of the other. The in-plane bonds are strong; however, the interactions between the layers are weaker, allowing the exfoliation or delamination to a single or few layers[11–14]. Moreover, the chemical and optoelectronics properties of 2D layered materials can be enhanced through different modifications, such as doping or surface engineering[15]. In particular, chemical modification by fluorination is fascinating for PEC applications because it can tune the physical and optical properties related to the photoresponses of 2D materials. For example, the fluorination of graphene[16,17], phosphorene[18], and g-C_3N_4[19] resulted in improved surface polarity, thermal and chemical stability, and tunable or opening of the band gap.

Among the 2D materials, $MPCh_3$ are particularly gaining interest due to their catalytic properties in the HER[7,20–23]. For the chalcogen atom (Ch), only compounds with sulfur or selenium are known until now. Nevertheless, a vast number of metals are acknowledged to form this kind of material, such as transition (e.g., Mn, Fe, Cd, Zn, Ni, etc.) and post-transition metals (e.g., Sn, Ga, In), as well as alkali metals like Ca and Mg[7,24,25]. $MPCh_3$ were deeply studied for their magnetic properties[26–28], but recent studies mainly focus on their potential as photocatalysts for energy applications[25,29,30].

MXenes are another class of 2D materials that have attracted attention for electrochemical applications in recent years. They are characterized by high metallic conductivity, high negative zeta potential, and fast charge transfer kinetics[14,31–33]. MXenes are commonly synthesized from

their layered parent MAX phases (MAX), a class of layered ternary materials with the general formula $M_{n+1}AX_n$, where M is an early transition metal, A is an element from IIIA and IVA group, X is carbon or nitrogen, and n is equal to 1, 2, or 3[34–37]. By applying acid treatment with aqueous hydrofluoric acid and sonication, the A element interlayer can be selectively etched and washed out from the MAX giving a set of single or multilayer. The scientific community mainly concentrates on applying MXenes in different fields, although MAX and their properties have not been thoroughly investigated.

This thesis primarily focuses on the study and the application of emerging 2D materials and related layered compounds, such as $MPCh_3$ and MAX, for the photoelectrochemical production of hydrogen. Parallely, the study of 3D printing techniques for fabricating functional electrodes that can be applied in photoelectrochemistry was implemented. Indeed, additive manufacturing, commonly called 3D printing, presents a versatile method with remarkable potential for utilization in the 21st century. It offers a straightforward approach for swiftly prototyping customized 3D structures using various precursor materials, like ceramics, metals, and others[38–40]. Different studies recently proved the potential utilization of 3D printing techniques, such as fused deposition methods, in electrochemistry[41–44], but the use of 3D-printed carbon electrodes is still underexplored for PEC applications. In this thesis, 3D-printed carbon electrodes were studied and modified for application as photocatalysts for HER, giving a better understanding of their possible use as a conductive platform for functional material in energy production or other electrochemical applications.

3. Literature Review

3.1. Theory and background

3.1.1. Hydrogen as energy source

The idea of a society based on hydrogen as the primary energy carrier started in 1800 when Nicholson and Carlisle performed the electrolytic decomposition of water for the first time, obtaining hydrogen and oxygen. Even if hydrogen is the most abundant element in the universe, it is considered an energy carrier and not a primary energy source because it cannot be found in the earth in its elemental state (H_2). Still, energy is required to obtain it from water or other substances, like natural gas, coals, or other hydrocarbons. The main virtue of using hydrogen as a fuel is that it generates only water as a by-product, producing no CO_2 when burned in the air. In addition, as shown in Table 3.1, hydrogen has the highest energy content per unit mass than any fuel. However, one kilogram of hydrogen corresponds to 11200 liters, an important volume compared to other fuels[45]. Indeed, hydrogen is mainly used in spacecraft, where the storage space is sufficient, but it is an engineering challenge to its direct application in terrestrial vehicles.

Table 3.1. Comparison of the properties of principal fuels[45]. Energy density for gases is referred to 1 atm and 25°C, readapt from Ref. 43.

	Density kg/m^3	*Energy density* kWh/m^3	*Energy* kWh/kg
Methane	0.71	9.1	12.8
Gasoline	702	8680	12.4
Diesel	855	10090	11.8
Methanol	799	4030	5.0
Hydrogen	0.0838	3.0	33.3

Nowadays, most hydrogen is produced by steam-reforming methane or water gas shift reactions. However, neither of these approaches is environmentally friendly since they involve using fossil fuels and the consequent production of CO_2 as a by-product. A carbon-neutral approach for hydrogen production is the electrolysis of water employing energy produced by renewable sources, like wind or solar. Currently, electrolysis supplies 2% of the total amount of hydrogen since it is not economically competitive against steam methane reforming[46]. Nevertheless, the cost of natural gas is destined to increase due to environmental, social, political, and economic factors, and the electrolysis from water is predicted to become the preferred method for hydrogen production.

3.1.2. Water electrolysis

Water electrolysis is the process of splitting hydrogen and oxygen from water using electricity. This approach is exciting, considering 70% of the earth's surface is covered with water, particularly if seawater could be used without further treatment to obtain high-purity gases, like hydrogen and oxygen. The reaction is carried out in a water electrolyzer that consists of two electrodes, anode and cathode, immersed in an electrolyte to facilitate the movement of ions between them. The oxygen evolution reaction (OER, Equation 3.1.1) takes place at the anode, and the hydrogen evolution reaction (HER, Equation 3.1.2) at the cathode[47]:

Anode **OER** $H_2O + 2h^+ \rightarrow 2H^+ + \frac{1}{2}O_2$ 3.1.1

Cathode **HER** $2H^+ + 2e^- \rightarrow H_2$ 3.1.2

Water splitting into hydrogen and oxygen is not a spontaneous reaction and requires the application of a minimum potential of 1.23 V if no additional heat is provided to the system, as shown in Equation 3.1.3. Nevertheless, the necessary potential will be higher to compensate for the resistive losses and reach a reasonable hydrogen production rate[47].

$$E° = -\frac{\Delta G°}{nF} = -1.23\ V \quad 3.1.3$$

where $\Delta G° = 237$ kJ/mol, n is the number of electrons involved, and F is the Faraday constant.

The HER reaction mechanism in acidic media consists of two steps, adsorption and desorption. Moreover, the hydrogen desorption can proceed through two pathways, given by Equations 3.1.4, 3.1.5, and 3.1.6[48,49]:

Step 1: $H_3O^+ + e^- \rightarrow H_{ads} + H_2O; b \approx 118\ mV/dec$ (Volmer reaction) 3.1.4

Step 2: $H_{ads} + H_{ads} \rightarrow H_2; b \approx 29\ mV/dec$ (Tafel reaction) 3.1.5

Or $H_{ads} + H_3O^+ + e^- \rightarrow H_2 + H_2O; b \approx 39\ mV/dec$ (Heyrovsky reaction) 3.1.6

The prevalence of one mechanism to the other will depend on the system used to carry out the reaction, and it can be experimentally determined using the Tafel slope, *b*. In general, for values of Tafel slope above 118 mV/dec, the determining step is the discharge reaction or known as the Volmer reaction, and for lower values (≈39 mV/dec for Heyrovsky reaction and ≈29.5 mV/dec for Tafel reaction), the desorption processes are the rate-determining ones. These values can be obtained by plotting the logarithm of the measured current density against the overpotential and then applying a linear fitting to the obtained graphs. Tafel slope indicates the potential required to increase the current density by one order of magnitude[50]. This means that smaller overpotential and Tafel values indicate better electrocatalytic performance of a catalytic material since less energy is needed to drive the catalytic reactions.

3.1.3. Photoelectrochemical hydrogen generation

Solar energy is the largest renewable energy source available, and it can be used in different ways to produce energy. The amount of sunlight that reaches the earth per hour ($\approx 1.2 \times 10^5$ TW) is sufficient to fuel all human activities for one year[51]. However, solar energy is diluted during the day and over the earth's surface, causing problems in harvesting the sunlight as the primary carbon-free energy source. For this reason, implementing the technology used for harvesting this remarkable amount of energy to achieve long-term sustainable energy sources

is at the center of the attention of the scientific community. In particular, for a long time, scientists have focused on using solar production of clean hydrogen fuels with high energy density from water through PEC reactions[52–54]. Nevertheless, water is transparent to the wavelengths constituting the solar spectrum, hence, the PEC water splitting requires an agent (semiconductor, dye, or chromophore) capable of absorbing sunlight and generating electron-hole pairs that can be involved in the reaction. Indeed, in PEC water electrolysis, one or both the electrodes are made/modified with photoactive semiconductor materials[55], constituting the photocathode and/or photoanode. In particular, the study of the photocathode and the connected HER is the main focus of this thesis. The PEC process starts when the light of appropriate wavelengths hits the semiconductor surface, causing the generation of electrons and holes. In a simple photocatalytic process, these charges will tend to easily recombine in the bulk and on the surface of the material. However, the application of electric potential to the cell, helps to fastly separate the charges between the two electrodes, with the holes reacting with water to produce oxygen and protons at the anode, while the electrons flowing in the cathode to reduce the protons to hydrogen gas. The reduction of the recombination phenomena and the possibility to use the solar light, not only to fuel the cell, but also to boost the catalytic activity of the electrodes, makes the PEC water splitting the most promising approach for the hydrogen generation as energy carrier. Extensive efforts and significant progress have been made toward the fabrication of electrocatalysts with earth-abundant materials, including metals and their compounds (e.g., 2D transition metal oxides and dichalcogenides). Also, several metal oxide-based photocatalysts have been demonstrated to be effective for water splitting under UV light irradiation. For example, TiO_2 is the most reported material as a benchmark for the UV-light-driven water splitting reactions due to its good photo-stability, low toxicity, large abundance, and low cost. Unfortunately, TiO_2 has a large bandgap of 3.2 eV, which can only be used in the UV light range, which includes only 5% of all solar energy (solar conversion efficiency in UV

light is only 2% compared with 16% when visible light up to 600 nm can be utilized)[56]. Thus, developing and studying new photoelectrocatalysts with high photocatalytic activity under visible light irradiation is one of the most attractive research topics in PEC water splitting and one of this thesis's main focuses.

3.2. State of the art

3.2.1. 2D layered materials for electrochemical hydrogen production

Since 2004, when a simple procedure to obtain single-layer graphene was proposed by Novoselov et al. [1], 2D layered materials, such as graphene[2,3], graphitic carbon nitride (g-C_3N_4)[4,5], transition metal dichalcogenides (TMDs)[6], monoelemental compounds[8–10], and transition metal carbides (MXenes), emerged as novels and promising electrocatalysts for energy conversion. 2D materials refer to materials in which electrons can move freely only on the nanometer scale (1–100 nm) in two dimensions. Strong in-plane bonds and weak interlayer Van der Waals forces characterize them[11].

Several 2D materials have been studied, modified, and applied for the electrochemical hydrogen generation from water. As a central member of the carbon family, 2D graphene, a single layer of carbon atoms with a hexagonal-packed lattice, has attracted considerable and persistent attention[57]. However, pristine graphene with high graphitization is electrochemically inert and exhibits a relatively low HER activity, numerous chemical modification strategies can be employed to tailor the electronic structure and chemical reactivity of a graphene sheet, effectively making its inert surface catalytically active[58].

In 2007, the Thomas group reported remarkable HER performance of MoS_2 with a hydrogen adsorption Gibbs free energy of only 0.08 eV, which is even lower than that of Pt with a value of 0.09 eV[6,59]. This highlights that 2D TMDs could be one of the most promising candidates for

HER. Since then, numerous studies have focused on improving the HER performance of 2D TMDs. On the one hand, the target is to increase the number of active sites. Generally, the sites along the edges are active, while the sites within the basal plane are inactive[6,60,61]. Besides the edge sites, the Cao group revealed that sulfur vacancies and grain boundaries are active as well[62]. On the other hand, the target is to improve the conductivity of 2D TMDs since most compounds are semiconductors, and many researchers have prepared metallic phases, such as metastable 1T MoS_2, enhancing the performance of HER[63–65].

3.2.1.1. Transition metal trichalchogenphosphites ($MPCh_3$)

$MPCh_3$ is a large family of van der Waals-layered materials whose structure is derived from the CdI_2 and $CdCl_2$ structural type and assumes a monoclinic or rhombohedral lattice configuration. They are dominated by divalent metal cations stabilized in octahedral chalcogen environments. $MPCh_3$ were synthesized for the first time in 1894[66] and then intensively studied for their magnetic properties[26–28]. However, with the recent rediscovery of 2D layered materials, more studies are focused on their study for energy-related applications (Figure 3.1). It is reported that these materials are semiconductors with band gaps between 1.3 and 3.5 eV, depending on the chalcogen elements and the metal[25,29,30]. Different works[20,21] reported the tendency for $MPSe_3$ crystals to generally show lower onset potential for HER than the analog MPS_3. This fact was attributed to a more significant distortion of the M-Se bond in the crystal structure, resulting in easier absorption of H and, consequently, better catalytic activity. Similarly to other 2D materials, the exfoliation of $MPCh_3$ results in enhanced catalytical activity due to the exposure of a higher number of active sites. For example, Mukherjee et al. [23,67] reported an improved onset potential of about 300 mV for $FePS_3$ and $FPSe_3$ after exfoliation to a few layers, as compared to their bulk crystals. Furthermore, it is reported that metal doping can dramatically

improve the electrochemical properties of $MPCh_3$. Li et al. reported that traces of cobalt doping on $NiPS_3$ led to enhanced catalytic activity for HER, attributed to increased electrical conductivity by about three orders of magnitude[68].

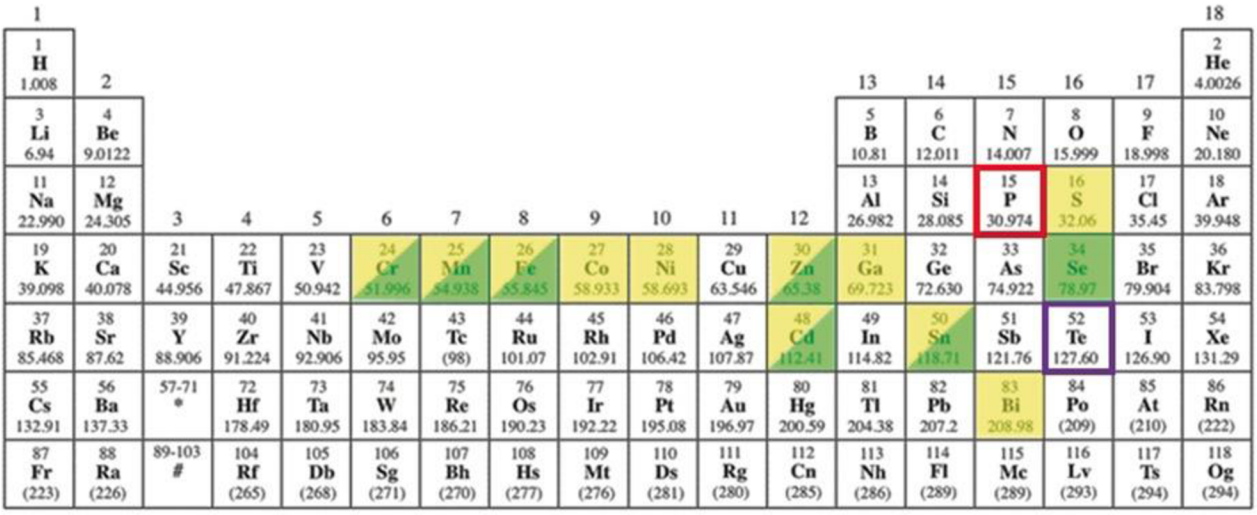

Figure 3.1. The highlighted blocks in the periodic table represent metal elements for which the layered $MPCh_3$ structure has been reported in electrochemical applications (S in yellow and Se in green)[7]. Phosphorus is delimited in red as it is a constant in $MPCh_3$. There are no reports of $MPCh_3$ with tellurium as the chalcogen element, delimited in purple. Copyright (2019) Wiley. Reproduced with permission from Ref 7.

3.2.1.2. MAX phases

In 2000, Barsoum[69] used the term "MAX phase" for the first time indicating a class of ternary layered carbides and nitrides that present hexagonal structures with space group P63/mmc. In their structure, layers of M_6X octahedra are connected by shared edges and alternated with layers of the A element. Changing the n value in the general formula $M_{n+1}AX_n$, the structure of the MAX changes slightly, with a different number of layers every two A layers, as shown in Figure 3.2. These phases show a remarkable combination of metallic and ceramic properties,

like good electrical and thermal conductivity and high thermal shock and oxidation resistance. Most of the known MAX were discovered by Nowotny et al.[70,71] more than 40 years ago. Still, only after the reports of Barsoum et al. in 1996[72,73] about their intriguing physical properties, the interest in MAX exploded. Most of the works related to MAX were primarily focused on studying their fundamental physical properties but less on their potential applications[74,75]. However, in the laat years, MAX have been investigated for application in energy-related fields, also thanks to several reports about the promising electrochemical properties of layered materials. For example, Rosli et al.[35] reported the synthesis and characterization of Ti_2AlC, Ti_2AlN, Ti_3AlC_2, and Ti_3SiC_2. The authors investigated the electrochemical properties and the potential application of these phases as electrocatalysts for HER and oxygen reduction reaction (ORR). The results showed that MAX have intermediate electrocatalytic performances compared to other recently reported layered catalysts. Following this work, Kumar et al.[76] reported the study of the electrochemical properties of Ti_2AlC, Ta_2AlC, Ti_2SnC, Ti_3SiC_2, V_2AlC, Mo_2TiAlC_2, and Cr_2AlC and the evaluation of their performances for HER. The authors concluded that Mo_2TiAlC_2 was the phase with the higher catalytic activity for hydrogen generation, thanks to the dominant effect of the Mo layer, also described for the analog MXene ($Mo_2TiC_2T_x$) by Anasori et al.[77]. In another recent report, Novcic et al.[78] studied in detail the electrochemical performance of Mo_2TiAlC_2 for HER, using scanning electrochemical microscopy. The obtained results showed that the HER activity was not uniform among the surface of the material but localized in highly active spots.

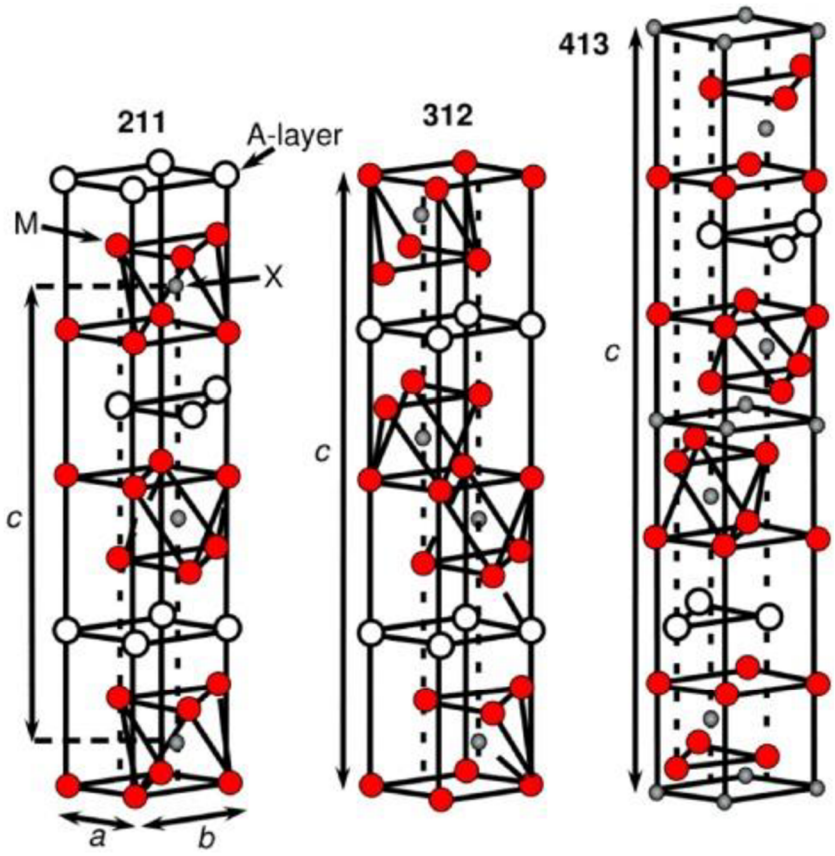

Figure 3.2. MAX unit cell structures of 211 (n = 1), 312 (n = 2), and 413 (n = 3)[79]. The figure is reproduced with permission from Ref. 79, Copyright Elsevier (2016).

3.2.2. Photoelectrochemical hydrogen production

Highly efficient electrocatalysts and photocatalysts for the HER can be used together as catalysts for photoelectrocatalysis. For example, spin-coated reduced graphene oxide (RGO) on $CuBi_2O_4$ electrode improved the photoelectrochemical performances thanks to the electron collection properties of RGO from the photocathodes[80]. The photocurrent density of $CuBi_2O_4$/RGO was nearly two times higher than that of $CuBi_2O_4$. In another work, Sim et al. used N-doped graphene quantum sheets (N-GQSs) as the co-catalyst to modify the silicon photocathode for the HER[81]. The saturated photocurrent density of the N-GQSs/planar Si was higher than that of planar Si without N-GQSs. Meanwhile, the N-GQSs/planar Si showed an

increased applied bias photon-to-current efficiency (ABPE) of 2.29%, which is greater than that of the bare Si system (0.91%).

TMDs with high HER activity are widely used as co-catalysts to improve the PEC performances of photocathodes. For example, MoS_2 fabricated by atomic layer deposition was used as the co-catalyst to decorate the Si photocathode[82]. The transportation and separation of photo-generated carriers were boosted because of the heterojunction between MoS_2 and Si. In addition, the activity of MoS_2 was further increased with the post-sulfurization at high temperatures. Under one sun illumination, the MoS_2/Si photocathode exhibited a reduced overpotential of about 630 mV compared to bare Si. Dong et al. used MoS_2 as the co-catalyst to modify the CdSe/NiO heteroarchitecture photoelectrode[83]. In this system, the CdSe absorbed light and generated electron–hole pairs. MoS_2 quickly attracted the electrons and took part in the HER reaction, reducing the carrier recombination.

3.2.3. Additive manufacturing

Additive manufacturing, commonly referred to as 3D printing, has transformed manufacturing processes by enabling the production of 3D objects through the controlled deposition of successive layers of material based on digital designs. In contrast to subtractive manufacturing methods, which involve removing material, 3D printing offers distinct advantages such as rapid prototyping and minimal material waste[38]. The selection between additive and subtractive techniques hinges on factors such as object complexity, material type, replication requirements, and cost considerations. Additive manufacturing excels in creating intricate designs with hollow components, mainly using plastic-based materials, whereas subtractive methods are preferable for metal or wood-based objects. Additionally, additive manufacturing can reduce energy consumption and material waste compared to subtractive processes[39,40]. The workflow typically commences with creating a virtual model, which is then converted into a printable

format and sliced into 2D layers. Several 3D printing technologies exist, including photopolymerization, extrusion, powder-based, and lamination methods. Extrusion-based approaches, like fused deposition modeling (FDM, Figure 3.3), are popular due to their simplicity and versatility in utilizing thermoplastic materials such as polylactic acid (PLA) and acrylonitrile butadiene styrene (ABS)[84]. In recent years, the integration of 3D printing in electrochemistry has gained momentum, allowing for the production of customized conductive electrodes and liquid handling systems for applications such as sensing, energy storage, and electrochemical synthesis[41,43,44]. Advances in direct 3D printing of carbon-based conductive materials and the creation of complex electrode architectures for lithium-ion batteries underscore the potential of additive manufacturing in advancing electrochemical technologies. With the increasing accessibility and versatility of 3D printing, its incorporation into electrochemistry research and development promises further advancements in device fabrication, performance enhancement, and cost reduction.

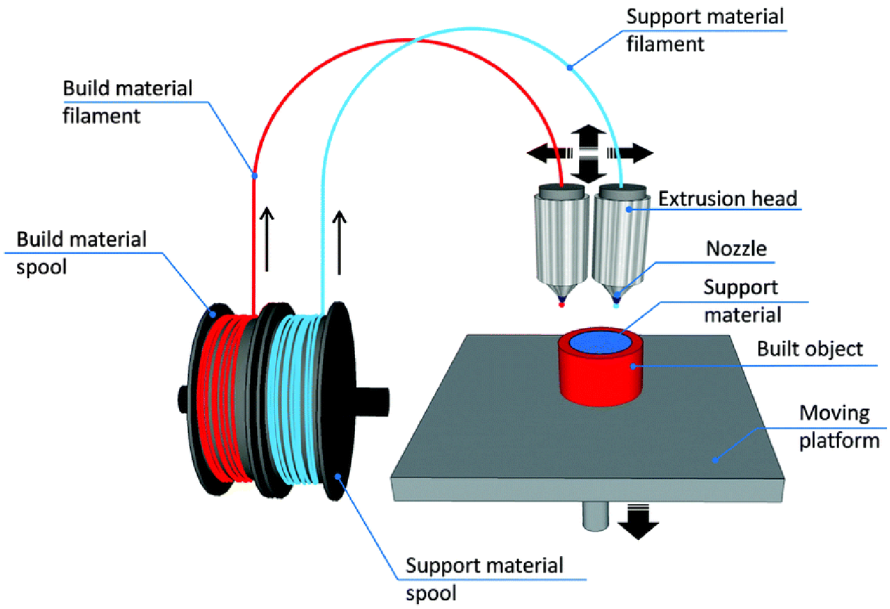

Figure 3.3. Schematic diagram of fused deposition modeling (FDM). A nozzle fed with a thermoplastic wire is moved in three dimensions across the building platform, onto which

molten voxels of a polymer are applied[84]. Reproduced from Ref. 84 with permission from the Royal Society of Chemistry.

4. Methods

This chapter contains the list of the purchased materials and suppliers, a brief description of the characterization techniques and the instruments employed to perform them, and the general methodology used to evaluate the performances of the studied samples.

The samples were prepared using different kinds of materials. All the $MPCh_3$ crystals ($MnPSe_3$, $FePSe_3$, and $ZnPSe_3$) were selenophosphites, so it will be referred to them as $MPSe_3$. Among the purchased MAX (Nb_2AlC, Ta_2AlC, Cr_2AlC, Ti_2AlC, and Ti_3AlC_2), four of them, namely Ta_2AlC, Cr_2AlC, Ti_2AlC, and Ti_3AlC_2, were treated to obtain the corresponding fluorinated MAX (F-MAX). All the other materials were used as received.

4.1. Materials and synthesis

$MPSe_3$ crystals were purchased from XFNANO, China. MAX were purchased from Laizhou Kai Kai Ceramic Material Co. Ltd. Screen-printed carbon electrodes (SPCE, SE 101) were obtained from CH Instruments, Inc. and Indium-Tin-Oxide (ITO) coated polyethylene terephthalate (PET) from Sigma Aldrich. Conductive carbon cement EM-Tec C38 was obtained from Micro to Nano. Potassium hexacyanoferrate (III) (99%), potassium nitrate (analytical grade), and potassium chloride (analytical grade) were purchased from Merck. Sulfuric acid 96% was obtained from Penta, Czech Republic. Dimethylformamide (DMF) was purchased from Sigma-Aldrich. Trimethylaluminum (TMA) and tetrakis(dimethylamido)silane (TDMASi) were obtained from Sigma-Aldrich, while tetrakis(dimethylamino)titanium(IV) (TDMATi) from Strem Chemicals. All solutions were prepared in deionized water with a resistivity of 18 MΩ cm.

The carbon black (CB)/polylactic acid (PLA) and the carbon nanotubes (CNT)/PLA (brand name 'Black Magic') filaments were commercially available and purchased from Proto-Pasta, USA, and Graphene Laboratories Inc., USA, respectively.

4.1.1. Fluorination of MAX phases

A four-chamber PTFE reactor was located inside a sealed Monel autoclave and MAX, namely Ta_2AlC, Cr_2AlC, Ti_2AlC, and Ti_3AlC_2, were placed separately in the four chambers. The reactor was secured using a permeable stopper, evacuated and flushed with nitrogen gas (N_2) several times. The autoclave was then evacuated for 20 minutes to achieve complete deaeration. After flushing 20% fluorine gas (F_2) in N_2 inside the autoclave and pressurizing to 5 bar, the system was heated to 150 °C by a Wood's metal heating bath and maintained overnight. Afterward, the system was cooled down to room temperature, and the gases were removed from the autoclave and treated with soda for neutralization. The autoclave was vented and flushed with N_2 several times to remove any traces of F_2 and related volatile compounds and finally evacuated through a column of sodium carbonate. After filling with N_2 to atmospheric pressure, the F-MAX (F-Ta_2AlC, F-Cr_2AlC, F-Ti_2AlC, and F-Ti_3AlC_2) were collected from the reactor and stored in sealed vials.

4.1.2. Preparation of 3D-printed carbon electrode

Multimaterial 3D-printed carbon electrodes were printed by a multimaterial 3D printer (Prusa i3 MK3+MMU2) and consisted of four alternating horizontal layers of CNT/CB materials. The circular head of the electrodes had a radius of 3 mm (6mm diameter), and the electrode rod had a width of 3.5 and a length of 15 mm. For all the electrodes in this thesis, a 0.6 mm nozzle heated to 220°C was employed to melt the filaments. The infill pattern was set to 15%, the layer thickness was 0.15 mm, and the bed printing temperature was fixed to 60°C to ensure the best

adhesion of the printedstructures. The as-printed 3D carbon electrodes underwent different activation steps, described in detail in each paper and summarised below.

(i) Electrochemical oxidation + immersion in a reducing agent;

(ii) Immersion in polar aprotic solvent;

(iii) Immersion in polar aprotic solvent + electrochemical oxidation

(iv) Saponification

All electrodes were rinsed thoroughly with water and dried in air.

4.1.3. Atomic layer deposition of TiO_2, SiO_2, and Al_2O_3

Atomic layer deposition (ALD) is a gas-phase thin film chemical deposition method in which the source vapors are pulsed into the reactor alternately, separated by purging or evacuation periods. In each step, the surface is saturated with a monomolecular layer of the precursor introduced[85]. The advantage of ALD with respect to other deposition processes is that the film growth proceeds in a self-limiting manner. In this way, each cycle deposits precisely the same amount of material. Accordingly, the film thickness may be accurately controlled simply by the number of deposition cycles. The self-limiting growth mechanism also ensures that the precursor fluxes do not need to be uniform over the substrate[85,86].

A typical ALD process is illustrated in Figure 4.1, which shows the example of metal oxide ALD using a metal precursor of ML_2 (M = metal and L = ligand) and water (i.e., H_2O) as the precursors. In the first step, the ML_2 vapor is introduced into an ALD reactor containing the substrate(s) to be coated. ML_2 consists of two L functional groups bound to a central metal atom and can react with one or two surface hydroxyl (-OH) groups. Hydroxyl groups naturally exist on most substrates, such as silicon, metal, and metal oxides. The ML_2 reaction forms a new metal-oxygen bond and liberates one or more L groups as the HL gas, while the other L group

remains bound to the metal. Once ML_2 has consumed all of the surface hydroxyl groups, the reaction terminates even in the presence of excess ML_2. The excess ML_2 precursor and HL product are removed by evacuation or inert gas purge. Next, water vapor is supplied. The water reacts with the surface L groups deposited by the previous ML_2 exposure, forming again new metal-oxygen bonds and releasing HL as the by-product. This reaction also repopulates the surface with -OH groups, restoring the initial surface chemical termination. Finally, the residual water and HL are removed by evacuation or purging. These four steps (dosing ML_2, the first purge, dosing water, and the second purge) comprise one metal oxide ALD cycle and generally deposit a layer of < 0.2 nm of metal oxides. Since the surface is restored to its initial state, any number of metal oxide ALD cycles can be performed sequentially to grow a film of the desired thickness.

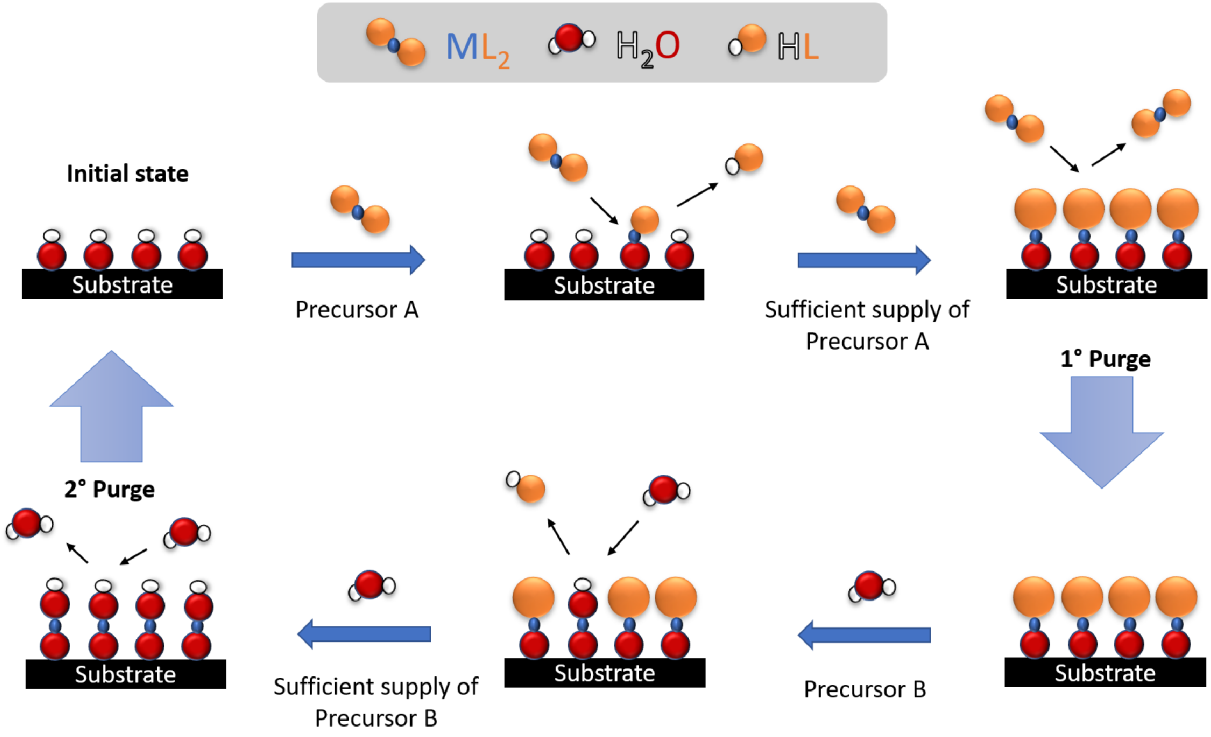

Figure 4.1. Schematic illustration of the ALD process of metal oxides for using ML_2 (precursor A) and water (precursor B).

In this thesis, an atomic layer deposition (ALD, Ultratech/CambridgeNanoTech Fiji 200) system was used for material deposition on the surface of the 3D-printed carbon electrodes after the activation process. TDMATi, TMA, and TDMASi were used as Ti, Al, and Si precursors, respectively. TDMATi was heated to 75 °C to increase the vapor pressure, whereas TMA and TDMASi were not heated. For TiO_2 and Al_2O_3, deionized water was used as an O_2 precursor, and argon was the carrier gas. The plasma for ALD SiO_2 was obtained by ionizing O_2 gas. For all substrates, the temperature was 150 °C.

4.2. Materials characterization

4.2.1 Morphology and composition

Scanning Electron Microscopy (SEM). SEM is an imaging technique used to investigate the morphology of solid specimens. The SEM uses a focused beam of high-energy electrons to generate accelerated secondary electrons with significant kinetic energy. The detection of the secondary electrons is commonly used for imaging since they are the most valuable for showing the morphology and topography of the sample. In this thesis, high-resolution SEM (FEI Verios 460L, Mira 3 XMU Tescan, and Lyra 3 Tescan) were used to evaluate the morphology of $MPSe_3$, MAX, F-MAX, and 3D-printed carbon electrodes.

Energy Dispersive X-ray Spectroscopy (EDS). EDS is a technique associated with SEM that is used to investigate the chemical composition of the analyzed sample. As a result of the exposure to the electron beam of SEM, atoms on the surface of the specimen are excited and emit specific wavelengths of X-rays that are characteristic of the atomic structure of the elements. An EDS detector can analyze these X-ray emissions and assign them to the appropriate element, yielding the composition of the atoms on the specimen surface. The EDS

detectors X-MAX20 (Oxford Instruments), XFlash 5010 (Bruker), and X-MaxN 150 (Oxford Instruments) were employed to obtain the elemental mapping and the quantification of the detected elements in terms of atomic percentage (At %). Based on the analyzed material, the applied accelerating voltage was changed in a range of 20-30 kV.

X-Ray Photoelectron Spectroscopy (XPS). XPS is a widely used surface-sensitive technique that provides information about the elemental composition and the chemical state of the elements in the sample. The analysis is based on the photoelectric effect, which describes how electrons absorb photons of a particular energy and emerge from the solid. The kinetic energy of the emitted electrons brings all the information about the sample since each element will require a specific amount of energy (binding energy) to leave the surface of the solid. All the materials used in this thesis work ($MPSe_3$, MAX, F-MAX, and 3D-printed carbon electrodes) were studied using XPS (Kratos Analytical Axis Supra) using a monochromatic Al Kα (1486.7 eV) X-ray excitation source with 225 W power. Survey spectra were obtained using emission 5 mA and a resolution of 80 eV, while the high-resolution spectra were measured using 15 mA and 20 eV. The obtained spectra were analyzed with CasaXPS software and calibrated against the C 1s peak (285 eV). The high-resolution spectra of the elements were fitted using Shirley-type background.

X-ray Diffraction Spectroscopy (XRD). XRD is an analytical technique used to identify the phase of crystalline material. This technique is based on constructive interference of monochromatic X-rays and a crystalline sample. These X-rays are directed at the sample through various angles, and the diffracted rays are collected. The conversion of the diffraction peaks to d-spacings allows the identification of the mineral because each mineral has a set of unique d-spacings. The structural analysis of MAX, F-MAX, and 3D-printed carbon electrodes was investigated using X-ray diffractometers (PANalytical XPert-PRO, Rigaku Smartlab 3 kW)

with a Co $K\alpha_1$ and a Cu $K\alpha_1$ source of wavelength 0.1789 nm. The JCPDS database was used to obtain the reference peaks for the detected phases.

4.2.2 Optical characterization

UV-Visible Spectroscopy (UV-Vis). UV-Vis is a technique based on the interaction of ultraviolet and visible light (300-900 nm) with matter. In some molecules and atoms, UV and visible light incident photons have enough energy to cause transitions between the different electronic energy levels. These transitions result in absorbance bands at wavelengths that are highly characteristic of the difference in energy levels of the absorbing species. This analysis was performed using a UV-Vis spectrophotometer (JASCO V-750) to obtain the MAX and F-MAX absorption spectra. The powders were suspended in a 50% solution of ethanol in water (0.625 mg/mL), and the absorbance spectra were acquired between 300 and 900 nm with a scan speed of 400 nm/min.

The reflectance spectra of MAX were measured by mounting an integrating sphere in the UV-Vis spectrophotometer. The integrating sphere is a hollow enclosure with walls constructed of a diffusely reflecting material that reflects all wavelengths of interest with high reflecting power. The diffuse reflectance of MAX powders was measured within 300-900 nm, using a scan speed of 400 nm min^{-1}. Kubelka-Munk function ($F(R_\infty)$)[87] was employed to estimate the band gap of MAX phases. In particular, the reflectance measurements can be transformed in the corresponding absorption spectra, according to Equation 4.2.1:

$$F(R_\infty) = \frac{K}{S} = \frac{1 - R_\infty}{2R_\infty} \qquad where \;\; R_\infty = \frac{R_{sample}}{R_{standard}} \qquad 4.2.1$$

$F(R_\infty)$ can substitute the absorption coefficient α defined in the Tauc method[88] by Equation 4.2.2:

$$(\alpha h\upsilon)^{\frac{1}{n}} = B\left(h\upsilon - E_g\right) \qquad 4.2.2$$

where h = Plank constant, υ = frequency, E_g = band gap energy, B = constant. The factor n is equal to ½ assuming direct transition band gap and equal to 2 for indirect transition band gap. Equation 4.2.2 can then be written in the form of Equation 4.2.3 and 4.2.4, respectively:

$$(F(R_\infty) * h\upsilon)^2 = B\left(h\upsilon - E_g\right) \qquad \text{for direct transition band gap} \qquad 4.2.3$$

$$(F(R_\infty) * h\upsilon)^{\frac{1}{2}} = B\left(h\upsilon - E_g\right) \qquad \text{for indirect transition band gap} \qquad 4.2.4$$

Tauc plots were obtained by plotting the $(F(R_\infty)\ h\upsilon)^2$ or $(F(R_\infty)\ h\upsilon)^{1/2}$ versus photon energy, and the baseline approach[89] was used for the graphic extrapolation of the values. In this approach, the linear fit is applied to the fundamental peak, similarly to the Tauc method, and to the slope below the fundamental peak, which can be identified as the "baseline". The band gap energy is estimated by the intersection of the two fitting lines.

4.3. Electrochemical measurements

All electrochemical measurements were carried out using a potentiostat (PGSTAT204, Metrohm Autolab, The Netherlands) controlled by NOVA software (version 2.1) in a three-electrode configuration. A platinum wire and a graphite rod were used as counter electrodes, and Ag/AgCl (1 M KCl) as the reference electrode. The working electrode (WE) was varied accordingly. All reported potentials were converted to the RHE using the potential value reported in the literature for the reference Ag/AgCl (1 M KCl, $E^0_{Ag/AgCl}$ = 236 mV[90]) and according to Equation 4.3.1:

$$E_{RHE} = E_{Ag/AgCl} + 0.059 * pH + E^0_{Ag/AgCl} \quad 4.3.1$$

Cyclic voltammetry measurements were performed in 10 mM $Fe(CN)_6^{3-}$ and 0.1 M KCl electrolyte with a scan rate of 100 mV/s.

4.3.1. Electrode preparation

The WE were prepared based on the nature of the material. The $MPSe_3$ crystals were attached to the SPCE ($MPSe_3$@SPCE) and the ITO coated PET ($MPSe_3$@ITO) using conductive carbon cement and conductive carbon tape, respectively.MAX and F-MAX were suspended in water (2.5 mg/mL) and sonicated for 60 minutes. The suspensions (5 uL) were then drop-casted on GC and SPCE and dried using a heat lamp.

4.3.2. Photoelectrochemical measurements

Linear sweep voltammetry (LSV) was performed by immersing the electrodes in a quartz cell containing 0.5 M H_2SO_4 solution for HER and 1 M NaOH for OER, with a scan rate of 2 mV/s. The illumination source for all the photoelectrochemical experiments was a customized LED (LZ4-44UV00, LZ4-40B208, and LZ4-40R208, LedEngin Inc.) setup with interchangeable wavelengths (365 nm, 460 nm, and 660 nm). Chronoamperometry measurements were performed by switching on/off during the experiment at regular intervals. The experimental conditions were changed based on the investigated material, as reported in Table 4.1:

Table 4.1. Summary of the experimental conditions for the chronoamperometry measurements.

WE	Electrolyte	Potential applied
$MPSe_3$@ITO	10 mM $Fe(CN)_6^{3-}$, 0.1 M KCl	0.76 V vs. RHE
$MPSe_3$@SPCE	0.5 M H_2SO_4	−0.50 V vs. RHE
MAX and F-MAX on GC	0.5 M H_2SO_4	-0.46 V vs. RHE
ALD TiO_2 on 3D-printed carbon electrode	0.5 M H_2SO_4	-0.40 V vs. RHE
ALD TiO_2 on 3D-printed carbon electrode	1 M NaOH	1.8 V vs. RHE

Part 1: Novel 2D materials for photoelectrochemical hydrogen evolution reaction

5. Layered transition metal selenophosphites for visible light photoelectrochemical production of hydrogen

Published paper included in this chapter:

Sanna, M.; Ng, S.; Pumera, M., Layered Transition Metal Selenophosphites for Visible Light Photoelectrochemical Production of Hydrogen. *Electrochem. Commun.* **2021**, 129 (May), 107077

The following results were presented at the conference: **3rd Cross-Border Seminar on Electroanalytical Chemistry (CBSEC), Yonsei-BUT International Workshop: Nanomaterials for Chemical Engineering, and at the CEITEC PhD Retreat 2021.**

5.1. Motivation for the study

The primary objective of this study was to conduct an experimental investigation into the photoelectrochemical characteristics exhibited by transition metal selenophosphites, specifically focusing on $MnPSe_3$, $FePSe_3$, and $ZnPSe_3$. Prior theoretical analyses indicated the potential of these materials as effective photoelectrocatalysts for solar-driven water splitting. However, the absence of empirical validation hindered the translation of theoretical predictions into practical applications. Motivated by the imperative to explore novel materials for sustainable energy production, particularly in hydrogen generation, our research aimed to bridge this gap by subjecting the abovementioned crystals to rigorous experimentation. Specifically, we assessed their performance in facilitating the hydrogen evolution reaction under acidic conditions while exposed to visible light irradiation. Through this empirical

investigation, this work aimed to provide valuable insights into the viability of transition metal selenophosphites as promising candidates for advanced solar-driven hydrogen production technologies.

5.2. Paper conclusion

The research dug into the properties of transition-metal selenophosphites crystals, specifically $MnPSe_3$, $FePSe_3$, and $ZnPSe_3$, assessing their efficacy as photoelectrocatalysts in driving the hydrogen evolution reaction. Remarkably, all crystals displayed exceptional photoelectrocatalytic activity when subjected to visible light (660 nm). Among them, $ZnPSe_3$ stood out by showcasing the lowest overpotential for the hydrogen evolution reaction and demonstrated superior responsiveness to light during photocurrent experiments conducted in acidic conditions. Therefore, within the scope of our investigation, $ZnPSe_3$ emerges as the most promising candidate for catalyzing hydrogen production through photocatalysis.

5.3. Author contribution

In this work, I prepared the electrode by attaching the $MPCh_3$ crystals on screen-printed electrodes and ITO. I performed the material characterization, studying the morphology using SEM and the elemental composition through EDS and XPS. Afterward, I carried out all the photoelectrochemical experiments, analyzed and plotted the data. Finally, I wrote the first draft of the manuscript and edited it accordingly with the other authors.

Electrochemistry Communications 129 (2021) 107077

Contents lists available at ScienceDirect

Electrochemistry Communications

journal homepage: www.elsevier.com/locate/elecom

Layered transition metal selenophosphites for visible light photoelectrochemical production of hydrogen

Michela Sanna [a], Siowwoon Ng [a], Martin Pumera [a,b,c,d,*]

[a] Future Energy and Innovation Laboratory, Central European Institute of Technology, Brno University of Technology, Purkyňova 123, 61200 Brno, Czech Republic
[b] 3D Printing & Innovation Hub, Department of Food Technology, Mendel University in Brno, Zemedelska 1, 61300 Brno, Czech Republic
[c] Department of Chemical and Biomolecular Engineering, Yonsei University, 50 Yonsei-ro, Seodaemun-gu, Seoul 03722, Republic of Korea
[d] Department of Medical Research, China Medical University Hospital, China Medical University, No. 91 Hsueh-Shih Road, Taichung 40402, Taiwan

ARTICLE INFO

Keywords:
2D materials
Transition metal selenophosphites
Photoelectrocatalyst
Hydrogen evolution reaction
Photoelectrochemistry

ABSTRACT

The growing consumption of global energy has posed serious challenges to environmental protection and energy supplies. A promising solution is via introducing clean and sustainable energy sources, including photoelectrochemical hydrogen fuel production. 2D materials, such as transition metal trichalcogenphosphites ($MPCh_3$), are gaining more and more interest for their potential as photocatalysts. Crystals of transition metal selenophosphites, namely $MnPSe_3$, $FePSe_3$ and $ZnPSe_3$, were tested as photocatalysts for the hydrogen evolution reaction (HER). $ZnPSe_3$ is the one that exhibited the lowest overpotential and the higher response to the light during photocurrent experiments in acidic media. For this reason, among the crystals in this work, it is the most promising for the photocatalyzed production of hydrogen.

1. Introduction

The generation of carbon free fuels, such as hydrogen from water, is at the forefront of research to reduce the emission of harmful compounds in the atmosphere. The water splitting to hydrogen can be carried out directly via solar light energy [1], however, the yields of direct photochemical water splitting are low [2–4]. Alternatively, the solar energy is converted to electricity via solar panels and electrical energy to be used for water splitting via electrocatalysts, such as Pt or transition metal dichalcogenides [5–8]. The combination of both approaches, photoelectrochemical water splitting, combines the best from both worlds – electrocatalytical water splitting with the aid of photons [9–11].

Since 2004, when a simple procedure to obtain single-layer graphene was proposed by Novoselov et al. [12], a renewed interest in two-dimensional (2D) materials has grown rapidly. The scientific community started to focus on the study of the remarkable properties and the possible applications of these materials, starting with mono-element compounds, like graphene, and then moving to more complex ones, for example transition metal dichalcogenides [6,7,13]. The common feature in 2D materials is their peculiar structure: in their bulk form they present stacked layers, one on top of each other. The in-plane bonds are strong, however, the interactions between the layers are weaker, and this allows obtaining single or few layers by exfoliation or delamination [14–17].

Among the rediscovered 2D materials, transition-metal trichalcogenphosphites ($MPCh_3$) are gaining more and more interest in particular due to their catalytic properties in the hydrogen evolution reaction (HER) [18–22]. Their structure is derived from CdI_2 and $CdCl_2$ structural type and assumes a monoclinic or rhombohedral lattice configuration. For the chalcogen atom (Ch), only compounds with sulfur or selenium are known until now. Nevertheless, a vast number of metals are acknowledged to form this kind of materials, such as transition (e.g., Mn, Fe, Cd, Zn, Ni, etc.) and post-transition metals (e.g., Sn, Ga, In), as well as alkali metals like Ca and Mg [23–25]. In the past, $MPCh_3$ were deeply studied for their magnetic properties [26–28], but recent studies are mainly focused on their potential as photocatalysts for energy applications. In fact, these materials are semiconductors with band gaps between 1.3 and 3.5 eV, depending on the chalcogen elements and the metal [23,25,29].

Hydrogen production by photocatalytic water splitting represents an alternative way to the exploitation of fossil fuels, since it provides a clean source of energy that helps to solve the serious environmental problems faced by our society [30–34]. However, several factors limit

* Corresponding author at: Future Energy and Innovation Laboratory, Central European Institute of Technology, Brno University of Technology, Purkyňova 123, 61200 Brno, Czech Republic.
E-mail address: pumera.research@gmail.com (M. Pumera).

https://doi.org/10.1016/j.elecom.2021.107077
Received 15 May 2021; Received in revised form 11 June 2021; Accepted 14 June 2021
Available online 17 June 2021

the application of this technology, such as low quantum yield and low activity in the visible spectral region. 2D materials such as $MPCh_3$ have the ideal band gaps for the application as photocatalysts for hydrogen generation since they could provide more efficient use of visible light in the photocatalytic process.

In this work, we tested the photoelectrochemical performance of three different crystals metal selenophosphites ($MPSe_3$), in which M = Mn, Fe and Zn (Scheme 1). In particular, the evaluation of the ability of these materials as photoelectrocatalysts for the hydrogen evolution reaction (HER) will lead to a better understanding of their potential in solar-driven processes for clean energy production.

2. Materials and methods

2.1. Chemicals

Crystals $MPSe_3$, i.e. $MnPSe_3$, $FePSe_3$, and $ZnPSe_3$, were purchased from XFNANO, China. Screen printed carbon electrodes (SPCE, SE 101) were obtained from CH Instruments, Inc. and Indium-Tin-Oxide (ITO) coated polyethylene terephthalate (PET) from Sigma Aldrich. Conductive carbon cement EM-Tec C38 was obtained from Micro to Nano. Potassium hexacyanoferrate (III) (99%) and potassium chloride (analytical grade) were purchased from Merck. Sulfuric acid 96% was obtained from Penta, Czech Republic. All solutions were prepared in deionized water with a resistivity of 18 MΩ cm.

2.2. Materials characterization

Morphological characterization of the crystals was carried out using a scanning electron microscope (SEM) TESCAN LYRA3 with an accelerating voltage of 10 kV. The elemental analysis was obtained from energy-dispersive X-ray spectroscopy (EDS, Bruker XFlash 5010), using an accelerating voltage 20 kV. X-ray photoelectron spectroscopy (XPS) was used to evaluate the surface chemical composition. The obtained spectra were calibrated against the carbon peak C 1s (285 eV) using the CasaXPS software.

2.3. Electrochemical measurements

All electrochemical measurements were carried out using a potentiostat (PGSTAT204, Metrohm Autolab, The Netherlands) controlled by NOVA software (version 2.1), in a three-electrode configuration. A platinum wire was used as counter electrode and Ag/AgCl (1 M KCl) as reference electrode. The working electrode was varied accordingly.

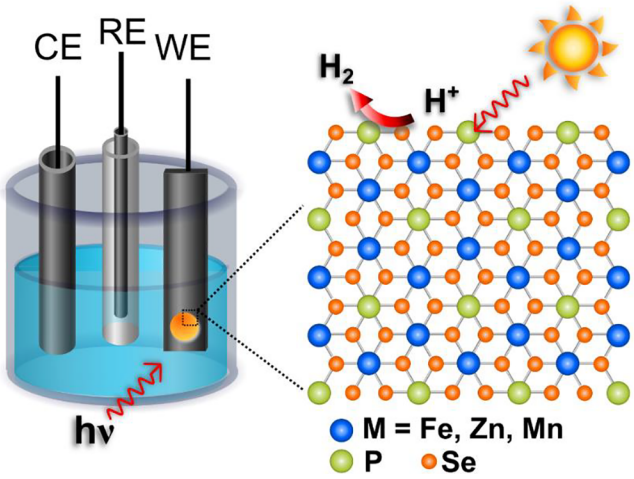

Scheme 1. Schematic illustration of the approach used to evaluate the photoelectrochemical performances of $MPCh_3$.

Cyclic voltammetry measurements were performed using $MPSe_3$ on SPCE as working electrode in 10 mM $Fe(CN)_6^{3-}$ and 0.1 M KCl electrolyte with a scan rate of 0.1 V/s.

Photocurrent measurement. Crystals of $MPSe_3$ (Figure S3) were attached to an ITO coated PET via conductive carbon tape and used as working electrodes. Chronoamperometry measurements were performed in 10 mM $Fe(CN)_6^{3-}$ and 0.1 M KCl electrolyte, applying 1 V vs. Ag/AgCl. During the experiments, the light was switched on/off at regular intervals. The illumination source was a customized LED (LZ4-40R208, LedEngin Inc.) setup that emits the wavelength 660 nm (≈40 mW/cm^2). Similar measurements were also carried out in 0.5 M H_2SO_4 electrolyte, applying −0.5 V vs. RHE. The $MPSe_3$ crystals were attached to SPCE with conductive carbon cement.

Photo-electrocatalytic hydrogen evolution measurement. The $MPSe_3$ crystals on SPCE were further used for the hydrogen evolution reaction (HER), with and without illumination. Linear sweep voltammetry (LSV) measurements were performed in 0.5 M H_2SO_4 electrolyte with a scan rate of 2 mV/s.

3. Results and discussion

The layered $MPSe_3$ materials were firstly characterized before moving to the investigation as photoelectrocatalysts for the hydrogen evolution reaction (HER). The morphology of metal selenophosphites ($MPSe_3$) crystals, namely, $MnPSe_3$, $FePSe_3$, and $ZnPSe_3$, were observed by scanning electron microscopy (SEM) (Fig. 1). All the crystals showed a structure with several stacked layers with different thicknesses, typical of the bulk 2D material. The atomic ratio between the chalcogen and the transition metal (Se/M) and the phosphorous and the metal (P/M) were calculated based on the elemental analyses using energy-dispersive X-ray spectroscopy (EDS). The EDS spectra and the distribution of the atomic % are reported in Figure S1. For all the crystals, the Se/M ratio is ~3, and the P/M ratio is ~1, which support the presence of $MPSe_3$.

The surface chemical composition of the $MPSe_3$ was further investigated using X-ray photoelectron spectroscopy (XPS). The obtained survey spectra and the key XPS peak of each element are shown in Figure S2. The presence of C 1s and O 1s peaks in all the crystals can be derivated from the adventitious carbon and oxygen as well as the carbon tape used to hold the samples for measurement. The survey spectra show that all the expected element (P, Se, and the respective metal) were detected in the analyzed crystals, confirming the observation from EDS in Figure S1.

To evaluate the electrochemical properties of the $MPSe_3$, the crystals were supported on screen printed carbon electrodes (SPCE) using conductive carbon cement. Cyclic voltammetry measurements of the $MPSe_3$ were carried out in 10 mM $Fe(CN)_6^{3-}$ and 0.1 M KCl electrolyte. The CV curves are shown in Fig. 2 and the difference between the anodic and cathodic peak potential (ΔE_p) was calculated from the voltammograms obtained. This parameter gives the information regarding the reversibility of the process: smaller ΔE_p corresponds to a more reversible electrochemical process [35]. The bare SPCE has a ΔE_p of 278 mV, and among the $MPSe_3$, $MnPSe_3$ has the lowest peak separation (149 mV), followed by $ZnPSe_3$ (154 mV) and $FePSe_3$ (252 mV).

To probe the photoelectrochemical performances, chronoamperometry experiments were carried out in the same media at the fixed potential of 1 V vs. Ag/AgCl, switching on and off the source of light (660 nm) at regular intervals. As shown in Fig. 3, the exposure to light caused an increment of the current density for all the crystals. The bare electrode does not show considerable changes in current during exposure to the light. $FePSe_3$ has the highest variation of current density after illumination, on average about 10 nA/cm^2. For $MnPSe_3$ and $ZnPSe_3$, the values are similar, approximately about 2.5 nA/cm^2. Moreover, a peak in the first seconds of illumination was observed for $ZnPSe_3$. This phenomenon is related to the recombination of the photogenerated charge carriers, that can happened for different reasons, including slow electron transport, accumulation of holes near the

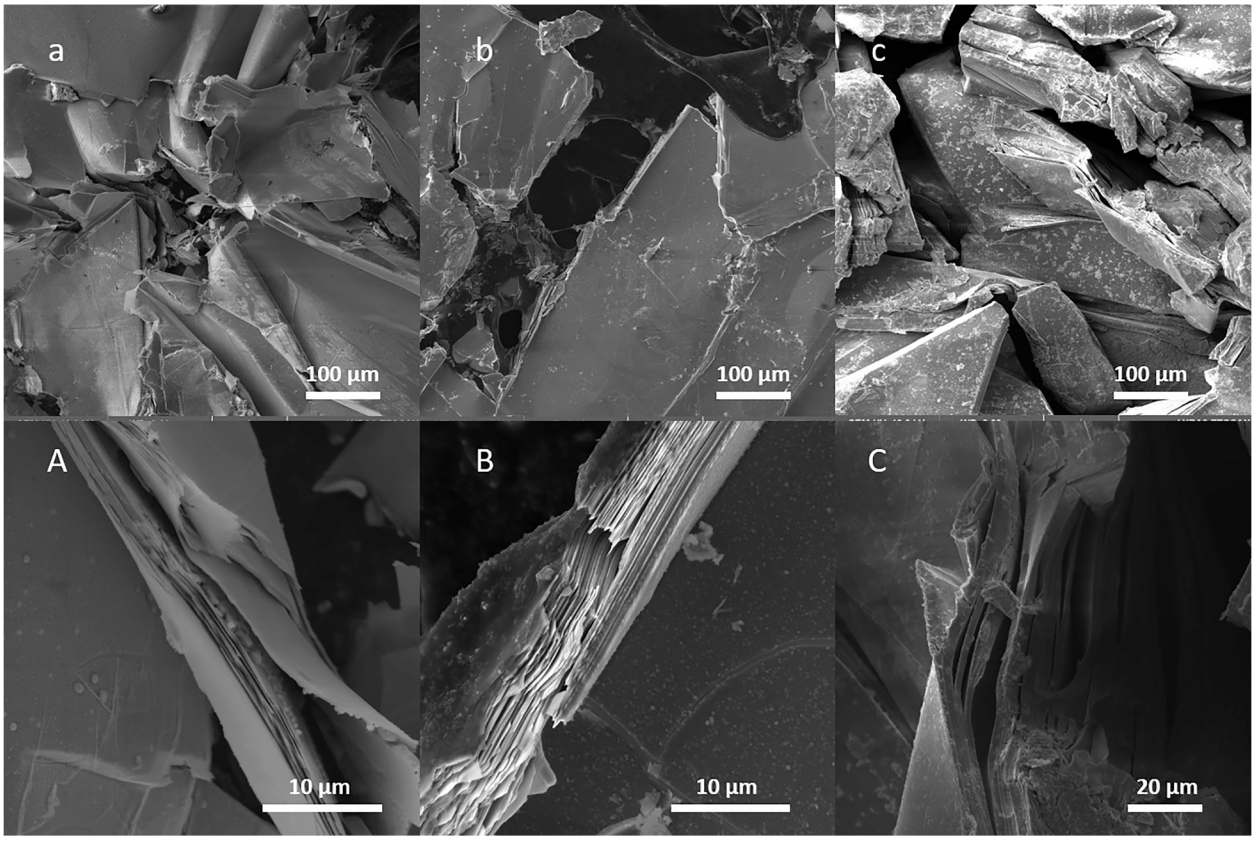

Fig. 1. SEM images of (a, A) $MnPSe_3$, (b, B) $FePSe_3$, (c, C) $ZnPSe_3$ crystals with different magnifications.

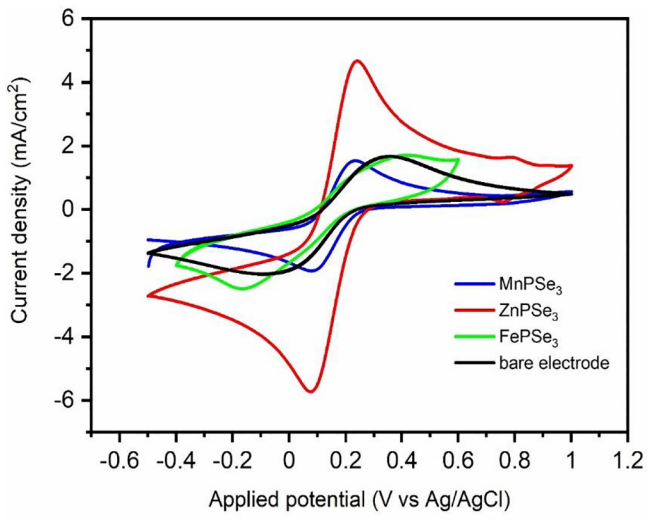

Fig. 2. Cyclic voltammograms of 10 mM $Fe(CN)_6^{3-}$ at $MPSe_3$ in 0.1 M KCl electrolyte, scan rate 0.1 V/s, screen printed carbon electrode as specimen current collector.

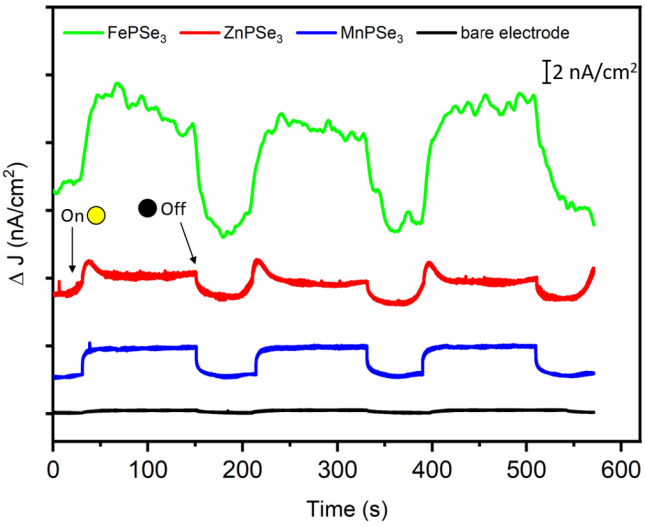

Fig. 3. Photoelectrochemical response of the $MPSe_3$ and bare electrode (as control) to visible light (660 nm) in 10 mM $Fe(CN)_6^{3-}$ and 0.1 M KCl electrolyte, applying 1 V vs. Ag/AgCl.

surface, etc. [36–38]. In general, the results obtained from the photocurrent experiment suggest that the crystals are photoactive in the visible spectral region.

Subsequently, we evaluate the photo-assisted hydrogen evolution of the three $MPSe_3$ crystals. Linear sweep voltammetry (LSV) was performed in 0.5 M H_2SO_4 with and without illumination. The overpotential at -10 mA/cm^2 has been used to compare the polarization curves obtained. The bare screen-printed carbon electrode (SPCE) is the one that shows the most deficient HER activity with an overpotential value of almost 1000 mV. The crystal trend is the same in the presence or absence of light and indicates that $ZnPSe_3$ is the material with higher catalytic activity for HER. However, all the $MPSe_3$ have a better performance with irradiation (Fig. 4A), proving the potentiality of these compounds as photocatalyst for HER. In particular, $ZnPSe_3$ is the one with the lowest overpotential (569 mV), followed by $MnPSe_3$ (655 mV) and $FePSe_3$ (740 mV). Among the three $MPSe_3$, $FePSe_3$ shows the largest improvement with illumination, with a reduced overpotential of 78 mV. $MnPSe_3$ and $ZnPSe_3$ show a decrease of the overpotential of 48 mV and

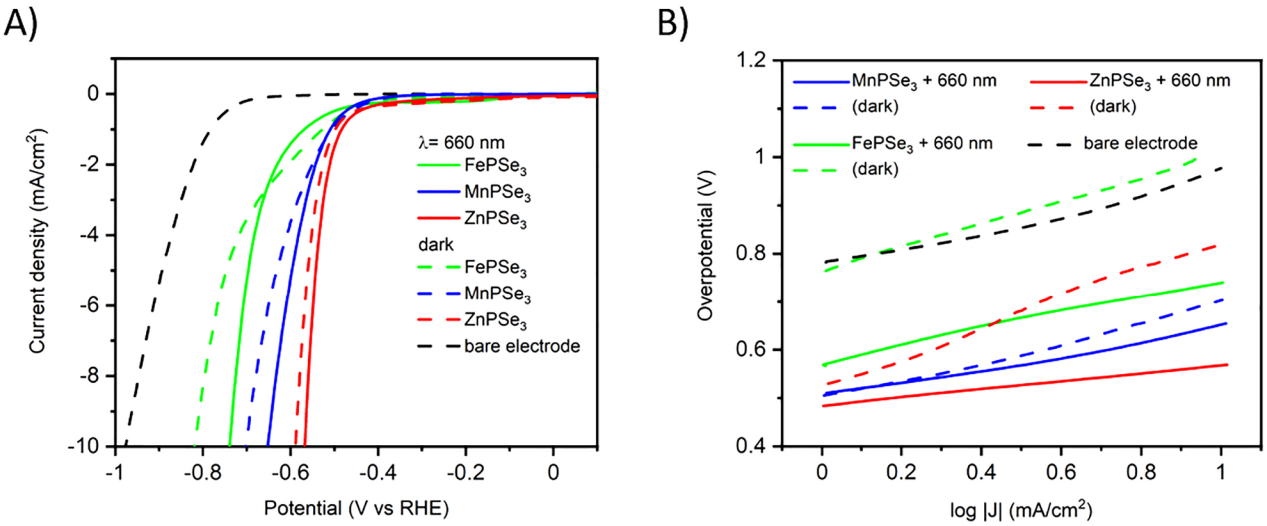

Fig. 4. Photo-electrocatalytic activity of $MPSe_3$ layered compounds evaluation for the hydrogen evolution reaction (HER). A) Linear sweep voltammograms of $MPSe_3$ and bare electrode (as control) recorded in the absence (dashed lines) and in the presence of illumination (solid lines, 660 nm) and B) corresponding Tafel plot, extrapolated from A).

44 mV respectively. These results corroborates with recent studies that report a theoretical [39] and experimental [40] band gap of ~1.5 eV for $FePSe_3$ and the consequent higher activity within the red portion of the visible spectrum. The band gaps reported for $ZnPSe_3$ and $MnPSe_3$ are 2.2–2.3 eV [40,41] and 2.2–2.9 eV [39,40], respectively, which suggest the higher activity might occur at shorter wavelength regions (<550 nm). This fact is confirmed by the absorption spectra of these compounds [40], in which the absorption of $ZnPSe_3$ and $MnPSe_3$ are confined in the range from 250 nm to 500 nm whereas $FePSe_3$ possesses an extended region up to 650 nm.

Tafel plot, represented in Fig. 4B, has been extrapolated from the LSV curves in Fig. 4A. The curves obtained by plotting the logarithm of the current density against the overpotential were used for linear fitting to obtain the Tafel slope. This value indicates the potential required to increase the current density of one order of magnitude [42]. This means that smaller overpotential and Tafel values indicate better electrocatalytic performance since less energy is required to increase the current density. In this case, the illumination catalyzes the hydrogen evolution hence decreases the Tafel slope for all the crystals. The values obtained in the presence of light are lower than the bare SPCE and, in particular, $ZnPSe_3$ is the one that shows the most significant decrease in Tafel slope value (from 315 mV/dec to 83 mV/dec), followed by $FePSe_3$ (from 240 mV/dec to 171 mV/dec) and $MnPSe_3$ (from 202 mV/dec to 143 mV/dec). The large change in the slope value observed for $ZnPSe_3$ can indicate that the rate determining step of the HER reaction is different during the exposure to the visible light. In fact, Tafel slope (b) is usually taken as an indicator of the possible reaction pathway and also to identify the limiting step of the reaction. It is known that HER in acidic media consists of two steps, adsorption and desorption. Moreover, the hydrogen desorption can proceed through two different pathways, given by Equations (1)–(3) [43,44]:

Adsorption (Volmer step):

$$H_3O^+ + e^- \rightarrow H_{ads} + H_2O;\ b \approx 118\ \text{mV/dec} \quad (1)$$

Desorption (Heyrovsky step):

$$H_{ads} + H_3O^+ + e^- \rightarrow H_2 + H_2O;\ b \approx 39\ \text{mV/dec} \quad (2)$$

Desorption (Tafel step):

$$H_{ads} + H_{ads} \rightarrow H_2;\ b \approx 29\ \text{mV/dec} \quad (3)$$

In general, for values above 118 mV/dec the determining step is the discharge reaction, or Volmer reaction, and for lower values (≈39 mV/dec for Heyrovsky reaction and ≈29.5 mV/dec for Tafel reaction) the desorption processes are the rate-determining ones [43,44].

To validate the photo-assisted catalytic effect, the photocurrent experiment was repeated in acidic media, mimicking the conditions for HER to confirm the instant photoresponse (Fig. 5). Considering the results obtained from polarization curves, we selected a potential of −0.5 V vs. RHE for chronoamperometry measurement. The results in Fig. 5 show that all the $MPSe_3$ present an instant increase in current density when exposed to the light, as well as rapid decrease when light is removed. This suggests that the photocatalytic effect is larger than the contribution from any possible convection phenomena. In particular, $FePSe_3$ and $ZnPSe_3$ show a significant change in current when exposed to light. $MnPSe_3$ is again the crystal which is less responsive to light at this particular wavelength region. Overall, the photocurrent is significantly higher compared with those obtained in a neutral media in Fig. 3. This fact can be explained considering that the measurement conducted in $Fe(CN)_6^{3-}$ involves a simple one-electron transfer reaction that is

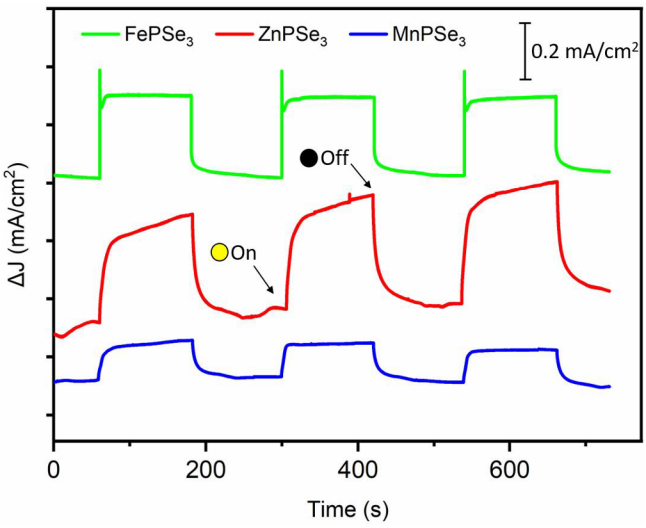

Fig. 5. Photoelectrochemical activity of layered $MPSe_3$ evaluation for the hydrogen evolution reaction. Photoresponse of the $MPSe_3$ to visible light (660 nm) in 0.5 M H_2SO_4, applying −0.5 V vs. RHE.

usually employed to evaluate the electrochemical properties of the working electrode [45]. On the other hand, the responses from the measurement in the acidic media are from a more complex reaction, as above-mentioned, in which a lot of factors can contribute to the increase in current, like the catalytic properties of the different materials toward the hydrogen generation.

4. Conclusion

In summary, we have investigated transition-metal selenophosphites crystals, $MnPSe_3$, $FePSe_3$ and $ZnPSe_3$, and we tested their performances as photoelectrocatalysts for the hydrogen evolution reaction. All the crystals showed excellent photoelectrocatalytic response during illumination with visible light (660 nm). $ZnPSe_3$ is the one that exhibited the lowest overpotential for HER and the higher response to the light during photocurrent experiments in acidic media. For this reason, among the crystals in this work, it is the most promising for the photocatalyzed production of hydrogen.

Authors contributions

M.S. performed the photoelectrochemical characterization, SEM-EDS, XPS, data analysis, and wrote the article. S.N. helped in photoelectrochemical characterization and reviewing the manuscript. M.P. came up with the idea of the project and supervised the research.

Declaration of Competing Interest

The authors declare that they have no known competing financial interests or personal relationships that could have appeared to influence the work reported in this paper.

Acknowledgment

M.P. acknowledges the financial support by the Grant Agency of the Czech Republic (GACR EXPRO: 19-26896X). M.S. acknowledges the Brno Ph.D. Talent scholarship funded by the Brno City Municipality, and the project Quality Internal Grants of BUT (KInG BUT), Reg. No. CZ.02.2.69 / 0.0 / 0.0 / 19_073 / 0016948, which is financed from the OP RDE. M.S. and S.N. thank the support of CzechNanoLab Research Infrastructure (LM2018110, MEYS CR).

Appendix A. Supplementary data

Supplementary data to this article can be found online at https://doi.org/10.1016/j.elecom.2021.107077.

References

[1] K. Maeda, T.E. Mallouk, Bull. Chem. Soc. Jpn. 92 (2018) 38–54, https://doi.org/10.1246/bcsj.20180258.
[2] I. Roger, M.A. Shipman, M.D. Symes, Nat. Rev. Chem. 1 (2017) 0003, https://doi.org/10.1038/s41570-016-0003.
[3] S. Styring, Faraday Discuss. 155 (2012) 357–376, https://doi.org/10.1039/c1fd00113b.
[4] X. Liu, S. Zhang, S. Guo, B. Cai, S.A. Yang, F. Shan, M. Pumera, H. Zheng, *Advances of 2D bismuth in energy sciences*, Chem. Soc. Rev. 49 (2020) 263–285, https://doi.org/10.1039/C9CS00551J.
[5] T.F. Jaramillo, K.P. Jørgensen, J. Bonde, J.H. Nielsen, S. Horch, I. Chorkendorff, Science 317 (2007) 100–102, https://doi.org/10.1126/science.1141483.
[6] X. Chia, M. Pumera, Chem. Soc. Rev. 47 (2018) 5602–5613, https://doi.org/10.1039/c7cs00846e.
[7] X. Chia, M. Pumera, Nat. Catal. 1 (2018) 909–921, https://doi.org/10.1038/s41929-018-0181-7.
[8] M.P. Browne, V. Urbanova, J. Plutnar, F. Novotný, M. Pumera, J. Mater. Chem. A 8 (2020) 1120–1126, https://doi.org/10.1039/c9ta11949c.
[9] W. Wang, M. Xu, X. Xu, W. Zhou, Z. Shao, Angew. Chemie - Int. Ed. 59 (2020) 136–152, https://doi.org/10.1002/anie.201900292.
[10] S. Wang, G. Liu, L. Wang, Chem. Rev. 119 (2019) 5192–5247, https://doi.org/10.1021/acs.chemrev.8b00584.
[11] N. Roy, N. Suzuki, C. Terashima, A. Fujishima, Bull. Chem. Soc. Jpn. 92 (2019) 178–192, https://doi.org/10.1246/bcsj.20180250.
[12] K.S. Novoselov, A.K. Geim, S.V. Morozov, D. Jiang, Y. Zhang, S.V. Dubonos, I. V. Grigorieva, A.A. Firsov, Science 306 (2004) 666–669, https://doi.org/10.1126/science.1102896.
[13] B. Hinnemann, P.G. Moses, J. Bonde, K.P. Jørgensen, J.H. Nielsen, S. Horch, I. Chorkendorff, J.K. Nørskov, J. Am. Chem. Soc. 127 (2005) 5308–5309, https://doi.org/10.1021/ja0504690.
[14] V. Nicolosi, M. Chhowalla, M.G. Kanatzidis, M.S. Strano, J.N. Coleman, Science 340 (2013) 72–75, https://doi.org/10.1126/science.1226419.
[15] O. Mashtalir, M.R. Lukatskaya, M.Q. Zhao, M.W. Barsoum, Y. Gogotsi, Adv. Mater. 27 (2015) 3501–3506, https://doi.org/10.1002/adma.201500604.
[16] Z. Yu, J. Peng, Y. Liu, W. Liu, H. Liu, Y. Guo, J. Mater. Chem. A 7 (2019) 13928–13934, https://doi.org/10.1039/c9ta03256h.
[17] O. Mashtalir, M. Naguib, V.N. Mochalin, Y. Dall'Agnese, M. Heon, M.W. Barsoum, Y. Gogotsi, Nat. Commun. 4 (2013) 1716, https://doi.org/10.1038/ncomms2664.
[18] C.C. Mayorga-Martinez, Z. Sofer, D. Sedmidubský, Š. Huber, A.Y.S. Eng, M. Pumera, A.C.S. Appl, ACS Appl. Mater. Interfaces 9 (2017) 12563–12573, https://doi.org/10.1021/acsami.6b16553.
[19] R. Gusmão, Z. Sofer, D. Sedmidubský, Š. Huber, M. Pumera, ACS Catal. 7 (2017) 8159–8170, https://doi.org/10.1021/acscatal.7b02134.
[20] R. Gusmão, Z. Sofer, M. Pumera, Adv. Funct. Mater. 29 (2019) 1805975, https://doi.org/10.1002/adfm.201805975.
[21] P. Sen, K. Alam, T. Das, R. Banerjee, S. Chakraborty, J. Phys. Chem. Lett. 11 (2020) 3192–3197, https://doi.org/10.1021/acs.jpclett.0c00710.
[22] D. Mukherjee, P.M. Austeria, S. Sampath, ACS Energy Lett. 1 (2016) 367–372, https://doi.org/10.1021/acsenergylett.6b00184.
[23] F. Wang, T.A. Shifa, P. Yu, P. He, Y. Liu, F. Wang, Z. Wang, X. Zhan, X. Lou, F. Xia, J. He, Adv. Funct. Mater. 28 (2018) 1802151, https://doi.org/10.1002/adfm.201802151.
[24] R. Gusmão, Z. Sofer, M. Pumera, Angew. Chemie - Int. Ed. 58 (2019) 9326–9337, https://doi.org/10.1002/anie.201810309.
[25] M.A. Susner, M. Chyasnavichyus, M.A. McGuire, P. Ganesh, P. Maksymovych, Adv. Mater. 29 (2017) 1602852, https://doi.org/10.1002/adma.201602852.
[26] D.J. Goossens, S. Brazier-Hollins, D.R. James, W.D. Hutchison, J.R. Hester, J. Magn. Magn. Mater. 334 (2013) 82–86, https://doi.org/10.1016/j.jmmm.2013.01.023.
[27] G. Long, T. Zhang, X. Cai, J. Hu, C.W. Cho, S. Xu, J. Shen, Z. Wu, T. Han, J. Lin, J. Wang, Y. Cai, R. Lortz, Z. Mao, N. Wang, ACS Nano. 11 (2017) 11330–11336, https://doi.org/10.1021/acsnano.7b05856.
[28] T. Masubuchi, H. Hoya, T. Watanabe, Y. Takahashi, S. Ban, N. Ohkubo, K. Takase, Y. Takano, J. Alloys Compd. 460 (2008) 668–674, https://doi.org/10.1016/j.jallcom.2007.06.063.
[29] R. Kumar, R.N. Jenjeti, M.P. Austeria, S. Sampath, J. Mater. Chem. C 7 (2019) 324–329, https://doi.org/10.1039/c8tc05011b.
[30] K. Maeda, K. Domen, J. Phys. Chem. Lett. 1 (2010) 2655–2661, https://doi.org/10.1021/jz1007966.
[31] A. Kudo, Y. Miseki, Chem. Soc. Rev. 38 (2009) 253–278, https://doi.org/10.1039/b800489g.
[32] J. Ran, J. Zhang, J. Yu, M. Jaroniec, S.Z. Qiao, Chem. Soc. Rev. 43 (2014) 7787–7812, https://doi.org/10.1039/c3cs60425j.
[33] K. Takanabe, ACS Catal. 7 (2017) 8006–8022, https://doi.org/10.1021/acscatal.7b02662.
[34] M. Matsuoka, M. Kitano, M. Takeuchi, K. Tsujimaru, M. Anpo, J.M. Thomas, Catal. Today. 122 (2007) 51–61, https://doi.org/10.1016/j.cattod.2007.01.042.
[35] N. Elgrishi, K.J. Rountree, B.D. McCarthy, E.S. Rountree, T.T. Eisenhart, J. L. Dempsey, J. Chem. Educ. 95 (2018) 197–206, https://doi.org/10.1021/acs.jchemed.7b00361.
[36] R. van de Krol, Photoelectrochemical measurements, in: R. van de Krol, M. Grätzel (Eds.), Photoelectrochemical Hydrogen Production, Springer, Boston, MA, 2012, pp. 69–117, https://doi.org/10.1007/978-1-4614-1380-6_3.
[37] P. Salvador, C. Gutiérrez, J. Electroanal. Chem. 160 (1984) 117–130, https://doi.org/10.1016/S0022-0728(84)80119-9.
[38] L.M. Peter, J. Li, R. Peat, J. Electroanal. Chem. 165 (1984) 29–40, https://doi.org/10.1016/S0022-0728(84)80084-4.
[39] B.L. Chittari, Y. Park, D. Lee, M. Han, A.H. Macdonald, E. Hwang, J. Jung, Phys. Rev. B 94 (2016), 184428, https://doi.org/10.1103/PhysRevB.94.184428.
[40] F.M. Oliveira, J. Paštika, L.S. Pires, Z. Sofer, R. Gusmão, Adv. Mater. Interfaces 8 (2021) 2100294, https://doi.org/10.1002/admi.202100294.
[41] J. Liu, X.B. Li, D. Wang, W.M. Lau, P. Peng, L.M. Liu, J. Chem. Phys. 140 (2014), 054707, https://doi.org/10.1063/1.4863695.
[42] C. Brett, Fundamentals of electrochemistry, in: A.A. Vives (Ed.), Piezoelectric Transducers and Applications, Springer, Berlin, Heidelberg, 2009, pp. 223–239, https://doi.org/10.1007/978-3-540-77508-9_8.
[43] M. Zeng, Y. Li, J. Mater. Chem. A 3 (2015) 14942–14962, https://doi.org/10.1039/c5ta02974k.
[44] C.G. Morales-Guio, L.A. Stern, X. Hu, Chem. Soc. Rev. 43 (2014) 6555–6569, https://doi.org/10.1039/c3cs60468c.
[45] A.J. Bard, L.R. Faulkner, Electrochemical methods: Fundamentals and Applications, 2nd ed., John Wiley & Sons Inc, New York, 2001.

6. Fluorinated MAX phases for photoelectrochemical hydrogen evolution

Published paper included in this chapter:

Sanna, M.; Ng, S.; Vaghasiya, J. V.; Pumera, M. Fluorinated MAX Phases for Photoelectrochemical Hydrogen Evolution. *ACS Sustain. Chem. Eng.* **2022**, *10* (8), 2793–2801.

The results obtained were presented at the conference: **X NyNA 2022: International Conference on Analytical Nanosciences and Nanotechnologies and at the CEITEC PhD Retreat 2022.**

6.1. Motivation for the study

The primary motivation behind this research is the noticeable disparity in the utilization of MAX compared to their derivative MXene counterparts. While MXenes have garnered significant attention and boast a rich literature base regarding their applications in various electrochemical processes, MAX have received comparatively less exploration. Existing studies predominantly focus on the physical attributes of MAX rather than their potential applications in electrochemical energy conversion. Nonetheless, MAX present a distinctive blend of metallic and ceramic properties, rendering them captivating candidates for electrocatalytic processes. Their attributes include commendable thermal and electrical conductivity, minimal thermal expansion coefficients, remarkable stability, and resistance to chemical degradation.

Furthermore, the enhancement of the chemical and optoelectronic properties of 2D layered materials is often pursued through doping or surface engineering strategies. Chemical modification, like fluorination, is particularly interesting, as it offers an interesting way of

tailoring the physical and optical characteristics crucial for photoelectrochemical applications. This study endeavors to understand the impact of fluorination on four distinct MAX, meticulously analyzing alterations in their morphology, elemental composition, and crystalline structure. Subsequently, both untreated MAX and their fluorinated counterparts will undergo thorough evaluation and comparison as potential photoelectrocatalysts for the HER.

6.2. Paper conclusion

The study focused on the impact of fluorination on various MAX compounds, including Ta_2AlC, Cr_2AlC, Ti_2AlC, and Ti_3AlC_2, with a focus on their structural, morphological, and performance alterations as potential photoelectrocatalysts for hydrogen generation. Exposure to fluorine gas induced notable changes in the morphology of the treated compounds, leading to partial delamination between layers and extensive formation of oxyfluoride species on their surfaces. Notably, F-Cr_2AlC exhibited a significant surface fluorination with minimal morphological change, possibly due to its reported higher resistance to oxidation and exfoliation compared to other MAX compounds studied. When subjected to illumination by a 660 nm light source, all MAX and F-MAX compounds displayed enhanced photoelectrocatalytic activity. Particularly noteworthy was the pronounced improvement observed in F-Ti_2AlC and F-Ti_3AlC_2. This enhancement was mainly attributed to the presence of photoactive oxyfluoride ($TiOF_2$) species on their surfaces following fluorination, as confirmed by morphological and structural analyses. Despite the absence of oxyfluorides, Cr_2AlC and F-Cr_2AlC exhibited the lowest overpotential and Tafel slope values in their respective categories, with the former showing superior performance and enhanced photoelectrocatalytic effects compared to Cr_2AlC. Further insights into the properties of Cr_2AlC are necessary to elucidate the role of fluorine within its structure. Moreover, the unexpected photoactivity observed in MAX compounds, traditionally considered to exhibit metallic behavior, suggests intriguing avenues for future research. Through this study, we present, for

the first time, the photoelectrocatalytic properties of MAX and F-MAX compounds for energy conversion applications. Despite their performances being lower than some benchmark materials like MoS_2 and MXene, we believe that a deeper understanding of these compounds and the effects of fluorination can pave the way for the development of promising new photoelectrocatalysts. For instance, given that MAX compounds are primarily used to obtain MXenes, and pure MXenes typically lack photoactivity, there is exciting potential to explore the synthesis of photoactive MXenes from fluorinated MAX through exfoliation processes.

6.3. Author contribution

I carried out the elemental analysis using XPS and performed all the photoelectrochemical measurements. Moreover, I performed the data analysis, plotted the results, and wrote the first draft of the manuscript.

ACS Sustainable Chemistry & Engineering

pubs.acs.org/journal/ascecg

Research Article

Fluorinated MAX Phases for Photoelectrochemical Hydrogen Evolution

Michela Sanna, Siowwoon Ng, Jayraj V. Vaghasiya, and Martin Pumera*

Cite This: *ACS Sustainable Chem. Eng.* 2022, 10, 2793−2801

Read Online

ACCESS | Metrics & More | Article Recommendations | Supporting Information

ABSTRACT: Photoelectrochemical generation of hydrogen from water is considered to be the most appealing solution for the replacement of fossil fuels as a source of energy. For this reason, the study of novel and affordable materials with high energy conversion efficiencies is currently a crucial objective for the scientific community. Chemical modification of two-dimensional (2D) and layered materials, such as fluorination, can play a decisive role in tuning the properties for energy-related applications, as it was documented in the past by fluorination of graphite and graphene. MAX phases (MAX) are a class of layered ternary compounds that is well known for their interesting physical properties but still underexplored as a photoelectrocatalyst for energy conversion. Herein, a set of MAX, namely, Ta_2AlC, Cr_2AlC, Ti_2AlC, and Ti_3AlC_2, was exposed to fluorine gas in a controlled environment and their photoelectrocatalytic properties were tested for the hydrogen evolution reaction with illumination by a visible light source of 660 nm wavelength. All of the mentioned compounds showed excellent hydrogen evolution performances under illumination, in particular after the fluorination process. Fluorinated Cr_2AlC is the phase that showed the lowest overpotential, and fluorinated Ti_2AlC and Ti_3AlC_2 showed the most prominent photoelectrocatalytic enhancement upon fluorination. The fluorinated MAX phases should find broad applications to photoelectrochemistry, as their fluorinated graphene counterparts did in the past.

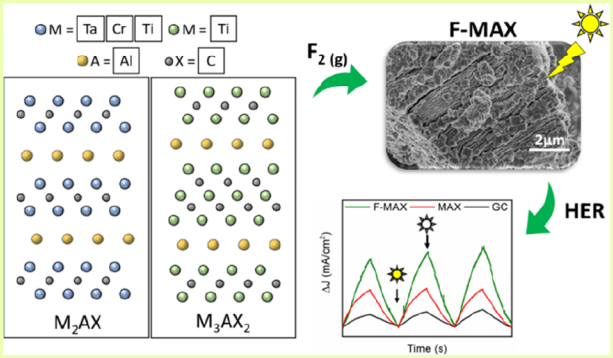

KEYWORDS: *MAX phase, fluorination, 2D layered material, photoelectrochemistry, hydrogen generation, photoelectrocatalyst*

INTRODUCTION

The limited amount of fossil fuels available on our planet, their impact on the environment, and the increasing energy consumption have raised an urge to find alternative sustainable energy sources. Nowadays, hydrogen is considered to be the perfect candidate for building a society based on clean energy production.[1,2] In fact, the combustion of this material leads to the generation of water, a harmless byproduct for land and air. However, hydrogen could be considered as an environmentally friendly alternative only if it is produced by exploiting renewable sources of energy, such as solar, wind, hydrothermal, or hydroelectric energy. Inspired by the early works on light-induced artificial photosynthesis, photoelectrochemical water splitting using solar energy is considered as one of the most promising hydrogen generation methods.[3−5] Investigating novel materials with high energy conversion efficiencies and low production cost is currently a crucial objective for scientists.

Many studies are now focused on applying two-dimensional (2D) layered materials, such as graphene,[6,7] graphitic carbon nitride (g-C_3N_4),[8,9] transition metal dichalcogenides[10] and trichalcogenphosphites,[11,12] monoelemental compounds (Xenes),[13−15] and transition metal carbides (MXenes), as electrocatalysts for energy conversion. These 2D nanomaterials including MXenes, which possess high specific surface areas and fast charge-transfer kinetics, have been extensively studied in the last decade for applications in energy conversion and storage, thanks to their promising electrocatalytic properties.[16−22] MXenes are commonly synthesized from their parent MAX phases (MAX), a class of layered ternary materials with the general formula $M_{n+1}AX_n$, where M is an early transition metal, A is an element from IIIA and IVA group, X is carbon or nitrogen, and n is equal to 1, 2, or 3.[19,23−25] By applying acid treatment with aqueous hydrofluoric acid and sonication, the A element interlayer can be selectively etched and washed out from the MAX giving a set of single or multilayer MXenes that present a mix of OH-, O-, and F- functionalizations on their surface.[26,27] Exhaustive literature can be found regarding the application of MXenes and their derivates in electrochemical

Received: December 2, 2021
Revised: February 6, 2022
Published: February 18, 2022

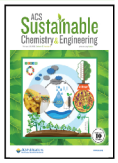

processes.[28−31] On the other hand, numerous reported studies on MAX are more focused on their physical properties, and few have been carried out to investigate their electrochemical energy-related applications.[32,33] MAX possess an uncommon combination of metallic and ceramic properties that make them an interesting candidate for electrocatalytic processes. In fact, they are good thermal and electrical conductors, have relatively low thermal expansion coefficients, show high stability, and resist chemical attacks.[24,25,34,35]

Further modifications of 2D layered materials, such as doping or surface engineering, are commonly used to enhance their chemical and optoelectronic properties.[36] In particular, chemical modification by fluorination is fascinating for photoelectrochemical applications because it can tune the physical and optical properties related to the photoresponses of 2D materials. For example, the fluorination of graphene,[37,38] phosphorene,[39] and g-C_3N_4[40] resulted in improved surface polarity, thermal, and chemical stability, but also tunable or opening of the band gap. These significant changes in the properties of 2D materials are attributed to the strong electronegativity and the large dissociation energy of fluorine.[41]

In this work, four MAX were treated with fluorine gas (F_2) in a controlled environment. Morphology, elemental composition, and crystalline phase of the fluorinated MAX phases (F-MAX) were studied. Then, MAX and F-MAX were applied and compared as phototelectrocatalyst for the hydrogen evolution reaction (HER).

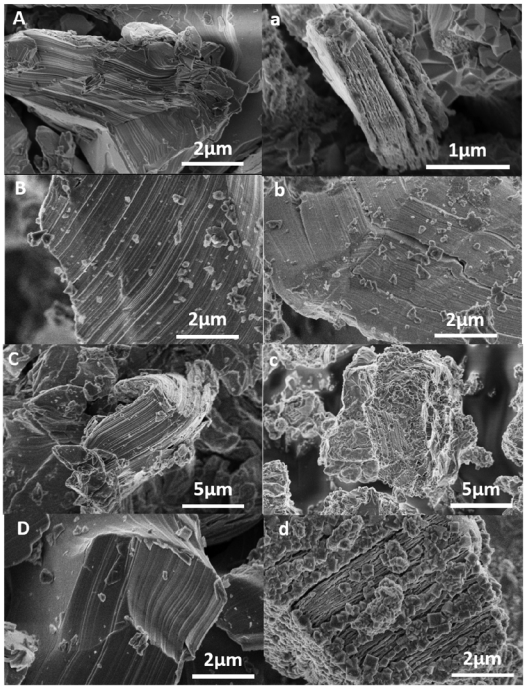

Figure 1. SEM micrographs of MAX (left column, A−D) and respective F-MAX (right column, a−d) phases (A) Ta_2AlC, (B) Cr_2AlC, (C) Ti_2AlC, and (D) Ti_3AlC_2.

RESULTS AND DISCUSSION

Four MAX, namely, Ta_2AlC, Cr_2AlC, Ti_2AlC, and Ti_3AlC_2, were exposed to F_2 gas in a controlled environment to prepare the F-MAX, F-Ta_2AlC, F-Cr_2AlC, F-Ti_2AlC, and F-Ti_3AlC_2. Different material characterizations were carried out to understand the effect of the F-treatment on the starting materials. The morphology of the MAX before and after the exposure to F_2 gas was observed by scanning electron microscopy (SEM). Micrographs of MAX (Figure 1A−D) generally show the typical 2D layered structure with really tight conformation. After the F-treatment, we observe partial delamination with consequent larger space between the layers for all F-MAX (Figure 1a,c,d) except for the layers of F-Cr_2AlC (Figure 1b) which remain quite intact. Moreover, the Ta- and Ti-based F-MAX also exhibited an extensive formation of cube-like aggregates on the surface.

Besides the change in morphology due to the fluorination process, energy-dispersive X-ray spectroscopy (EDS) was used to investigate the presence of different elements in the F-MAX. As shown in the EDS mapping (Figure 2), the expected elements, that is, the respective metal (Ta, Cr, or Ti), Al, C, and O elements are observed, which is confirmed by the EDS spectra in Figure S1. The presence of O, which is also found in the MAX, is unavoidable (evidenced by XPS of all MAX, to be discussed later). The fluorination process induces F in the material; in specific, F-Cr_2AlC exhibits the lowest amount (4.1 At %), followed by F-Ta_2AlC (6.0 At %), F-Ti_3AlC_2 (6.9 At %), and F-Ti_2AlC (11.6 At %). A detailed breakdown of all elements is included in the inset of Figure S1.

More details about the chemical composition of the MAX and F-MAX were obtained from the X-ray photoelectron spectroscopy (XPS) measurement, as shown in Figure 3. For simplicity, only the primary XPS peak of each element was labeled in the spectra. By comparing the XPS spectrum before and after the fluorination process, the main difference was the presence of an intense F 1s peak at ≈685 eV in all the F-MAX. The observation again confirms the presence of F within the F-MAX, which matches the analyses from EDS measurement. The peak position related to the other elements (metal, Al, C, and O) remained similar but with reduced intensity after the fluorination process. Note that the presence of oxygen in MAX due to the formation of oxide layers on the surface has been reported in previous works.[42,43]

X-ray diffraction (XRD) pattern of F-MAX was acquired to evaluate the crystalline phases (Figure 4). The diffractions peaks in the XRD pattern of F-Ta_2AlC, F-Ti_2AlC, and F-Ti_3AlC_2 are mainly assigned to their respective MAX and also other diffraction peaks that can be attributed to the formation of different oxyfluoride species, namely, TaO_2F and $TiOF_2$ for Ta- and Ti-based F-MAX, respectively. F-Cr_2AlC is the only phase that does not show the presence of the respective oxyfluoride, where its XRD pattern shows a prevalence of its MAX and traces of $Cr_{23}C_6$.

Based on the different material characterization techniques, we observe that the fluorination by F_2 gas on the MAX has resulted in different effects. As evidenced by EDX and XPS measurements, fluorine was successfully introduced within the MAX. The M−A bond in MAX is more chemically reactive compared to the M−X bond, and for this reason, the Al layer can be selectively etched.[19] After the exposure to F_2, most of the MAX undergo a partial etching and, as a consequence, the 2D layers are noticeably separated (Figure 1 right column). At the same time, fluorine reacted with the oxides present in the MAX to form the oxyfluoride species detected in XRD. As a confirmation, the cubic-like structures observed on the surface of F-MAX in Figure 1a,c,d can be attributed to TaO_2F and $TiOF_2$ since both possess a simple cubic crystal structure and the cubic morphology agrees with the reported works.[44,45] Despite fluorine being detected in F-Cr_2AlC, the etching effect

https://doi.org/10.1021/acssuschemeng.1c08133
ACS Sustainable Chem. Eng. 2022, 10, 2793−2801

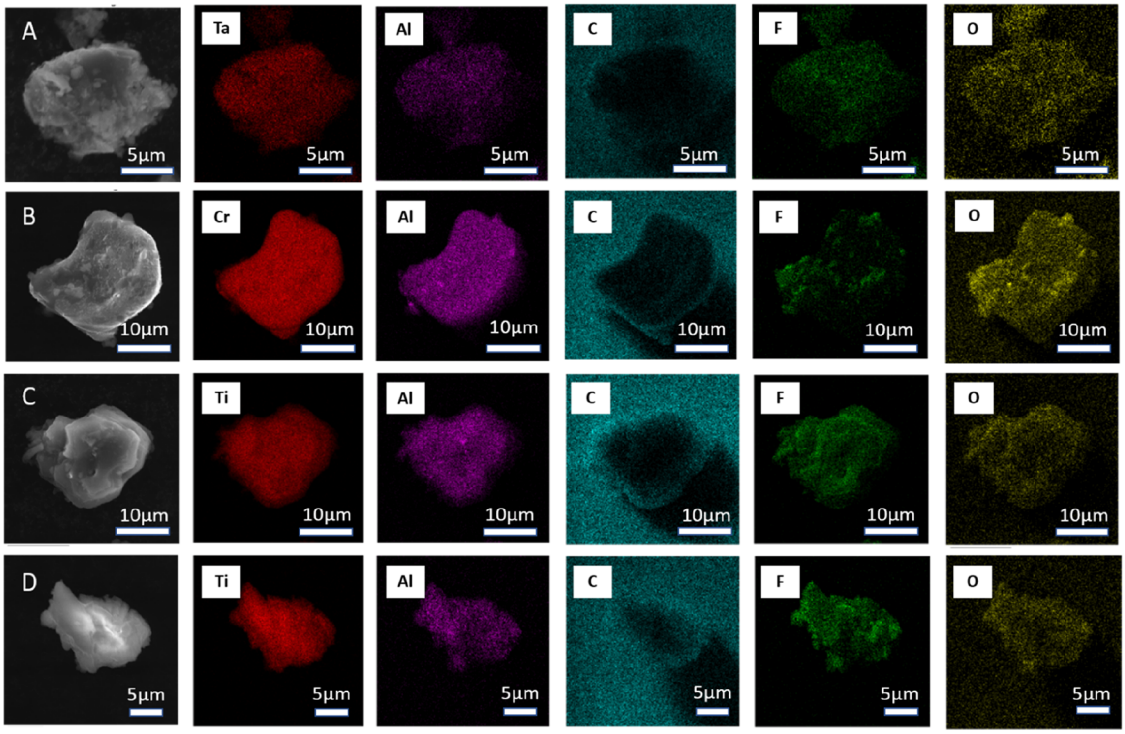

Figure 2. SEM-EDS mapping of the F-MAX phases; (A) F-Ta_2AlC, (B) F-Cr_2AlC, (C) F-Ti_2AlC, and (D) F-Ti_3AlC_2, elemental map of the respective metal (Ta, Cr or Ti), Al, C, F, and O.

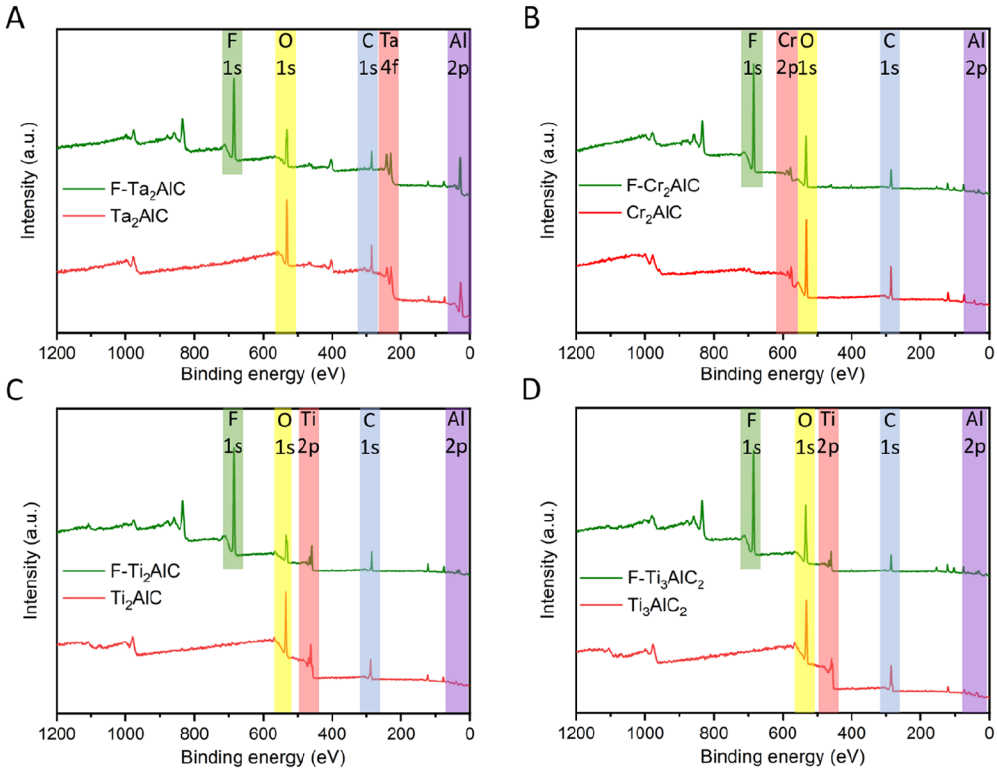

Figure 3. XPS survey spectra of MAX and F-MAX phases, (A) Ta_2AlC, (B) Cr_2AlC, (C) Ti_2AlC, and (D) Ti_3AlC_2.

on the Al layer is least prominent, with the smallest separation between layers, the lowest amount of F within the sample, and no Cr-based oxyfluoride structures were detected. The different fluorination effects can be related to the properties of individual MAX and its corresponding metal oxides. Of all MAX in this work, Cr_2AlC is more resistant to oxidation and harsh environment.[46,47] Furthermore, the etching effect is directly related to the bond strength and exfoliation energy of

https://doi.org/10.1021/acssuschemeng.1c08133
ACS Sustainable Chem. Eng. 2022, 10, 2793−2801

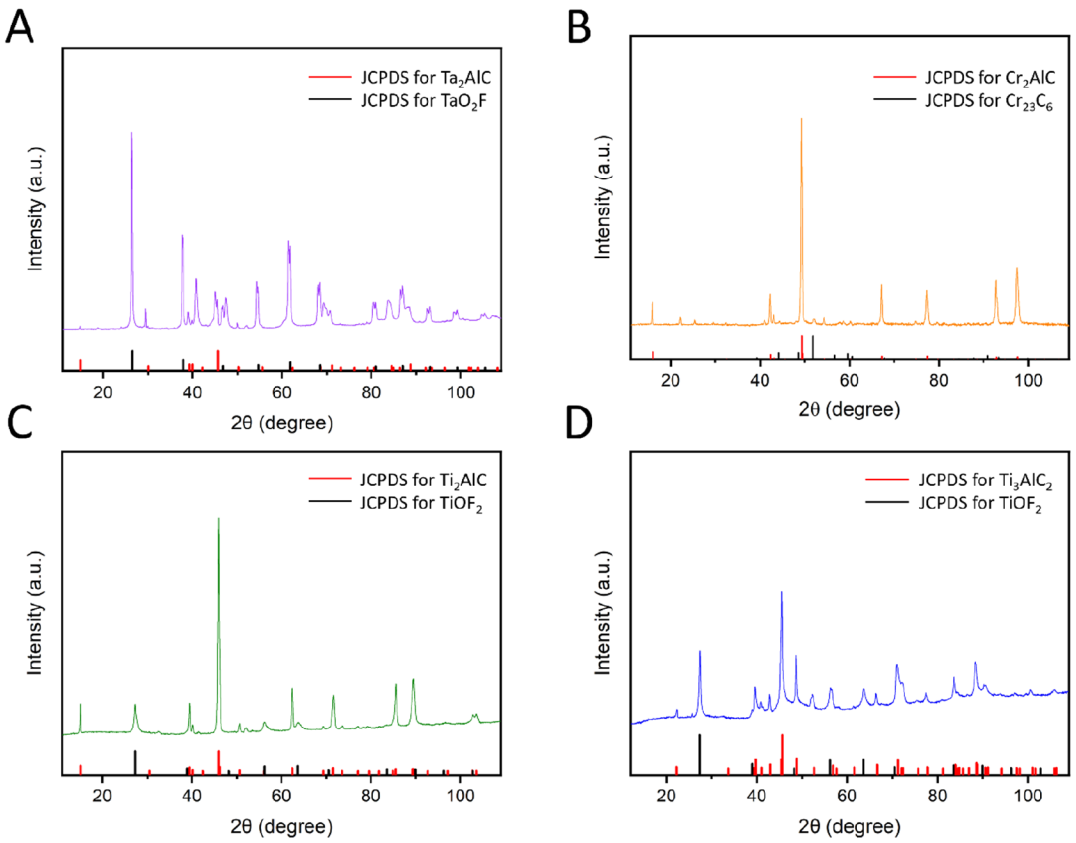

Figure 4. XRD pattern of F-MAX phases, (A) F-Ta_2AlC, (B) F-Cr_2AlC, (C) F-Ti_2AlC, and (D) F-Ti_3AlC_2.

the MAX. A recent computational work predicted that the exfoliation energy for Cr_2AlC (0.213 eV $Å^{-1}$) is higher than the one for Ta_2AlC (0.192 eV $Å^{-1}$), Ti_2AlC (0.170 eV $Å^{-1}$), and Ti_3AlC_2 (0.164 eV $Å^{-1}$),[48] which explains the least etching effect of Cr_2AlC.

We investigated the above prepared and analyzed materials as photoelectrocatalysts for HER. Linear sweep voltammetry (LSV) was performed in 0.5 M H_2SO_4 electrolyte for both MAX and F-MAX on the glassy carbon (GC) electrode with and without exposure to a light source (λ = 660 nm), and the LSV curves are shown in Figure 5. As a reference, the bare GC electrode was measured, which is known for its poor catalytic activity for HER.[49] All the MAX (red dashed lines) are more catalytically active than the blank GC as demonstrated by the lowered overpotentials, ≈808 mV for Cr_2AlC, ≈822 mV for Ta_2AlC, and ≈966 mV for both Ti-based MAX; all comparisons are made at −10 mA cm^{-2}. The higher catalytic activity of Cr_2AlC among the MAX tested in this work corroborates with a recent study.[32] Besides, Ti_2AlC and Ti_3AlC_2 exhibited similar activity as electrocatalysts for the HER, as also reported by Rosli et al.[33] Generally, all the F-MAX (green dashed lines) improved the catalytic activity by showing an even lower overpotential than the MAX, ≈715 mV for Cr_2AlC, ≈786 mV for Ta_2AlC, ≈866 mV for Ti_3AlC_2, and ≈928 mV for Ti_2AlC. The presence of the illumination during the measurements led to a decrease in the overpotential value for both MAX and F-MAX. The more prominent photoelectrocatalytic HER enhancement was recorded for F-Ti_2AlC, followed by F-Ti_3AlC_2: the overpotential was, respectively, reduced by 178 mV (to 783 mV) and 119 mV (to 747 mV) compared to the one obtained without exposure to the light. The higher photoactivity of these phases can be related to the presence of $TiOF_2$ on the surface. In fact, different studies on $TiOF_2$ reported its high photoactivity under irradiation (λ = 660 nm),[44,50] with an optical band gap of ≈3.10 eV.[51] As discussed above, the presence of the respective oxyfluoride (TaO_2F) was also detected in the F-Ta_2AlC phase. However, in this case, the overpotential of F-Ta_2AlC is lower (reduced by 88 mV) than the one observed for Ta_2AlC (reduced by 100 mV). The lower photoelectrocatalytic HER enhancement by TaO_2F than $TiOF_2$ can be related to their optical band gap. A recent study reported that TaO_2F presents an energy band value of ≈4.10 eV,[45] so it is expected to be less photoactive than $TiOF_2$ when both are exposed to the light source (660 nm) in this work. Overall, Cr_2AlC and F-Cr_2AlC presented the lowest overpotential in their respective category. In particular, under the illumination, an overpotential of 695 and 642 mV was achieved for Cr_2AlC and F-Cr_2AlC, respectively. We present a summary of overpotential values of all MAX and F-MAX with and without illumination in Figure 5a−d for clear comparison.

Furthermore, Tafel plots (Figure S2) were derived from the polarization curves in Figure 5A−D, and Tafel slope values (Table S1) were calculated by fitting the linear region of the Tafel plots. As reported in previous studies for MAX in electrocatalytic HER,[32,33] all the phases exhibited slope values greater than 100 mV dec^{-1}, so it can be inferred that the rate-limiting step for the MAX and F-MAX phases is the adsorption of hydrogen on the surface (Volmer step), that is, usually identified as limiting with slope values ≈120 mV dec^{-1} or larger. Similar to Figure 5, where Ta_2AlC and Cr_2AlC presented the lower overpotentials, both demonstrated the

https://doi.org/10.1021/acssuschemeng.1c08133
ACS Sustainable Chem. Eng. 2022, 10, 2793−2801

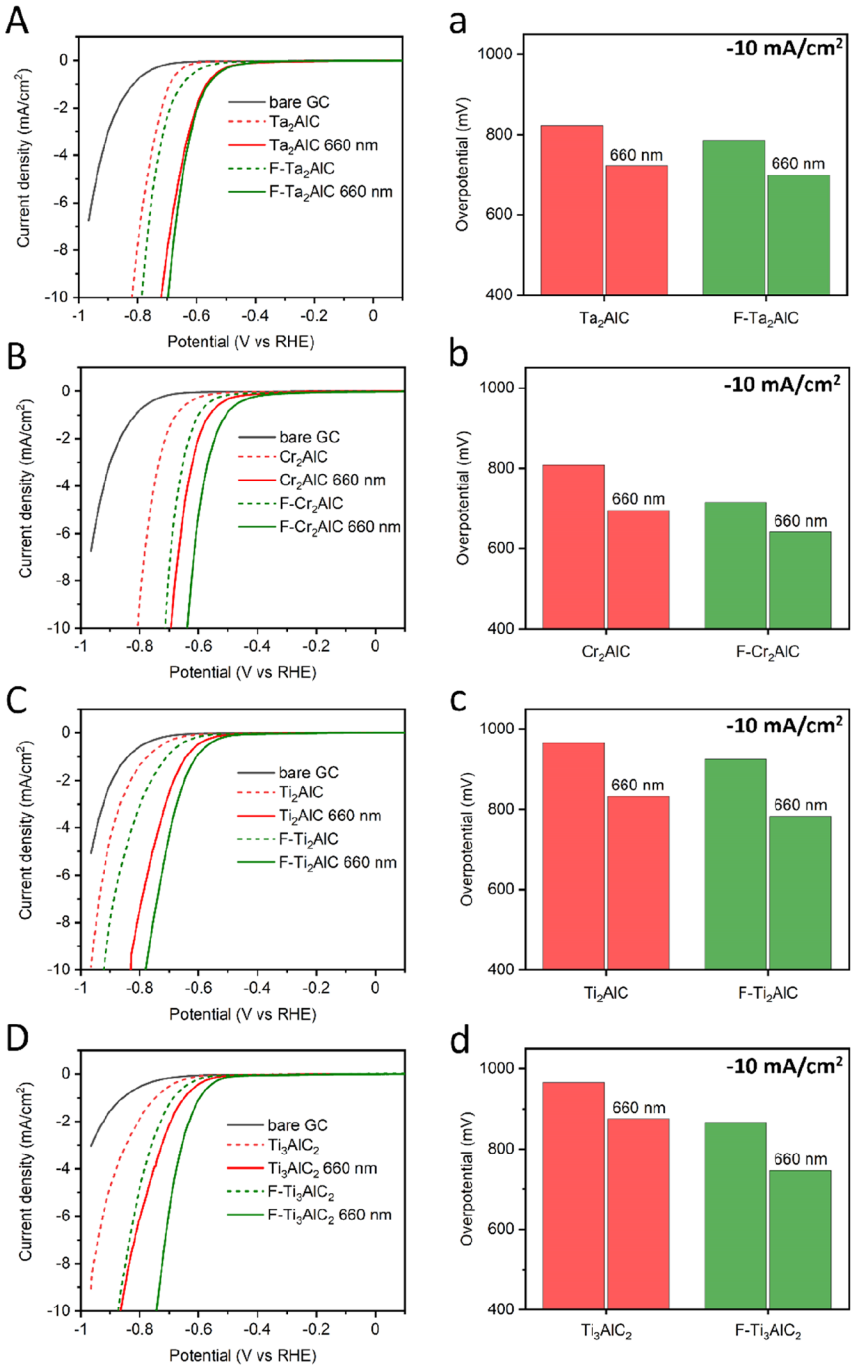

Figure 5. Linear sweep voltammograms of HER for MAX and F-MAX, (A) Ta_2AlC, (B) Cr_2AlC, (C) Ti_2AlC, and (D) Ti_3AlC_2 without and with illumination by a light source of wavelength 660 nm, measured in 0.5 M H_2SO_4 electrolyte with a scan rate of 2 mV s^{-1}. The corresponding overpotential values are at −10 mA cm^{-2} (a,b,c,d).

lowest slope values, in the range of 120−155 mV dec^{-1} with and without illumination. The Ti-based compounds generally showed higher slopes, in the range of 190−230 mV dec^{-1}. However, the Tafel slopes of the illuminated F-MAX are lower than the non-illuminated, presenting comparable values with other F-MAX, in particular, 147 mV dec^{-1} for F-Ti_3AlC_2 and 170 mV dec^{-1} for F-Ti_2AlC. As mentioned above, the photoresponse of these phases was influenced by the presence of $TiOF_2$. For this reason, we believe that the exposure of the oxyfluoride to light can play a role and influence the kinetic of the reaction.

Chronoamperometry measurements (Figure 6) were performed in the same electrolyte to validate the illumination effect observed in polarization curves, as shown in Figure 5. The light source was switched on/off during the experiment at regular intervals, and a fixed potential [−0.46 V vs reversible hydrogen electrode (RHE)] was applied. This potential value was chosen considering the results in Figure 5 at the region before the onset potential of hydrogen evolution. This is to minimize the noise of the recorded currents caused by the evolution of the bubble during the experiment (visible in the response of F-Ti_3AlC_2 in Figure 6D). Comparing the

https://doi.org/10.1021/acssuschemeng.1c08133
ACS Sustainable Chem. Eng. 2022, 10, 2793−2801

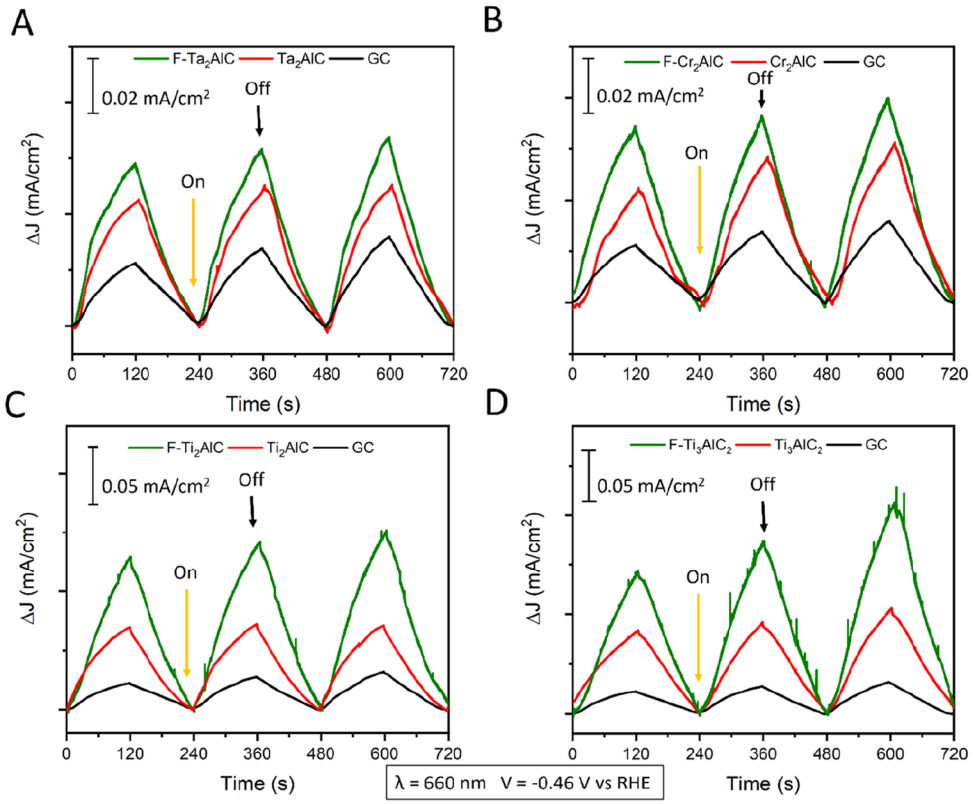

Figure 6. Chronoamperometry measurement for representation of the photoresponses of MAX and F-MAX at −0.46 V vs RHE with ON/OFF pulses under the 660 nm LED irradiation. (A) Ta_2AlC, (B) Cr_2AlC, (C) Ti_2AlC, and (D) Ti_3AlC_2.

photocurrent density of the bare GC electrode and the MAX and F-MAX allowed us to discriminate between the photothermal and the photoelectrochemical effect caused by the light exposure. In fact, all the phases showed a greater increase in current density than the GC electrode, suggesting the presence of the photoelectrocatalytic effect. The results confirmed that all F-MAX showed a larger current increment during illumination than their respective MAX. In particular, the most prominent increase in current was recorded for F-Ti_2AlC and F-Ti_3AlC_2 (0.13 and 0.15 mA cm^{-2}, respectively), which agrees with the lowered HER overpotentials with the illumination, as shown in Figure 5. Further confirmation of the photoactivity of the F-MAX was obtained comparing the UV−visible absorbance spectra of these materials, reported in Figure S3. Similarly, in this case, F-MAX showed a greater absorption of light than the respective MAX, considering the region of the spectra close to the wavelength used in this work (660 nm).

■ CONCLUSIONS

In summary, we investigated the effect of the fluorination of different MAX, Ta_2AlC, Cr_2AlC, Ti_2AlC, and Ti_3AlC_2, on their structural and morphological properties and performances for application as photoelectrocatalysts for hydrogen generation. The morphology of the treated compounds changed as a consequence of the exposure to the fluorine gas, showing partial delamination between the layers and an extensive formation of oxyfluoride species on their surface. As an exception, the analysis of F-Cr_2AlC showed a considerable amount of fluorine on the surface without significant change in its morphology. This difference can be related to the fact that Cr_2AlC is reported to be more resistant to oxidation and exfoliation than the other MAX in this work. All MAX and F-MAX showed an improved photoelectrocatalytic activity when exposed to the illumination by a 660 nm light source. The more pronounced improvement of the catalytic activity due to illumination was observed for F-Ti_2AlC and F-Ti_3AlC_2, which showed a reduction of the overpotential values of 178 and 119 mV, respectively. The improved response of the two compounds when exposed to a 660 nm light can be attributed mainly to the presence of the photoactive oxyfluoride ($TiOF_2$) on their surface as a consequence of the fluorination process, as confirmed from the morphological and structural characterization. Cr_2AlC and F-Cr_2AlC presented the lowest overpotential and Tafel slope values in their respective category and, despite the absence of the corresponding oxyfluoride, the former showed better performances and improved photoelectrocatalytic effect compared to Cr_2AlC. In this case, a better insight into the properties of this compound is necessary to explain the role of fluorine within its structure. In particular, the photo-activity of MAX was an unexpected result, since they are reported to show a metallic behavior,[24] and further investigation on the origin of the stated photocatalytic activity could lead to intriguing discoveries. With this work, we reported for the first time the photoelectrocatalytic properties of MAX and F-MAX for energy conversion application. Even if the performances obtained are lower than some other materials, such as MoS_2 and MXene, we believe that a better understanding of these compounds and the effect of fluorination on their properties can lead to the development of new promising photoelectrocatalysts. For example, since MAX are mainly used to obtain MXenes and pure MXenes typically do not exhibit photo-activity, an exciting perspective

https://doi.org/10.1021/acssuschemeng.1c08133
ACS Sustainable Chem. Eng. 2022, 10, 2793−2801

could be put forth to evaluate the possibilities to synthesize MXenes that present photoelectrochemical activity from the exfoliation of F-MAX.

MATERIALS AND METHODS

Materials. MAX (Ta_2AlC, Cr_2AlC, Ti_2AlC, and Ti_3AlC_2) were purchased from Laizhou Kai Kai Ceramic Material Co. Ltd, and sulfuric acid (H_2SO_4) 96% was obtained from Penta, Czech Republic. All solutions were prepared in deionized water with a resistivity of 18 MΩ cm.

Fluorination of MAX Phases. The reaction was carried out in a four-chamber PTFE reactor located inside a sealed Monel autoclave. Ta_2AlC, Cr_2AlC, Ti_2AlC, and Ti_3AlC_2 were placed separately in the four chambers of the reactor, which was then secured using a permeable stopper. After several evacuation cycles and flushing with nitrogen gas (N_2), the autoclave was evacuated for 20 min to complete the de-aeration process. Afterward, 20% fluorine gas (F_2) in N_2 was slowly flushed inside the system and pressurized to 5 bar. The autoclave was then heated to 150 °C and maintained overnight, using a Wood's metal heating bath. Subsequently, when the system was cooled down to room temperature, the gases were removed from the autoclave and collected in a pressurized safety reservoir in which they were treated in a soda ash bath for neutralization. To remove any traces of fluorine gas or related volatile compounds, the autoclave was vented and flushed several times with N_2. A final evacuation was done using a column with sodium carbonate, and the system was filled back with N_2 to atmospheric pressure. Finally, the MAX were collected from the reactor and properly stored in sealed vials.

Materials Characterization. Morphological characterization was performed using high-resolution SEM (FEI Verios 460L). An EDS detector X-MaxN 150 (Oxford Instruments) was used to obtain the elemental mapping and analysis using an accelerating voltage of 30 kV. Additional chemical composition analysis was carried out using XPS (Kratos Analytical Axis Supra), and the spectra obtained were calibrated against the C 1s peak (285 eV) using the CasaXPS software. The structural analysis of the F-MAX was investigated using an X-ray diffractometer (PANalytical XPert-PRO) with a Co $K\alpha_1$ source of wavelength 0.1789 nm. UV−visible (UV−vis) absorbance spectra were acquired between 300 and 900 nm using a UV−vis spectrophotometer (JASCO V-750) with a scan speed of 400 nm min^{-1}. The samples for the UV−vis measurements were prepared suspending MAX and F-MAX (0.625 mg mL^{-1}) in a solution of 50% ethanol in water.

Photoelectrochemical Measurements. MAX and F-MAX (2.5 mg mL^{-1}) were dispersed in deionized water and ultrasonicated for 60 min. Afterward, 5 μL of the obtained suspension was drop-casted on the GC electrode and dried under a heat lamp. The prepared electrode was then used as a working electrode in a three-electrode configuration. Ag/AgCl (1 M KCl) was used as a reference electrode, and a platinum wire was used as a counter electrode. LSV was performed using a potentiostat (PGSTAT204, Metrohm Autolab, The Netherlands) controlled by NOVA software (version 2.1), using a scan rate of 2 mV s^{-1}, immersing the electrodes in a quartz cell containing 0.5 M H_2SO_4 solution. All reported potentials were converted to the RHE, according to the potential value reported in the literature for the reference Ag/AgCl (1 M KCl, 236 mV).[52] The illumination source used for the photoelectrochemical experiments was a customized LED (LZ4-40R208, LedEngin Inc.) setup that emits the wavelength 660 nm (≈40 mW cm^{-2}). All MAX and F-MAX were tested with and without illumination, and the bare GC electrode was measured as a reference. For chronoamperometry measurements, a fixed potential of −0.46 V vs RHE was applied and the light source was switched on/off at regular intervals.

ASSOCIATED CONTENT

Supporting Information

The Supporting Information is available free of charge at https://pubs.acs.org/doi/10.1021/acssuschemeng.1c08133.

EDS spectra of the F-MAX, UV−vis absorbance spectra, Tafel plots, and corresponding Tafel slope values (PDF)

AUTHOR INFORMATION

Corresponding Author

Martin Pumera − *Future Energy and Innovation Laboratory, Central European Institute of Technology, Brno University of Technology, Brno 61200, Czech Republic; Center for Advanced Functional Nanorobots, Department of Inorganic Chemistry, Faculty of Chemical Technology, University of Chemistry and Technology Prague, Prague 16628, Czech Republic; Department of Chemical and Biomolecular Engineering, Yonsei University, Seoul 03722, Korea; Department of Medical Research, China Medical University Hospital, China Medical University, Taichung 40402, Taiwan;* orcid.org/0000-0001-5846-2951; Email: pumera.research@gmail.com

Authors

Michela Sanna − *Future Energy and Innovation Laboratory, Central European Institute of Technology, Brno University of Technology, Brno 61200, Czech Republic*

Siowwoon Ng − *Future Energy and Innovation Laboratory, Central European Institute of Technology, Brno University of Technology, Brno 61200, Czech Republic;* orcid.org/0000-0003-2176-6710

Jayraj V. Vaghasiya − *Center for Advanced Functional Nanorobots, Department of Inorganic Chemistry, Faculty of Chemical Technology, University of Chemistry and Technology Prague, Prague 16628, Czech Republic;* orcid.org/0000-0003-0950-3299

Complete contact information is available at: https://pubs.acs.org/10.1021/acssuschemeng.1c08133

Author Contributions

M.S.: Photoelectrochemical and XPS measurements, data analysis, and writing the original draft. S.N.: SEM imaging, data analysis, and review and editing of the manuscript. J.V.V: XRD and EDS measurements and review of the manuscript. M.P.: funding acquisition, conceptualization, and review and editing of the manuscript.

Notes

The authors declare no competing financial interest.

ACKNOWLEDGMENTS

M.P. acknowledges the Grant Agency of the Czech Republic (GACR EXPRO: 19-26896X). M.S. acknowledges the Brno Ph.D. Talent scholarship funded by the Brno City Municipality, and the project Quality Internal Grants of BUT (KInG BUT), reg. no. CZ.02.2.69/0.0/0.0/19_073/0016948, which is financed from the OP RDE. Material characterizations were carried out with the support of CzechNanoLab project at CEITEC Nano Research Infrastructure (LM2018110, MEYS CR). The authors acknowledge Dr. Jan Plutnar for the synthesis of the fluorinated MAX phases.

REFERENCES

(1) Woodhouse, M.; Herman, G. S.; Parkinson, B. A. Combinatorial Approach to Identification of Catalysts for the Photoelectrolysis of Water. *Chem. Mater.* **2005**, *17*, 4318−4324.

(2) Chen, X.; Shen, S.; Guo, L.; Mao, S. S. Semiconductor-Based Photocatalytic Hydrogen Generation. *Chem. Rev.* **2010**, *110*, 6503−6570.

(3) Zou, X.; Sun, Z.; Hu, Y. H. G-C_3N_4-Based Photoelectrodes for Photoelectrochemical Water Splitting: A Review. *J. Mater. Chem. A* **2020**, *8*, 21474−21502.
(4) Fujishima, A.; Honda, K. Electrochemical Photolysis of Water at a Semiconductor Electrode. *Nature* **1972**, *238*, 37−38.
(5) Tahir, A. A.; Wijayantha, K. G. U.; Saremi-Yarahmadi, S.; Mazhar, M.; McKee, V. Nanostructured α-Fe2O3 Thin Films for Photoelectrochemical Hydrogen Generation. *Chem. Mater.* **2009**, *21*, 3763−3772.
(6) Jiao, Y.; Zheng, Y.; Davey, K.; Qiao, S.-Z. Activity Origin and Catalyst Design Principles for Electrocatalytic Hydrogen Evolution on Heteroatom-Doped Graphene. *Nat. Energy* **2016**, *1*, 16130.
(7) Qu, L.; Liu, Y.; Baek, J.-B.; Dai, L. Nitrogen-Doped Graphene as Efficient Metal-Free Electrocatalyst for Oxygen Reduction in Fuel Cells. *ACS Nano* **2010**, *4*, 1321−1326.
(8) Zhao, Y.; Zhang, J.; Qu, L. Graphitic Carbon Nitride/Graphene Hybrids as New Active Materials for Energy Conversion and Storage. *ChemNanoMat* **2015**, *1*, 298−318.
(9) Gong, Y.; Li, M.; Wang, Y. Carbon Nitride in Energy Conversion and Storage: Recent Advances and Future Prospects. *ChemSusChem* **2015**, *8*, 931−946.
(10) Jaramillo, T. F.; Jørgensen, K. P.; Bonde, J.; Nielsen, J. H.; Horch, S.; Chorkendorff, I. Identification of Active Edge Sites for Electrochemical H_2 Evolution from MoS_2 Nanocatalysts. *Science* **2007**, *317*, 100−102.
(11) Gusmão, R.; Sofer, Z.; Pumera, M. Metal Phosphorous Trichalcogenides ($MPCh_3$): From Synthesis to Contemporary Energy Challenges. *Angew. Chem., Int. Ed.* **2019**, *58*, 9326−9337.
(12) Sanna, M.; Ng, S.; Pumera, M. Layered Transition Metal Selenophosphites for Visible Light Photoelectrochemical Production of Hydrogen. *Electrochem. Commun.* **2021**, *129*, 107077.
(13) Yang, F.; Elnabawy, A. O.; Schimmenti, R.; Song, P.; Wang, J.; Peng, Z.; Yao, S.; Deng, R.; Song, S.; Lin, Y.; Mavrikakis, M.; Xu, W. Bismuthene for Highly Efficient Carbon Dioxide Electroreduction Reaction. *Nat. Commun.* **2020**, *11*, 1088.
(14) Dinh, K. N.; Zhang, Y.; Zhu, J.; Sun, W. Phosphorene-Based Electrocatalysts. *Chem.—A Eur. J.* **2020**, *26*, 6437−6446.
(15) Ng, S.; Sturala, J.; Vyskocil, J.; Lazar, P.; Martincova, J.; Plutnar, J.; Pumera, M. Two-Dimensional Functionalized Germananes as Photoelectrocatalysts. *ACS Nano* **2021**, *15*, 11681.
(16) Redondo, E.; Pumera, M. MXene-Functionalised 3D-Printed Electrodes for Electrochemical Capacitors. *Electrochem. Commun.* **2021**, *124*, 106920.
(17) Sun, S.; Liao, C.; Hafez, A. M.; Zhu, H.; Wu, S. Two-Dimensional MXenes for Energy Storage. *Chem. Eng. J.* **2018**, *338*, 27−45.
(18) Jun, B.-M.; Kim, S.; Heo, J.; Park, C. M.; Her, N.; Jang, M.; Huang, Y.; Han, J.; Yoon, Y. Review of MXenes as New Nanomaterials for Energy Storage/Delivery and Selected Environmental Applications. *Nano Res.* **2019**, *12*, 471−487.
(19) Anasori, B.; Lukatskaya, M. R.; Gogotsi, Y. 2D Metal Carbides and Nitrides (MXenes) for Energy Storage. *Nat. Rev. Mater.* **2017**, *2*, 16098.
(20) Sun, Y.; Chen, D.; Liang, Z. Two-Dimensional MXenes for Energy Storage and Conversion Applications. *Mater. Today Energy* **2017**, *5*, 22−36.
(21) Rohaizad, N.; Mayorga-Martinez, C. C.; Fojtů, M.; Latiff, N. M.; Pumera, M. Two-Dimensional Materials in Biomedical, Biosensing and Sensing Applications. *Chem. Soc. Rev.* **2021**, *50*, 619−657.
(22) Chia, X.; Pumera, M. Characteristics and Performance of Two-Dimensional Materials for Electrocatalysis. *Nat. Catal.* **2018**, *1*, 909−921.
(23) Sokol, M.; Natu, V.; Kota, S.; Barsoum, M. W. On the Chemical Diversity of the MAX Phases. *Trends Chem.* **2019**, *1*, 210−223.
(24) Radovic, M.; Barsoum, M. W. MAX Phases: Bridging the Gap between Metals and Ceramics. *Am. Ceram. Soc. Bull.* **2013**, *92*, 20−27.
(25) Barsoum, M. W.; Radovic, M. Elastic and Mechanical Properties of the MAX Phases. *Annu. Rev. Mater. Res.* **2011**, *41*, 195−227.
(26) Khazaei, M.; Ranjbar, A.; Esfarjani, K.; Bogdanovski, D.; Dronskowski, R.; Yunoki, S. Insights into Exfoliation Possibility of MAX Phases to MXenes. *Phys. Chem. Chem. Phys.* **2018**, *20*, 8579−8592.
(27) Naguib, M.; Mashtalir, O.; Carle, J.; Presser, V.; Lu, J.; Hultman, L.; Gogotsi, Y.; Barsoum, M. W. Two-Dimensional Transition Metal Carbides. *ACS Nano* **2012**, *6*, 1322−1331.
(28) Vaghasiya, J. V.; Mayorga-Martinez, C. C.; Sofer, Z.; Pumera, M. MXene-Based Flexible Supercapacitors: Influence of an Organic Ionic Conductor Electrolyte on the Performance. *ACS Appl. Mater. Interfaces* **2020**, *12*, 53039−53048.
(29) Chia, H. L.; Mayorga-Martinez, C. C.; Antonatos, N.; Sofer, Z.; Gonzalez-Julian, J. J.; Webster, R. D.; Pumera, M. MXene Titanium Carbide-Based Biosensor: Strong Dependence of Exfoliation Method on Performance. *Anal. Chem.* **2020**, *92*, 2452−2459.
(30) Vaghasiya, J. V.; Mayorga-Martinez, C. C.; Vyskočil, J.; Sofer, Z.; Pumera, M. Integrated Biomonitoring Sensing with Wearable Asymmetric Supercapacitors Based on Ti_3C_2 MXene and 1T-Phase WS_2 Nanosheets. *Adv. Funct. Mater.* **2020**, *30*, 2003673.
(31) Vyskočil, J.; Mayorga-Martinez, C. C.; Szőkölová, K.; Dash, A.; Gonzalez-Julian, J.; Sofer, Z.; Pumera, M. 2D Stacks of MXene Ti_3C_2 and 1T-Phase WS_2 with Enhanced Capacitive Behavior. *ChemElectroChem* **2019**, *6*, 3982−3986.
(32) Akshay Kumar, K. P.; Alduhaish, O.; Pumera, M. Electrocatalytic Activity of Layered MAX Phases for the Hydrogen Evolution Reaction. *Electrochem. Commun.* **2021**, *125*, 106977.
(33) Rosli, N. F.; Nasir, M. Z. M.; Antonatos, N.; Sofer, Z.; Dash, A.; Gonzalez-Julian, J.; Fisher, A. C.; Webster, R. D.; Pumera, M. MAX and MAB Phases: Two-Dimensional Layered Carbide and Boride Nanomaterials for Electrochemical Applications. *ACS Appl. Nano Mater.* **2019**, *2*, 6010−6021.
(34) Eklund, P.; Rosen, J.; Persson, P. O. Å. Layered Ternary $M_{N+1}AX_n$ Phases and Their 2D Derivative MXene: An Overview from a Thin-Film Perspective. *J. Phys. D. Appl. Phys.* **2017**, *50*, 113001.
(35) Sun, Z. M. Progress in Research and Development on MAX Phases: A Family of Layered Ternary Compounds. *Int. Mater. Rev.* **2011**, *56*, 143−166.
(36) Chia, H. L.; Mayorga-Martinez, C. C.; Pumera, M. Doping and Decorating 2D Materials for Biosensing: Benefits and Drawbacks. *Adv. Funct. Mater.* **2021**, *31*, 2102555.
(37) Wang, X.; Wang, W.; Xu, D.; Liu, Y.; Lai, W.; Liu, X. Activation Effect of Porous Structure on Fluorination of Graphene Based Materials with Large Specific Surface Area at Mild Condition. *Carbon* **2017**, *124*, 288−295.
(38) Kim, Y. H.; Park, J. S.; Choi, Y.-R.; Park, S. Y.; Lee, S. Y.; Sohn, W.; Shim, Y.-S.; Lee, J.-H.; Park, C. R.; Choi, Y. S.; Hong, B. H.; Lee, J. H.; Lee, W. H.; Lee, D.; Jang, H. W. Chemically Fluorinated Graphene Oxide for Room Temperature Ammonia Detection at Ppb Levels. *J. Mater. Chem. A* **2017**, *5*, 19116−19125.
(39) Hsieh, Y.-L.; Su, W.-H.; Huang, C.-C.; Su, C.-Y. In Situ Cleaning and Fluorination of Black Phosphorus for Enhanced Performance of Transistors with High Stability. *ACS Appl. Mater. Interfaces* **2020**, *12*, 37375−37383.
(40) Ma, F.; Sun, C.; Shao, Y.; Wu, Y.; Huang, B.; Hao, X. One-Step Exfoliation and Fluorination of g-C_3N_4 Nanosheets with Enhanced Photocatalytic Activities. *New J. Chem.* **2017**, *41*, 3061−3067.
(41) Drissi, L. B.; Kanga, N. B.-J.; Ramadan, F. Z. Excitonic and Fluorination Effects on Optoelectronic Response of GeC Hybrid. *Comput. Condens. Matter* **2018**, *14*, 49−54.
(42) Chen, K.; Qiu, N.; Deng, Q.; Kang, M.-H.; Yang, H.; Baek, J.-U.; Koh, Y.-H.; Du, S.; Huang, Q.; Kim, H.-E. Cytocompatibility of Ti_3AlC_2, Ti_3SiC_2, and Ti_2AlN: In Vitro Tests and First-Principles Calculations. *ACS Biomater. Sci. Eng.* **2017**, *3*, 2293−2301.
(43) Myhra, S.; Crossley, J. A. A.; Barsoum, M. W. Crystal-Chemistry of the Ti_3AlC_2 and Ti_4AlN_3 Layered Carbide/Nitride

https://doi.org/10.1021/acssuschemeng.1c08133
ACS Sustainable Chem. Eng. 2022, 10, 2793−2801

Phases - Characterization by XPS. *J. Phys. Chem. Solids* **2001**, *62*, 811−817.
(44) Zhu, J.; Zhang, D.; Bian, Z.; Li, G.; Huo, Y.; Lu, Y.; Li, H. Aerosol-Spraying Synthesis of SiO_2/TiO_2 Nanocomposites and Conversion to Porous TiO_2 and Single-Crystalline $TiOF_2$. *Chem. Commun.* **2009**, *36*, 5394−5396.
(45) Lange, M. A.; Khan, I.; Opitz, P.; Hartmann, J.; Ashraf, M.; Qurashi, A.; Prädel, L.; Panthöfer, M.; Cossmer, A.; Pfeifer, J.; Simon, F.; von der Au, M.; Meermann, B.; Mondeshki, M.; Tahir, M. N.; Tremel, W. A Generalized Method for High-Speed Fluorination of Metal Oxides by Spark Plasma Sintering Yields Ta_3O_7F and TaO_2F with High Photocatalytic Activity for Oxygen Evolution from Water. *Adv. Mater.* **2021**, *33*, 2007434.
(46) Ouisse, T.; Sarigiannidou, E.; Chaix-Pluchery, O.; Roussel, H.; Doisneau, B.; Chaussende, D. High Temperature Solution Growth and Characterization of Cr_2AlC Single Crystals. *J. Cryst. Growth* **2013**, *384*, 88−95.
(47) Lin, Z. J.; Li, M. S.; Wang, J. Y.; Zhou, Y. C. High-Temperature Oxidation and Hot Corrosion of Cr_2AlC. *Acta Mater.* **2007**, *55*, 6182−6191.
(48) Khaledialidusti, R.; Khazaei, M.; Khazaei, S.; Ohno, K. High-Throughput Computational Discovery of Ternary-Layered MAX Phases and Prediction of Their Exfoliation for Formation of 2D MXenes. *Nanoscale* **2021**, *13*, 7294−7307.
(49) Wang, L.; Sofer, Z.; Pumera, M. Voltammetry of Layered Black Phosphorus: Electrochemistry of Multilayer Phosphorene. *ChemElectroChem* **2015**, *2*, 324−327.
(50) Wang, J.; Cao, F.; Bian, Z.; Leung, M. K. H.; Li, H. Ultrafine Single-Crystal $TiOF_2$ Nanocubes with Mesoporous Structure, High Activity and Durability in Visible Light Driven Photocatalysis. *Nanoscale* **2014**, *6*, 897−902.
(51) Hou, C.; Xie, J.; Yang, H.; Chen, S.; Liu, H. Preparation of $Cu_2O@TiOF_2/TiO_2$ and Its Photocatalytic Degradation of Tetracycline Hydrochloride Wastewater. *RSC Adv.* **2019**, *9*, 37911−37918.
(52) Kahlert, H. *Reference Electrodes BT - Electroanalytical Methods: Guide to Experiments and Applications*; Scholz, F., Bond, A. M., Compton, R. G., Fiedler, D. A., Inzelt, G., Kahlert, H., Komorsky-Lovrić, Š., Lohse, H., Lovrić, M., Marken, F., Neudeck, A., Retter, U., Scholz, F., Stojek, Z., Eds.; Springer: Berlin, Heidelberg, 2010; pp 291−308.

https://doi.org/10.1021/acssuschemeng.1c08133
ACS Sustainable Chem. Eng. 2022, 10, 2793−2801

7. The unexpected photoelectrochemical activity of MAX phases: the role of oxide impurities

Published paper included in this chapter:

Sanna, M.; Novčić, K.A.; Ng, S.; Černý, M.; Pumera, M., The unexpected photoelectrochemical activity of MAX phases: the role of oxide impurities, *J. Mater. Chem. A*, **2023**,11, 3080-3090.

7.1. Motivation for the study

Building upon the findings from our preceding research, we embarked on a comprehensive exploration into the intricacies of MAX properties and the underlying mechanisms governing their inherent photoactivity. By synergizing theoretical insights with empirical data, we aimed to gain deeper insights into the influence of impurities within these ternary compounds. It is intriguing to note that MAX exhibit enhanced catalytic prowess in response to light stimuli, a phenomenon that contradicts their anticipated metallic behavior based on electronic structure considerations. Unraveling the origins of this discrepancy presents an opportunity to fine-tune and optimize the properties of MAX, thereby augmenting their efficacy for applications in photoelectrochemical processes. Through this endeavor, we endeavor to unlock the full potential of MAX materials, paving the way for advancements in sustainable energy technologies.

7.2. Paper conclusion

In summary, our investigation focused on analyzing the properties of three MAX, namely Nb_2AlC, Ta_2AlC, and Ti_3AlC_2, utilizing both theoretical and experimental methodologies to elucidate the origins of their photoactivity. Theoretical calculations revealed that metals

predominantly contribute to the density of states (DOS) around the Fermi level, confirming the metallic nature of these compounds, with no discernible band gap in the vicinity of the Fermi level. XPS and EDS analyses confirmed the presence of transition metal oxides and revealed a notable amount of Al_2O_3. Interestingly, experimental estimations indicated the presence of two fundamental absorptions at 2.2 eV and 3.1 eV for Nb_2AlC and 2.2 eV and 3.3 eV for Ta_2AlC, contrasting with theoretical predictions. The estimated band gap for Ti_3AlC_2 was also determined to be 2.4 eV. Demonstrating the presence of photoactive material, all MAX phases exhibited enhanced photocatalytic activity towards HER under illumination by various light sources. Notably, Nb_2AlC and Ta_2AlC demonstrated superior performance under UV light, while Ti_3AlC_2 exhibited the lowest overpotential under 460 nm light, aligning with the estimated optical band gaps. The documented formation of oxides on MAX, resulting from inevitable contamination upon exposure to air or oxidizing solvents, was found to play a pivotal role in enhancing photoelectrochemical hydrogen generation due to their intrinsic photoactivity. These insights may pave the way for further utilization of MAX phases as photoelectrocatalysts. Beyond the three MAX phases investigated in this study, the extensive pool of over 150 other synthesized MAX phases may harbor similar photoactive properties yet to be explored and harnessed in this domain.

7.3. Author contribution

In this work, I conducted all the studies related to the experimental evaluation of MAX, analysed the data obtained and plotted them. In particular, I performed the optical measurements, the morphological characterisation using SEM, and studied the elemental composition by EDS and XPS. I carried out the photoelectrochemical measurements and I wrote the first draft of the manuscript.

Journal of Materials Chemistry A

ROYAL SOCIETY OF CHEMISTRY

PAPER

View Article Online
View Journal | View Issue

Cite this: J. Mater. Chem. A, 2023, 11, 3080

The unexpected photoelectrochemical activity of MAX phases: the role of oxide impurities†

Michela Sanna, [a] Katarina A. Novčić, [a] Siowwoon Ng, [a] Miroslav Černý [bc] and Martin Pumera *[ade]

MAX phases are layered ternary compounds that are mainly studied for their physical properties and their use in the synthesis of MXenes. Their application in energy generation has been investigated and recently, the unexpected photoactivity of MAX phases under the influence of a visible light source has been reported. To investigate the origin of this photoactivity, theoretical calculations and experimental characterisation of the structural and optical properties of three MAX phases, Nb_2AlC, Ta_2AlC and Ti_3AlC_2, were performed. Although the theoretical calculations confirmed that the phases presented no band gap in the vicinity of the Fermi level, the experimental evaluation showed two main absorptions for Nb_2AlC and Ta_2AlC (2.2 eV, 3.1 eV, and 2.2 eV, 3.3 eV, respectively) and one for Ti_3AlC_2 (2.4 eV). To confirm the observations from the optical characterisation, the phases were applied as photoelectrocatalysts for hydrogen generation under the influence of light of different wavelengths. Nb_2AlC and Ta_2AlC performed better when exposed to UV light, while Ti_3AlC_2 showed the lowest overpotential under the influence of visible light, in accordance with the experimentally estimated band gaps. The materials were extensively characterised and the photoactivity of MAX phases was attributed to the presence of photoactive oxide impurities on the surface of the material, which are naturally formed from contact with air and solvents. In this work, we show how these impurities can lead to better performances thanks to their intrinsic photoactivity, indicating the prospects for the use of MAX phases in other photoelectrochemical processes.

Received 1st September 2022
Accepted 6th January 2023

DOI: 10.1039/d2ta06929f

rsc.li/materials-a

Introduction

The dramatic increase in energy demand in the past decades and the consequent overexploitation of fossil fuels have contributed to the great need to find alternative energy sources. Among the environmentally friendly energy sources, one of the most interesting alternatives to fossil fuels to alleviate environmental and energy issues is solar energy, combined with electrochemical reactions to store energy in chemical bonds.[1,2] In 2007, it was estimated that in the so-called "solar belt", which referred to the abundant solar radiation region of the Earth between latitudes of 40°N and 40°S, the yearly average input of solar energy is 18.48 MJ (m^2 day^{-1}).[3] This is a remarkable amount of free energy that can be harvested and implemented in future energy production technology to achieve long-term sustainable and renewable energy sources. For this reason, the scientific community has long focused on the solar production of clean hydrogen fuels with high energy density through photoelectrochemical reactions.[4–6] Various (photo) electrocatalytic materials from TiO_2,[7,8] $BiVO_4$,[9,10] CdS,[11,12] and MoS_2,[13,14] to more recent work on Xenes[15,16] and MXenes,[17,18] have been investigated for hydrogen production, and new catalysts are continuously being studied and tested for application in this field.

MAX phases (MAX) are a class of layered ternary compounds with the general formula $M_{n+1}AX_n$ (M = early transition metal, A = IIIA and IVA group element, X = C or N, and n = 1, 2, or 3), which possess hexagonal crystal structures with $P6_3/mmc$ symmetry.[19–22] MAX are known for possessing properties typical of metals and ceramics, such as thermal and electrical conductivity, chemical and oxidation resistance, and damage tolerance.[19,22,23] Lately, MAX have been the centre of attention because they are the parent materials in the creation of two-dimensional (2D) MXenes. The A layer of MAX can be selectively etched to form MXenes.[24–26] These 2D materials have attracted attention for electrochemical applications since they

[a]Future Energy and Innovation Laboratory, Central European Institute of Technology, Brno University of Technology, Purkyňova 123, 61200 Brno, Czech Republic. E-mail: pumera.research@gmail.com

[b]Central European Institute of Technology, Brno University of Technology, Technická 2, CZ-616 69 Brno, Czech Republic

[c]Faculty of Mechanical Engineering, Brno University of Technology, Technická 2, CZ-616 69 Brno, Czech Republic

[d]Faculty of Electrical Engineering and Computer Science, VSB–Technical University of Ostrava, 17. Listopadu 2172/15, 70800 Ostrava, Czech Republic

[e]Department of Medical Research, China Medical University Hospital, China Medical University, No. 91 Hsueh-Shih Road, Taichung 40402, Taiwan

† Electronic supplementary information (ESI) available. See DOI: https://doi.org/10.1039/d2ta06929f

are characterised by high metallic conductivity, high negative zeta potential, and fast charge transfer kinetics.[27–30] The interest of the scientific community is concentrated on the application of MXenes in different fields, although MAX and their properties have not been fully investigated. Recent studies have taken one step back, looking into the fundamental electrochemical properties of MAX phases and the possible application of these compounds as (photo)electrocatalysts for energy conversion.[22,31,32]

In previous studies,[33,34] MAX showed better catalytic performances when exposed to different light sources. Ta_2AlC, Cr_2AlC, Ti_2AlC and Ti_3AlC_2 demonstrated improved photoelectrocatalytic H_2 production when illuminated by a 660 nm light source.[33] In addition, Cr_2AlC demonstrated huge potential in the photodegradation of various cationic and anionic dyes under the influence of visible and UV light, showing an optical band gap of 1.28 eV.[34] These studies provided evidence that in contrast to the metallic nature of MAX,[35,36] some of them, if not all, possess band gaps and absorb light, as shown in Scheme 1, so they can be applied in solar-driven applications.

Here, we aim to understand the origin of the photoactivity of these compounds. We report a theoretical and experimental study on three MAX, namely Nb_2AlC, Ta_2AlC, and Ti_3AlC_2. A theoretical study on the total and partial density of states and band structure was carried out based on Density Functional Theory (DFT). The morphology, surface composition, and optical properties of MAX were analysed in detail by SEM, EDS and XPS. Finally, the phases were applied as a photoelectrocatalyst for hydrogen generation under the influence of different sources of light. Trace amounts of impurities (in ppm or even in ppb levels) have been reported to influence traditional synthetic chemistry catalysis,[37–40] electrocatalysis[41–47] and photocatalysis.[48,49] This is true about metals,[37] metal oxides[45] and phase impurities[50] because in catalysis (chemical, electrochemical or photochemical) the small active sites can overwhelmingly dominate the much more sluggish performance of the "host" material.[41,42,51] We show that oxide impurities within the MAX are the driving force of the photoelectrochemistry, like impurities are the driving force of the electrochemistry in research on carbon nanotubes,[41,42] graphene[43,44] and transition metal dichalcogenides.[45–47]

Experimental

Materials

MAX phases (Nb_2AlC, Ta_2AlC, and Ti_3AlC_2) were obtained from Laizhou Kai Kai Ceramic Material Co. Ltd. and were used without additional treatment. Screen-printed carbon electrodes (SPCE, SE 101) were purchased from CH instruments, and sulfuric acid (H_2SO_4, 96%) from Penta, Czech Republic. All solutions were prepared using deionised water with a resistivity of 18 MΩ cm.

Theoretical calculations

The first principles DFT calculations were performed using the Vienna *Ab initio* Simulation Package (VASP) and the generalised gradient approximation (GGA) in parametrisation by Perdew, Burke and Ernzerhof (PBE). The cut-off energy of 500 eV and a Monkhorst–Pack Γ-centered 19 × 19 × 4 k-point mesh were used. For the study of MAX, a 2 × 2 × 1 supercell was created. VESTA code[52] and Origin-Pro 2020 were used for the structure visualisation. Analysis of the electronic properties was

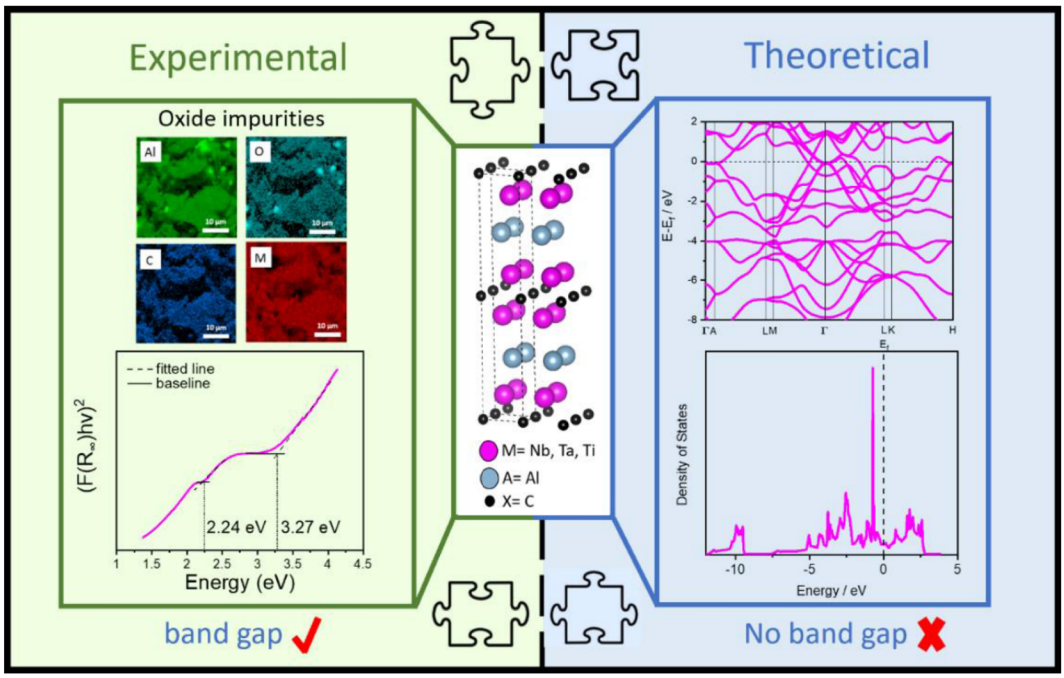

Scheme 1 Schematic representation of the motivation and the approach used in this work for the investigation of the photoactivity of MAX phases.

performed through calculations of the band structure and total and partial density of states (DOS).

Materials characterisations

The morphology of the MAX phase powders was analysed using a scanning electron microscope (SEM, Mira 3 XMU Tescan) equipped with an energy-dispersive X-ray spectroscopy (EDS) detector X-MAX20 (Oxford Instruments) for elemental mapping. An accelerating voltage of 20 kV was used for the analysis of the elemental composition. Further information about the chemical composition was obtained using X-ray photoelectron spectroscopy (XPS, Kratos Analytical Axis Supra). All the obtained spectra were analysed using the CasaXPS software and calibrated against the C 1s peak at 285 eV. The high-resolution spectra of the major elements were fitted using a Shirley-type background. The X-ray diffraction (XRD) patterns were obtained using an X-ray diffractometer (Rigaku SmartLab 3 kW) with Cu Kα source of wavelength 0.1789 nm. The optical images of the prepared electrodes were acquired by Stereomicroscope Zeiss Stemi 508 (STEMI) and the thickness determination was done by confocal laser scanning microscopy (CLSM, Olympus LEXT-OLS 4100) with 10× lenses. The reflectance spectra of MAX phases were measured by mounting an integrating sphere in a UV-vis spectrophotometer (JASCO V-750) operated by JASCO software. The measurements were performed within the range of 300–900 nm, using a scan speed of 400 nm min^{-1}. The Kubelka–Munk (K–M) function was employed to estimate the band gap of MAX phases. In particular, the reflectance measurements can be converted into the corresponding absorption spectra, applying the K–M function $F(R_\infty)$,[53] as defined in eqn (1):

$$F(R_\infty) = \frac{K}{S} = \frac{1 - R_\infty}{2R_\infty} \quad \text{where} \quad R_\infty = \frac{R_{sample}}{R_{standard}} \tag{1}$$

$F(R_\infty)$ can substitute for the absorption coefficient α defined in the Tauc method[54] by eqn (2):

$$(\alpha h\nu)^{\frac{1}{n}} = B(h\upsilon - E_g) \tag{2}$$

where h = Planck constant, υ = frequency, E_g = band gap energy, B = constant. The factor n depends on the nature of the transition, and it is equal to 2 for indirect transition band gaps and equal to $\frac{1}{2}$ for direct transition band gaps. Eqn (2) can be finally written in the form of eqn (3) and (4):

$$(F(R_\infty) \times h\nu)^2 = B(h\upsilon - E_g) \text{ for direct transition band gap} \tag{3}$$

$$(F(R_\infty) * h\nu)^{\frac{1}{2}} = B(h\upsilon - E_g) \text{ for indirect transition gap} \tag{4}$$

Tauc plots were obtained by plotting $(F(R_\infty)\ h\nu)^2$ *versus* photon energy and the baseline approach was used for the graphic extrapolation of the values.[55] In this approach, the linear fit is applied to the fundamental peak, similar to the Tauc method, and to the slope below the fundamental peak, which can be identified as the "baseline". The estimation of the band gap energy is given by the intersection of the two fitting lines. The absorbance spectra were converted from the reflectance measurement using the spectral analysis tool of the JASCO software.

Electrode preparation

Aqueous solutions of MAX phases (5 mg mL^{-1}) were sonicated for 30 minutes, and 5 μL of the obtained suspensions were drop-casted on SPCE and dried using a heat lamp. The same procedure was used to prepare the glassy carbon (GC) electrodes used for the chronoamperometry measurements. The loading of material on the electrodes was 0.35 mg cm^{-2}. The distribution of the particles on the SPCE was studied using the back-scattered electron detector mounted on the SEM, while the height of the deposition was analysed using CLSM. The obtained data, reported in Fig. S1,† showed that the size of the MAX particles varied in the range from 2 to 15 μm with a typical distribution of materials by the drop-casting technique.[56] Moreover, CLSM analysis showed that the thickness of the deposited MAX varied by up to 36.9 μm for Nb_2AlC, 19.2 μm for Ta_2AlC, and 38.6 μm for Ti_3AlC_2.

Photoelectrochemical measurements

All the measurements were carried out in a three-electrode configuration, using the prepared MAX on SPCE as the working electrode, a graphite rod as the counter electrode, and Ag/AgCl (1 M KCl) as the reference electrode. The electrodes were immersed in a quartz cell containing 0.5 M H_2SO_4 solution, and a potentiostat (PGSTAT204, Metrohm Autolab, The Netherlands) operated by NOVA software (version 2.1) was used to perform linear sweep voltammetry with a scan rate of 5 mV s^{-1}. The measured potentials were converted to the Reversible Hydrogen Electrode (RHE). A customised LED setup (LZ4-44UV00, LZ4-40B208, and LZ4-40R208, LedEngin Inc.) with interchangeable wavelengths (365 nm, 460 nm, and 660 nm) was used as the illumination source. The LSV of the bare SPCE was measured in the dark as a reference, while MAX phases were tested with and without illumination. For chronoamperometry measurements, GC electrodes were used as the working electrode and a fixed potential of −0.56 V *vs.* RHE was applied. The light source (660 nm) was switched on/off at regular intervals.

Results & discussion

We first performed a theoretical investigation of the properties of three MAX, specifically Nb_2AlC, Ta_2AlC, and Ti_3AlC_2 (Scheme 2), using the first principle calculations based on DFT. The plots of the total density of states (DOS) of Nb_2AlC, Ta_2AlC and Ti_3AlC_2 are presented in Fig. 1A–C. The DOS calculations show the metallic nature of all investigated MAX with no band gap. The continuous DOS across the Fermi level (E_f) indicates that the material is electrically conductive. Subsequently, partial DOS of Nb_2AlC, Ta_2AlC and Ti_3AlC_2 was used to study the nature of the chemical bonding. Fig. S2† shows the element and orbital resolved DOS of the MAX. From this Figure, the Fermi level is dominantly occupied by the transition metals of Nb, Ta and Ti,

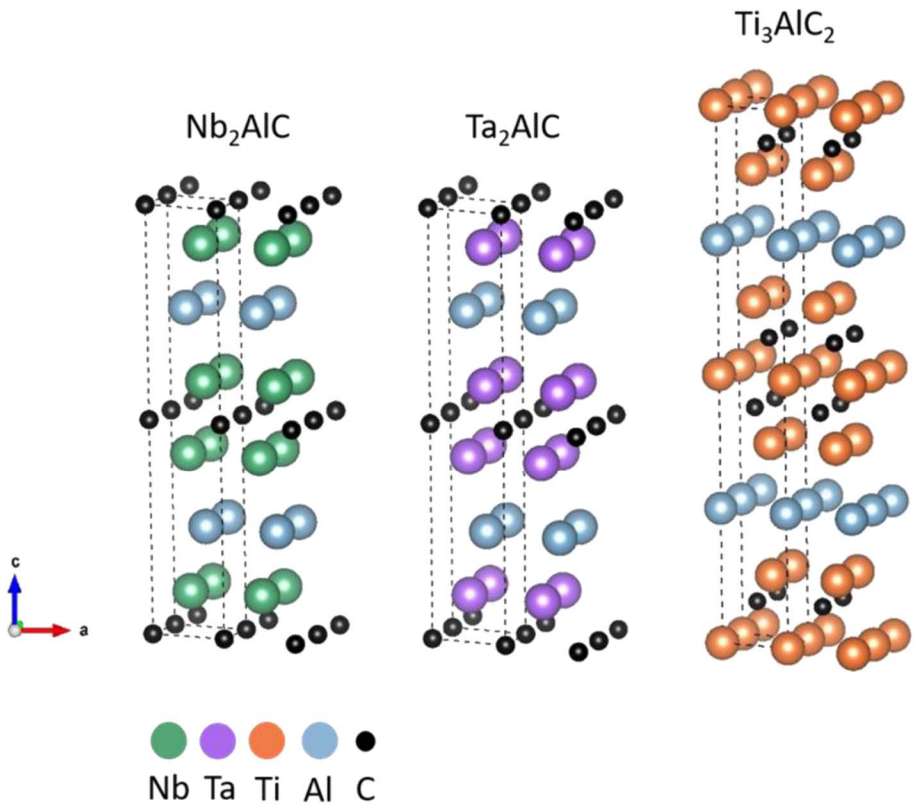

Scheme 2 Schematic illustration of the structure of MAX phases. The dashed lines show the edges of the unit cell.

respectively, which is also visible in the total DOS (Fig. 1A–C) that follows the pattern of the Nb (d), Ta (d) and Ti (d) orbitals. There is hybridisation between the transition metals Nb (d), Ta (d) and Ti (d) and C (p) at around −5 eV, −3 eV and −10 eV, respectively. The transition metals also showed hybridisation with the Al (p) at around −2 eV, −5 eV and −2.5 eV, respectively.

The *ab initio* electronic structure calculations of the investigated MAX predicted the band structure with numerous bands crossing the Fermi level, as shown in Fig. 1a–c. There is no gap in the vicinity of the Fermi level, which additionally confirmed the metallic nature of the MAX. The DOS and band structure results agree with previous works on theoretical studies of Nb_2AlC,[57,58] Ta_2AlC[36] and Ti_3AlC_2.[35,59]

Having a basic understanding of the MAX, we proceeded with extensive experimental material characterisations. SEM was used to study the morphology of the three phases and the obtained micrographs are shown in Fig. 2A–C. All the MAX presented the tight layered structure typical of these non-exfoliated materials and no additional structures were seen.

A detailed study of the surface elemental composition by employing EDS confirmed the presence of the composing elements of the MAX (transition metal, aluminium, and carbon), but also detected a considerable amount of oxygen. In particular, the elemental mapping reported in Fig. 3A–C shows that oxygen is uniformly distributed on the MAX, indicating the possible presence of metal oxides. Comparing the mapping of oxygen with the other elements, we observed the correspondence of the high-intensity spots between aluminium and oxygen, suggesting the presence of aluminium oxide. The elemental quantification from the EDS spectra (Fig. S3†) shows that Ta_2AlC is the MAX with the largest amount of oxygen (22.9 At%), followed by Nb_2AlC (10.8 At%), and Ti_3AlC_2 (4.8 At%). For all of them, the sum of the elements deviated from the expected stoichiometry, supporting the presence of other elements or different metal oxides.

XPS was utilised to study in more detail the surface chemical compositions of the three MAX (Fig. 4A–C). The survey spectra of the phases confirmed the observation by EDS, showing the presence of the corresponding transition metals, aluminium, carbon, and oxygen. No additional elements were detected. Only the main peaks for each element were labelled in the survey spectra in Fig. 4. The high-resolution spectra of all the main peaks were recorded to further analyse the oxidation state of the transition metals and the chemical bonding with carbon and oxygen. The deconvolution of the transition metal region confirmed the presence of metal-carbide and metal–oxygen bonds. In particular, the Nb 3d region revealed the doublet peaks for the metallic state Nb^0 (202.9 eV, 205.6 eV),[60] the doublet relative to the bond with carbon (203.7 eV, 206.4 eV),[61] and the one for the oxidation state Nb^{5+} (207.3 eV, 210.0 eV),[62] denoting the presence of Nb_2O_5. The deconvolution of the Ta 4f region showed the Ta–C doublets (22.4 eV, 24.2 eV),[63] and the peaks related to the oxidation state Ta^{5+} (26.1 eV, 28.0 eV),[64] which can be attributed to Ta_2O_5. The high-resolution spectrum of the Ti 2p region of Ti_3AlC_2 revealed the Ti–C doublets (455.0 eV, 461.2 eV),[65] the peaks related to the metallic state Ti^0

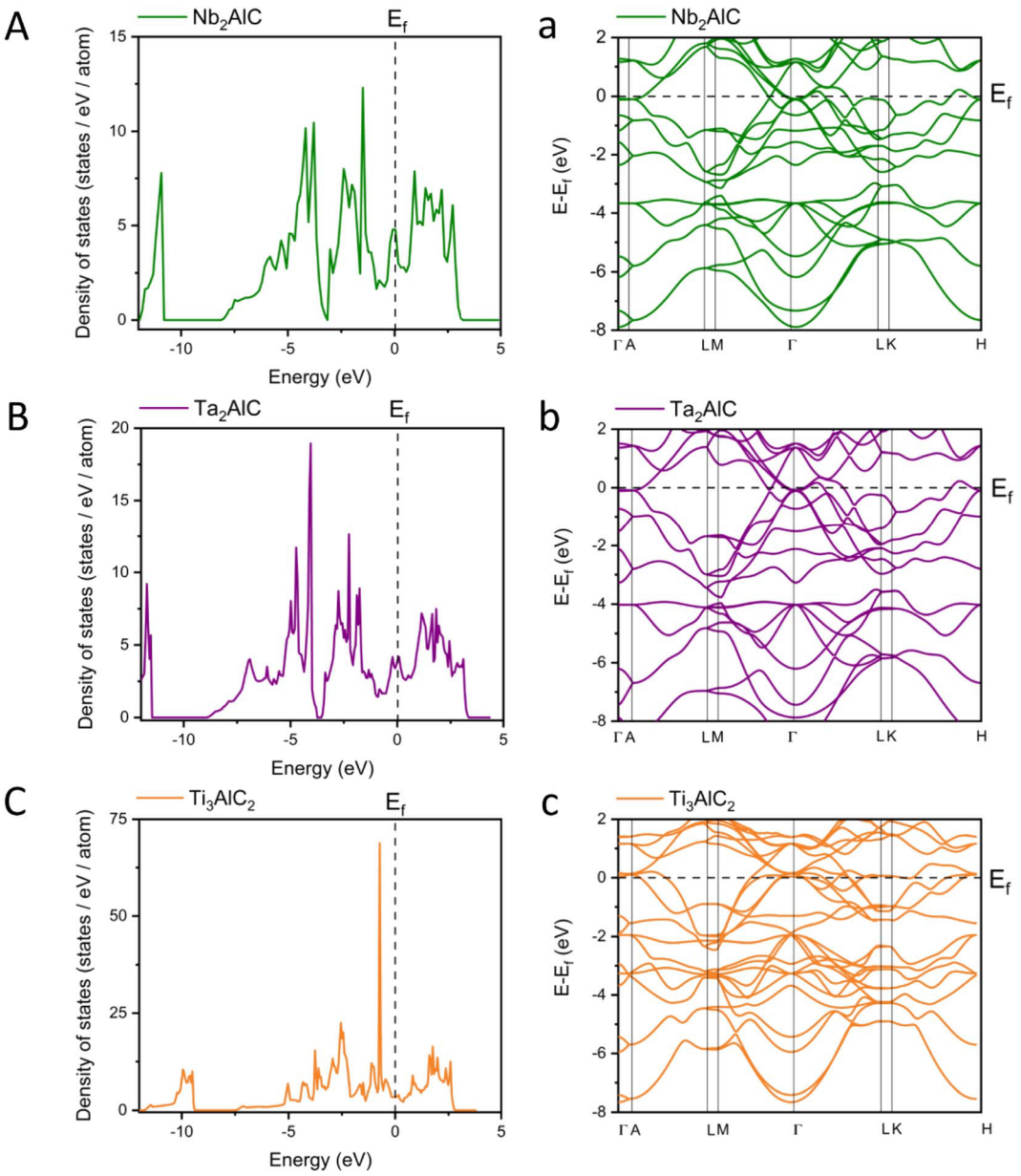

Fig. 1 Total density of states (DOS) and band structure of Nb_2AlC (A, a), Ta_2AlC (B, b) and Ti_3AlC_2 (C, c). The Fermi level, E_f is shown by the black dashed line.

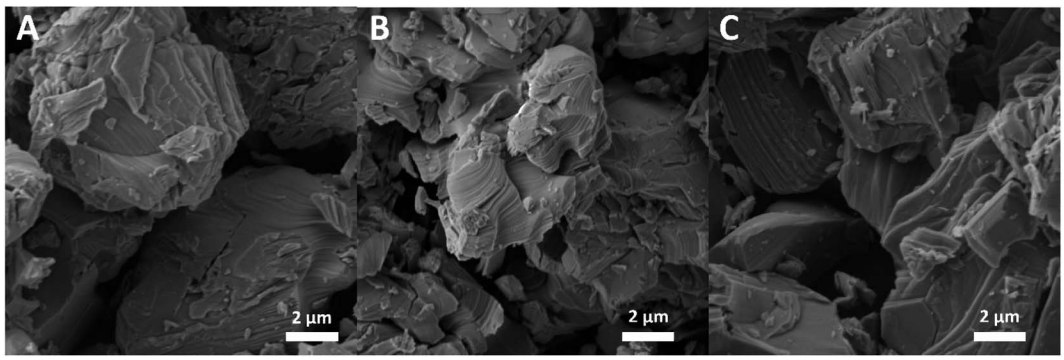

Fig. 2 SEM micrographs of MAX phases, Nb_2AlC (A), Ta_2AlC (B), and Ti_3AlC_2 (C). The scale bars are 2 μm.

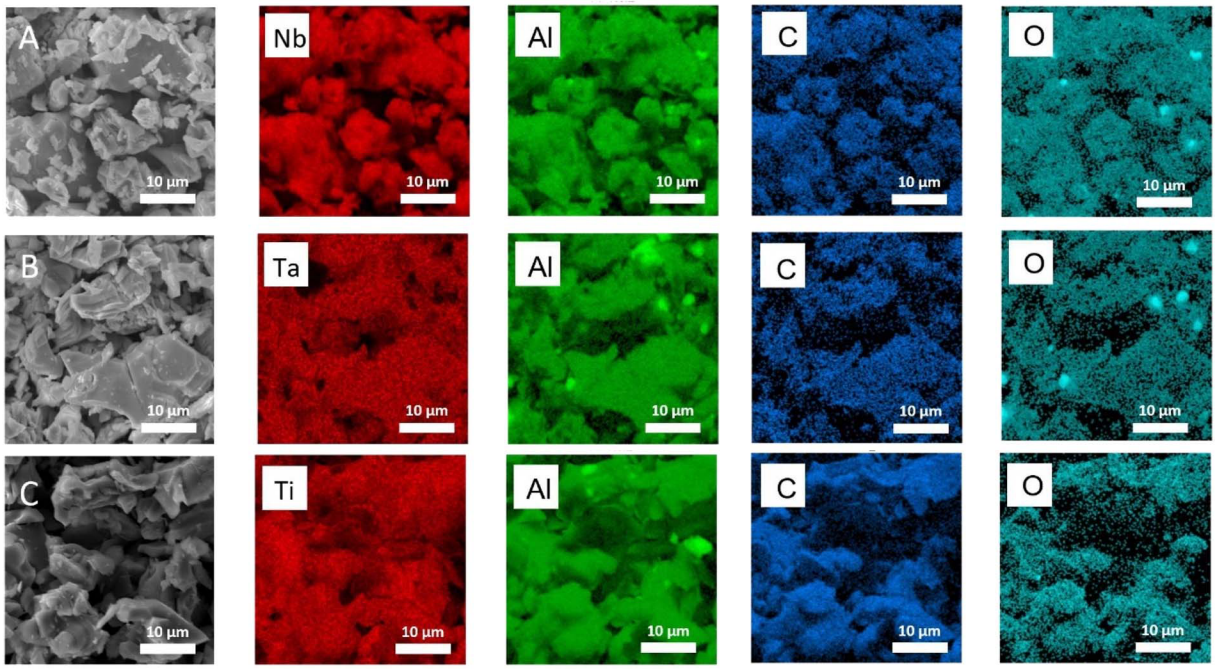

Fig. 3 EDS mapping of MAX phases, Nb_2AlC (A), Ta_2AlC (B), and Ti_3AlC_2 (C), showing the corresponding metal (Nb, Ta or Ti), Al, C, and O. The scale bars are 10 µm.

(453.7 eV, 459.8 eV),[66] and those of the oxidation state Ti^{4+} (458.6 eV, 464.2 eV),[67] which indicated the existence of TiO_2. The deconvolution of the Al 2p region of all the MAX validated what was deducted from EDS mapping. The wide peak at 74.4 eV indicated the presence of Al_2O_3, Al–O and Al–OH in the three MAX.[68] The detailed analysis of the C 1s region presented similar characteristics for all MAX, with the peak correlated to the adventitious carbon (285.0 eV), and the metal carbide peak of the analysed material (Nb–C 282.8 eV,[69] Ta–C 282.5 eV,[69] and Ti–C 281.3 eV[65]). The deconvolution of the O 1s region confirmed the presence of the corresponding transition metal oxides detected from the high-resolution spectrum of the transition metals of the MAX, in particular the Nb_2O_5 peak at 530.3 eV,[62] Ta_2O_5 at 530.2 eV,[64] and TiO_2 at 529.7 eV.[67] Similarly, the peak in the O 1s region related to Al_2O_3 (531.3 eV)[68] was detected in all the MAX.

Except for a few aluminium oxide particles detected from the EDS mapping in Fig. 3, in general, no visibly different structures were noticed from the SEM images in Fig. 2. It is apparent from the EDX and XPS analyses that all MAX contain a certain amount of their respective transition metal oxides and aluminium oxides (and hydroxides) in the bulk and on the surface. Moreover, the XRD patterns of MAX phases, reported in Fig. S4,† confirmed the presence of MAX phases[70–72] and traces of Al_2O_3,[72] but without the corresponding metal oxides. On the other hand, the metal oxides detected with the surface-sensitive XPS analysis were not found with XRD measurements. The observations suggest the low concentration of the metal (Nb, Ta, Ti) oxides relative to the MAX and the poor crystallinity of these compounds. In general, the presence of the additional metal oxides that are not expected from the pure MAX would likely influence the properties and the electrochemical performances of the MAX, since metal oxides such as Nb_2O_5, Ta_2O_5, TiO_2 and Al_2O_3 are either photoactive or catalytically active, or both.[73–77]

The estimation of the optical band gap of the MAX was obtained based on diffuse reflectance measurements. The Kubelka–Munk (K–M) model[53] was applied in the calculation of the absorption coefficient of thick powder samples and subsequently led to the band gap extrapolation from the Tauc plot, through graphical methods. Assuming direct transition for the MAX, Fig. 5A–C show the Tauc plots transformed from the reflectance measurement (eqn (3)). Details of the optical bandgap estimation are given in the Experimental section. The estimation of the band gap value is usually obtained using the Tauc plot graphical method for semiconductor materials but, in this work, materials characterisations showed the co-existence of more than a single semiconductor compound in the MAX. For this reason, the "baseline method" was adopted, also applying a linear fit to the slope right below the fundamental absorption (baseline, solid line) and the band gap was extrapolated from the intersection of the two fitted lines.[55] Nb_2AlC and Ta_2AlC showed two different steep regions, indicating the presence of two different photoactive semiconductors, thus, two band gap values were obtained, 2.2 eV and 3.1 eV for Nb_2AlC, and 2.2 eV and 3.3 eV for Ta_2AlC. Ti_3AlC_2 presented only one fundamental absorption with a band gap of 2.4 eV. The estimation of the band gap was also performed assuming indirect transitions, as shown in Fig. S5.† The calculated values agreed with the ones previously discussed, differing by about 0.1 eV. Considering what was observed from the materials characterisation, the different band gaps can be related to the different metal oxides detected with XPS analyses. It was reported that

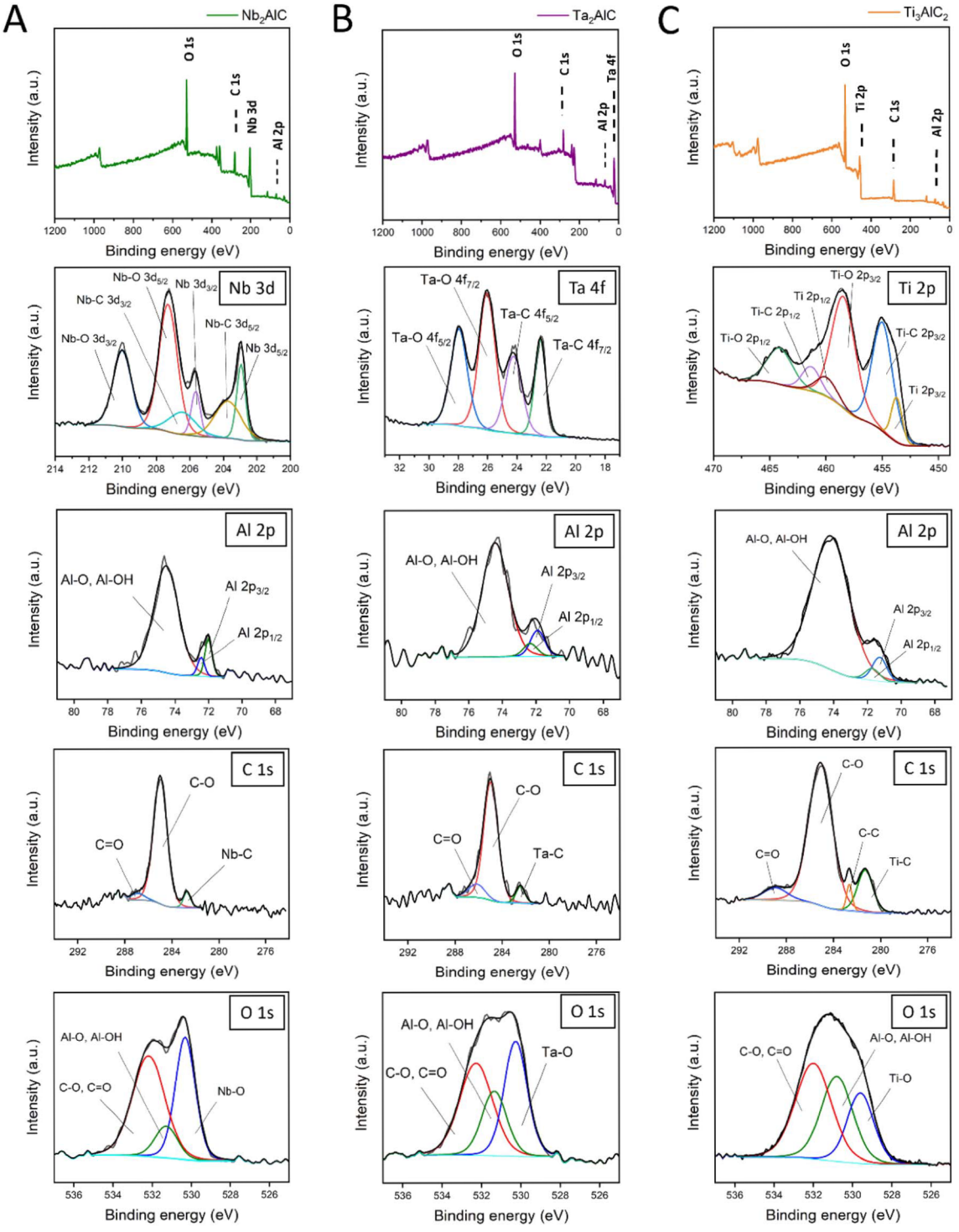

Fig. 4 XPS spectra of MAX phases, Nb_2AlC (A), Ta_2AlC (B), and Ti_3AlC_2 (C) with high-resolution analysis of metal (Nb 3d, Ta 4f or Ti 2p), Al 2p, C 1s, and O 1s. The main XPS peak for each element is labelled in the survey spectrum.

the band gap of Nb_2O_5 can vary between 3.1 eV and 5.3 eV,[78] while for Ta_2O_5 it was reported that the experimental band gap is between 3.6 eV and 4.0 eV.[79–81] The latter differs from the calculated value but it is also important to highlight that the equation developed by Tauc referred to amorphous materials, therefore the presence of crystalline phases can lead to the underestimation of the band gap.[82,83] Moreover, the absorption spectra of Nb_2AlC, Ta_2AlC, and Ti_3AlC_2 (Fig. S6†) confirmed that all the MAX showed absorptions in the visible and UV region.

The material characterisations highlighted two features that are common to all the MAX: the presence of Al_2O_3 detected by EDS and XPS, and the existence of a material that possesses

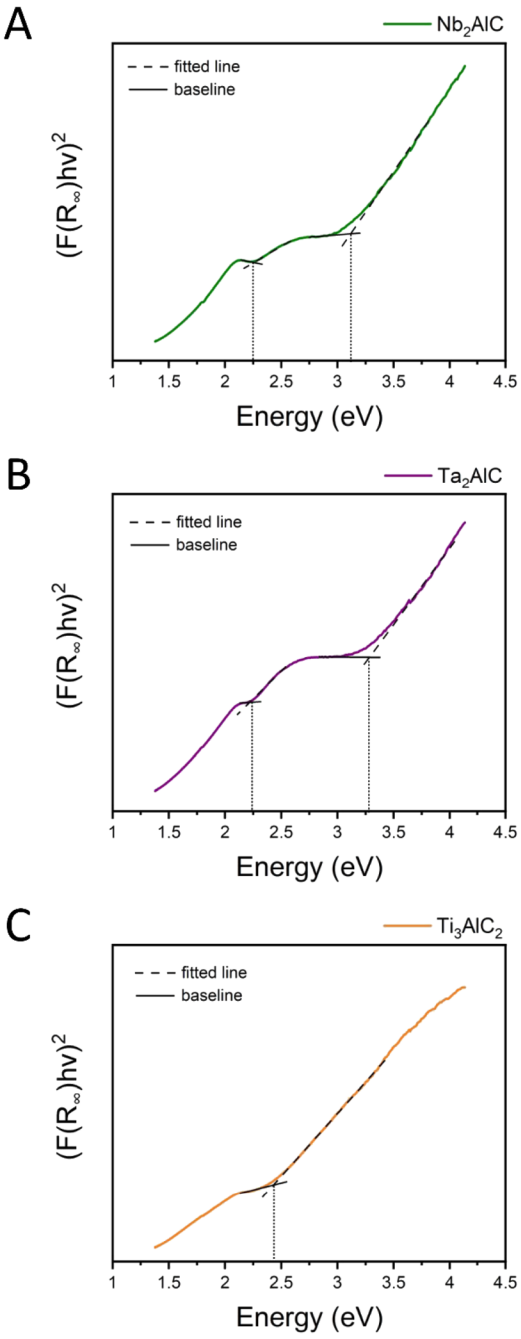

Fig. 5 Tauc plots of the Kubelka–Munk function calculated from the reflectance spectra of Nb_2AlC (A), Ta_2AlC (B), and Ti_3AlC_2 (C), assuming direct transitions. The dashed and solid black lines show the fitted line from the Tauc method and the baseline, respectively. The estimation of the band gap value corresponds to the abscissa of the intersection of the two lines, as shown by the dotted vertical line.

a band gap around 2.2–2.4 eV, extrapolated from the Tauc plots. Al_2O_3 is an insulator that is not supposed to absorb light, since it possesses a wide band gap between 5.1 eV and 7.6 eV, depending on the crystalline form and the synthesis method.[84] However, it was reported that Al_2O_3 can be applied in the photodegradation of phenolic compounds under the influence of UV light.[73,74] In particular, it was reported how the band gap of the Al_2O_3 synthesised by the sol–gel method changed dramatically based on the annealing temperature, ascribed to the hydroxyl groups of the material. These functionalities are responsible for the photoresponse since they allow the absorption of molecules that can form reactive oxygen species, involved in the degradation process.[73] The presence of Al–OH groups was detected in all MAX used in this work, as shown in Fig. 4. However, it is difficult to understand their role in the photocatalytic process since they are impurities that formed spontaneously due the exposure to air and they cannot easily be isolated to investigate in detail their exact composition and properties. In contrast to the theoretical calculation that all three MAX have continuous DOS and band structures without a gap, indicating a metallic behaviour, the experimental evaluation shows that the MAX with mixed metal oxides, as a whole, possess optical band gaps with semiconductor characteristics and potentially demonstrate photoresponses.

To verify the hypothesis, linear sweep voltammetry was used to test the photoelectrochemical activity of MAX for HER under the influence of illumination at different wavelengths. The wavelength of the light sources was chosen based on the estimated band gaps mentioned above, covering the region of the electromagnetic spectrum that goes from ultraviolet (UV, 365 nm), close to the start (blue, 460 nm) and the end (red, 660 nm) of the visible region. Fig. 6A–C show that considering the overpotential at -10 mA cm^{-2}, all MAX presented a lower overpotential compared to the bare screen-printed carbon electrodes (SPCE, dashed line), measured for reference. Generally, exposure to the light led to better performances for all MAX. Nb_2AlC showed the lowest overpotential under the influence of UV light (758 mV), followed by the red (814 mV), and the blue light sources (863 mV), as compared to non-illuminated (904 mV). Ta_2AlC also presented a decreased overpotential of 760 mV, 787 mV, and 811 mV when illuminated by 365 nm, 460 nm, and 660 nm light, respectively. The electrode measured without illumination again presented the highest overpotential (863 mV). As mentioned above, both MAX performed better after exposure to UV light, thanks to the presence of the respective transition metal oxides (Nb_2O_5 and Ta_2O_5) that are known to be active in the UV region. However, Ti_3AlC_2 exhibited an overpotential of 814 mV in the dark and showed the best photoactivity when exposed to visible light, presenting an overpotential of 680 mV with the blue source and 697 mV with the red one, but was less active when illuminated by UV light, with an overpotential of 736 mV. This trend agrees with the fundamental absorption in the visible region and the deduced band gap (2.4 eV) shown in Fig. 5C. The results agree with the photoactivity of MAX in the literature.[33,34]

Eventually, chronoamperometry measurements (Fig. S7†) were performed in the same electrolyte switching on/off the light source (660 nm) to confirm the photoelectrochemical response reported in Fig. 6. The results showed that all MAX exhibited a larger current increment during illumination as compared to the bare GC. In particular, Nb_2AlC showed the most prominent increase in current, followed by Ti_3AlC_2 and Ta_2AlC. The results obtained agree with the trend of the polarisation curves in Fig. 6.

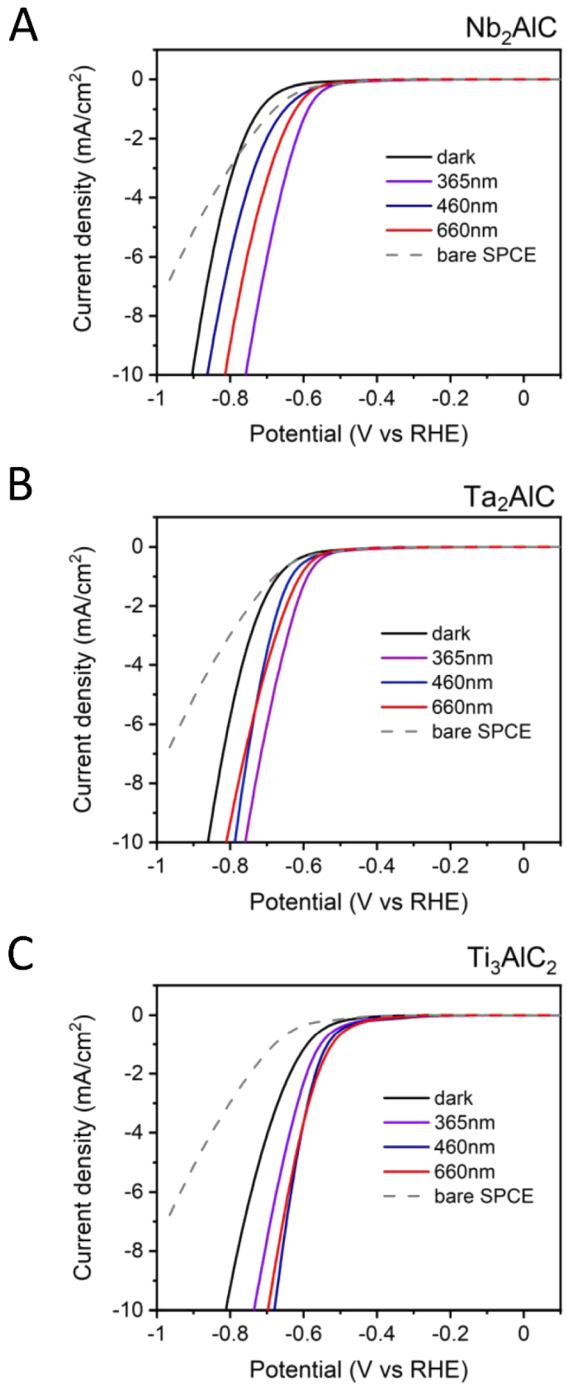

Fig. 6 Linear sweep voltammograms of MAX phases, Nb_2AlC (A), Ta_2AlC (B), and Ti_3AlC_2 (C) supported by SPCE measured in 0.5 M H_2SO_4 electrolyte; scan rate 5 mV s^{-1}. The measurements were carried out in the dark and then the sample was exposed to light sources of different wavelengths.

The application of the Nb_2AlC, Ta_2AlC and Ti_3AlC_2 as photoelectrocatalysts for hydrogen production reinforced the hypothesis that the detected metal oxide impurities contributed significantly to the photoactivity of these materials, as schematically shown in Scheme 3. Furthermore, surface engineering

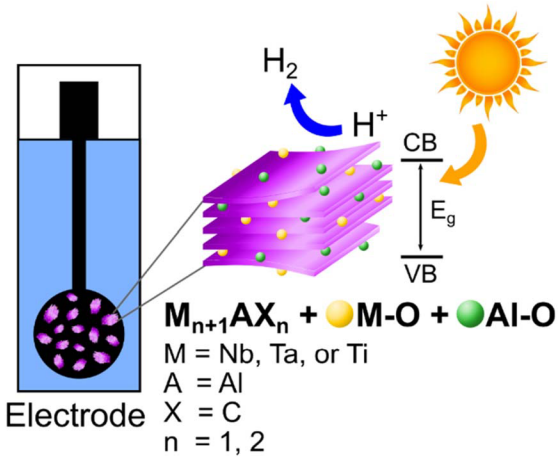

Scheme 3 Representation of the mechanism of the photoelectrochemical HER, where the oxide impurities take part in the photoelectrocatalytic process.

can be used to tune the properties of these materials and optimise their performance in energy-related applications.

Conclusion

In summary, we studied the properties of three MAX phases, Nb_2AlC, Ta_2AlC, and Ti_3AlC_2, using theoretical and experimental approaches to investigate the origin of their photoactivity. The theoretical calculations conclude that the metals contribute dominantly to the DOS around the Fermi level, confirming the metallic nature of these compounds, with no band gap in the vicinity of the Fermi level. XPS and EDS analyses detected not only the presence of the respective transition metal oxides but also a relevant amount of Al_2O_3. In contrast to the theoretical calculation, it was experimentally estimated that for Nb_2AlC and Ta_2AlC, there are two fundamental absorptions at 2.2 eV, 3.1 eV, and 2.2 eV, 3.3 eV, respectively. Moreover, the estimated band gap for Ti_3AlC_2 was 2.4 eV. As a confirmation of the presence of photoactive material, all MAX showed enhanced photocatalytic activity towards the HER when exposed to illumination by different light sources. In particular, Nb_2AlC and Ta_2AlC performed better (758 mV and 760 mV of overpotential, respectively) when exposed to UV light, and Ti_3AlC_2 showed the lowest overpotential (680 mV) when exposed to the 460 nm light source, in accordance with the estimated optical band gaps. In general, the formation of oxides on MAX phases has been already reported, since contamination is unavoidable if the material comes in contact with the air or with oxidising solvents.[85,86] In this work, we showed how these impurities can play a crucial role in photoelectrochemical hydrogen generation, leading to better performances thanks to their intrinsic photoactivity. These findings can open the door for further implementation of MAX phases as photoelectrocatalysts. In addition to the three MAX investigated in this work, more than 150 other MAX phases[87] synthesised to date might demonstrate similar photoactive properties, which are yet to be tested and possibly applied in this field.

Author contributions

M. S: material characterisation (SEM, EDS, XPS and optical measurements), electrochemical measurements, data analysis, original draft. K. N.: theoretical calculations (DOS, band structure), material characterisation (XRD, CLSM), data analysis, original draft. S. N.: conceptualisation, data analysis, editing and revision of the manuscript. M. C.: funding acquisition, supervision of theoretical part, editing and revision of the manuscript. M. P.: funding acquisition, supervision of the experimental part, conceptualisation, editing and revision of the manuscript.

Conflicts of interest

There are no conflicts to declare.

Acknowledgements

The authors acknowledge CzechNanoLab project at CEITEC Nano Research Infrastructure (LM2018110, MEYS CR) for the support in material characterisation. M. S. acknowledges the financial support from JCMM and all partners for the Brno PhD Talent scholarship, financed by the Brno City Municipality. M. S. and K. N. acknowledge the project Quality Internal Grants of BUT (KInG BUT), Reg. No. CZ.02.2.69/0.0/0.0/19_073/0016948, which is financed from the OP RDE. M. P. acknowledges the Grant Agency of the Czech Republic (GACR EXPRO: 19–26896X). M. Č. acknowledges the M-ERA.Net project No. TH71020004 (HYSUCAP).

References

1 J. Gong, C. Li and M. R. Wasielewski, *Chem. Soc. Rev.*, 2019, **48**, 1862–1864.
2 B. A. Pinaud, J. D. Benck, L. C. Seitz, A. J. Forman, Z. Chen, T. G. Deutsch, B. D. James, K. N. Baum, G. N. Baum, S. Ardo, H. Wang, E. Miller and T. F. Jaramillo, *Energy Environ. Sci.*, 2013, **6**, 1983–2002.
3 M. D. Islam, I. Kubo, M. Ohadi and A. A. Alili, *Appl. Energy*, 2009, **86**, 511–515.
4 T. Hisatomi, J. Kubota and K. Domen, *Chem. Soc. Rev.*, 2014, **43**, 7520–7535.
5 X. Yu, M. S. Prévot, N. Guijarro and K. Sivula, *Nat. Commun.*, 2015, **6**, 7596.
6 S. Koumi Ngoh and D. Njomo, *Renewable Sustainable Energy Rev.*, 2012, **16**, 6782–6792.
7 I. S. Cho, Z. Chen, A. J. Forman, D. R. Kim, P. M. Rao, T. F. Jaramillo and X. Zheng, *Nano Lett.*, 2011, **11**, 4978–4984.
8 R. Van De Krol, Y. Liang and J. Schoonman, *J. Mater. Chem.*, 2008, **18**, 2311–2320.
9 L. Wang, R. Liang, T. Zhou, J. Zheng, B. M. Liang, H. P. Zhang, F. M. Luo, P. G. Gibson and G. Wang, *Ann. Allergy, Asthma Immunol.*, 2017, **119**, 324–332.
10 O. Monfort, L. C. Pop, S. Sfaelou, T. Plecenik, T. Roch, V. Dracopoulos, E. Stathatos, G. Plesch and P. Lianos, *Chem. Eng. J.*, 2016, **286**, 91–97.
11 S. Han, Y. C. Pu, L. Zheng, L. Hu, J. Z. Zhang and X. Fang, *J. Mater. Chem. A*, 2016, **4**, 1078–1086.
12 S. Dolai, P. Maiti, A. Ghorai, R. Bhunia, P. K. Paul and D. Ghosh, *ACS Appl. Mater. Interfaces*, 2021, **13**, 438–448.
13 K. Ghosh, S. Ng, C. Iffelsberger and M. Pumera, *Appl. Mater. Today*, 2022, **26**, 101301.
14 S. Ng, R. Zazpe, J. Rodriguez-Pereira, J. Michalička, J. M. Macak and M. Pumera, *J. Mater. Chem. A*, 2021, **9**, 11405–11414.
15 S. Ng, J. Sturala, J. Vyskocil, P. Lazar, J. Martincova, J. Plutnar and M. Pumera, *ACS Nano*, 2021, **15**, 11681–11693.
16 K. N. Dinh, Y. Zhang, J. Zhu and W. Sun, *Chem. – A Eur. J.*, 2020, **26**, 6437–6446.
17 K. P. Akshay Kumar, K. Ghosh, O. Alduhaish and M. Pumera, *Electrochem. Commun.*, 2021, **122**, 106890.
18 Z. W. Seh, K. D. Fredrickson, B. Anasori, J. Kibsgaard, A. L. Strickler, M. R. Lukatskaya, Y. Gogotsi, T. F. Jaramillo and A. Vojvodic, *ACS Energy Lett.*, 2016, **1**, 589–594.
19 M. Sokol, V. Natu, S. Kota and M. W. Barsoum, *Trends Chem.*, 2019, **1**, 210–223.
20 M. W. Barsoum and M. Radovic, *Annu. Rev. Mater. Res.*, 2011, **41**, 195–227.
21 Z. M. Sun, *Int. Mater. Rev.*, 2011, **56**, 143–166.
22 N. F. Rosli, M. Z. M. Nasir, N. Antonatos, Z. Sofer, A. Dash, J. Gonzalez-Julian, A. C. Fisher, R. D. Webster and M. Pumera, *ACS Appl. Nano Mater.*, 2019, 6010–6021.
23 M. Radovic and M. W. Barsoum, *Am. Ceram. Soc. Bull.*, 2013, **92**, 20–27.
24 M. Malaki, A. Maleki and R. S. Varma, *J. Mater. Chem. A*, 2019, **7**, 10843–10857.
25 Y. Cheng, L. Wang, Y. Song and Y. Zhang, *J. Mater. Chem. A*, 2019, **7**, 15862–15870.
26 M. Khazaei, A. Ranjbar, K. Esfarjani, D. Bogdanovski, R. Dronskowski and S. Yunoki, *Phys. Chem. Chem. Phys.*, 2018, **20**, 8579–8592.
27 A. VahidMohammadi, J. Rosen and Y. Gogotsi, *Science*, 2021, **372**, eabf1581.
28 M. Naguib, O. Mashtalir, J. Carle, V. Presser, J. Lu, L. Hultman, Y. Gogotsi and M. W. Barsoum, *ACS Nano*, 2012, **6**, 1322–1331.
29 O. Mashtalir, M. Naguib, V. N. Mochalin, Y. Dall'Agnese, M. Heon, M. W. Barsoum and Y. Gogotsi, *Nat. Commun.*, 2013, **4**, 1–7.
30 J. C. Lei, X. Zhang and Z. Zhou, *Front. Phys.*, 2015, **10**, 276–286.
31 K. A. Novčić, C. Iffelsberger and M. Pumera, *J. Mater. Chem. A*, 2022, **10**, 3206–3215.
32 K. P. Akshay Kumar, O. Alduhaish and M. Pumera, *Electrochem. Commun.*, 2021, **125**, 106977.
33 M. Sanna, S. Ng, J. V. Vaghasiya and M. Pumera, *ACS Sustainable Chem. Eng.*, 2022, **10**, 2793–2801.
34 B. Shalini Reghunath, D. Davis and K. R. Sunaja Devi, *Chemosphere*, 2021, **283**, 131281.
35 J. Gertzen, P. Levecque, T. Rampai and T. van Heerden, *Mater. (Basel).*, 2021, **14**, 1–12.
36 X. Qian, Y. Li, X. He, H. Fan and S. Yun, *J. Phys. Chem. Solids*, 2011, **72**, 954–956.

37 I. Thomé, A. Nijs and C. Bolm, *Chem. Soc. Rev.*, 2012, **41**, 979–987.
38 S. L. Buchwald and C. Bolm, *Angew. Chem.*, 2009, **121**, 5694–5695.
39 P.-F. Larsson, A. Correa, M. Carril, P.-O. Norrby and C. Bolm, *Angew. Chem.*, 2009, **121**, 5801–5803.
40 N. E. Leadbeater and M. Marco, *J. Org. Chem.*, 2003, **68**, 5660–5667.
41 C. E. Banks, A. Crossley, C. Salter, S. J. Wilkins and R. G. Compton, *Angew. Chem., Int. Ed.*, 2006, **45**, 2533–2537.
42 B. Šljukić, C. E. Banks and R. G. Compton, *Nano Lett.*, 2006, **6**, 1556–1558.
43 C. H. An Wong, Z. Sofer, M. Kubešová, J. Kučera, S. Matějková and M. Pumera, *Proc. Natl. Acad. Sci. U. S. A.*, 2014, **111**, 13774–13779.
44 L. Wang, Z. Sofer and M. Pumera, *ACS Nano*, 2020, **14**, 21–25.
45 N. Mohamad Latiff, L. Wang, C. C. Mayorga-Martinez, Z. Sofer, A. C. Fisher and M. Pumera, *Nanoscale*, 2016, **8**, 16752–16760.
46 R. J. Toh, Z. Sofer, J. Luxa and M. Pumera, *ChemCatChem*, 2017, **9**, 1168–1171.
47 M. Pumera, *ACS Catal.*, 2020, **10**, 7087–7092.
48 M. P. Browne, V. Urbanova, J. Plutnar, F. Novotný and M. Pumera, *J. Mater. Chem. A*, 2020, **8**, 1120–1126.
49 S. M. Tan and M. Pumera, *ACS Nano*, 2019, **13**, 2681–2728.
50 X. J. Chua, S. M. Tan, X. Chia, Z. Sofer, J. Luxa and M. Pumera, *Chem. – A Eur. J.*, 2017, **23**, 3169–3177.
51 K. R. Ward, M. Gara, N. S. Lawrence, R. S. Hartshorne and R. G. Compton, *J. Electroanal. Chem.*, 2013, **695**, 1–9.
52 K. Momma and F. Izumi, *J. Appl. Crystallogr.*, 2011, **44**, 1272–1276.
53 P. Kubelka and F. Munk, *Z. Tech. Phys.*, 1931, **12**, 593–601.
54 J. Tauc, *Mat. Res. Bull.*, 1968, **3**, 37–46.
55 P. Makuła, M. Pacia and W. Macyk, *J. Phys. Chem. Lett.*, 2018, **9**, 6814–6817.
56 A. Kaliyaraj Selva Kumar, Y. Zhang, D. Li and R. G. Compton, *Electrochem. Commun.*, 2020, **121**, 106867.
57 Z. U. Din Babar, J. Fatheema, N. Arif, M. S. Anwar, S. Gul, M. Iqbal and S. Rizwan, *RSC Adv.*, 2020, **10**, 25669–25678.
58 A. J. Xu, W. W. Zhong and X. Zhang, *Comput. Condens. Matter*, 2016, **6**, 1–4.
59 X. H. Wang and Y. C. Zhou, *J. Mater. Sci. Technol.*, 2010, **26**, 385–416.
60 T. A. Sasaki and Y. Baba, *Phys. Rev. B: Condens. Matter Mater. Phys.*, 1985, **31**, 791–797.
61 A. Darlinski, *IEEE Trans. Magn.*, 1987, **23**, 1381–1384.
62 N. Özer, M. D. Rubin and C. M. Lampert, *Sol. Energy Mater. Sol. Cells*, 1996, **40**, 285–296.
63 T. Anazawa, S. Tokumitsu, R. Sekine, E. Miyazaki, K. Edamoto, H. Kato and S. Otani, *Surf. Sci.*, 1995, **328**, 263–268.
64 S. F. Ho, S. Contarini and J. W. Rabalais, *J. Phys. Chem.*, 1987, **91**, 4779–4788.
65 J. Luthin and C. Linsmeier, *Phys. Scr. T*, 2001, **91**, 134–137.
66 A. A. Galuska, J. C. Uht and N. Marquez, *J. Vac. Sci. Technol., A*, 1988, **6**, 110–122.
67 M. C. Biesinger, L. W. M. Lau, A. R. Gerson and R. S. C. Smart, *Appl. Surf. Sci.*, 2010, **257**, 887–898.
68 J. Van den Brand, W. G. Sloof, H. Terryn and J. H. W. De Wit, *Surf. Interface Anal.*, 2004, **36**, 81–88.
69 L. Ramqvist, K. Hamrin, G. Johansson, A. Fahlman and C. Nordling, *J. Phys. Chem. Solids*, 1969, **30**, 1835–1847.
70 A. Liu, Q. Yang, X. Ren, F. Meng, L. Gao, M. Gao, Y. Yang, T. Ma and G. Wu, *Ceram. Int.*, 2020, **46**, 6934–6939.
71 T. H. Scabarozi, J. Roche, A. Rosenfeld, S. H. Lim, L. Salamanca-Riba, G. Yong, I. Takeuchi, M. W. Barsoum, J. D. Hettinger and S. E. Lofland, *Thin Solid Films*, 2009, **517**, 2920–2923.
72 C. L. Yeh and Y. S. Chen, *Ceram. Int.*, 2017, **43**, 15659–15665.
73 F. Tzompantzi, Y. Piña, A. Mantilla, O. Aguilar-Martínez, F. Galindo-Hernández, X. Bokhimi and A. Barrera, *Catal. Today*, 2014, **220–222**, 49–55.
74 Y. Piña-Pérez, F. Tzompantzi-Morales, R. Pérez-Hernández, R. Arroyo-Murillo, P. Acevedo-Peña and R. Gómez-Romero, *Fuel*, 2017, **198**, 11–21.
75 M. Ni, M. K. H. Leung, D. Y. C. Leung and K. Sumathy, *Renewable Sustainable Energy Rev.*, 2007, **11**, 401–425.
76 S. Furukawa, Y. Ohno, T. Shishido, K. Teramura and T. Tanaka, *ACS Catal.*, 2011, **1**, 1150–1153.
77 V. Gurylev, *Mater. Today Sustain.*, 2022, **18**, 100131.
78 R. A. Rani, A. S. Zoolfakar, A. P. O'Mullane, M. W. Austin and K. Kalantar-Zadeh, *J. Mater. Chem. A*, 2014, **2**, 15683–15703.
79 R. M. Fleming, D. V. Lang, C. D. W. Jones, M. L. Steigerwald, D. W. Murphy, G. B. Alers, Y. H. Wong, R. B. Van Dover, J. R. Kwo and A. M. Sergent, *J. Appl. Phys.*, 2000, **88**, 850–862.
80 W. J. Chun, A. Ishikawa, H. Fujisawa, T. Takata, J. N. Kondo, M. Hara, M. Kawai, Y. Matsumoto and K. Domen, *J. Phys. Chem. B*, 2003, **107**, 1798–1803.
81 F. Z. Tepehan, F. E. Ghodsi, N. Ozer and G. G. Tepehan, *Sol. Energy Mater. Sol. Cells*, 1997, **46**, 311–321.
82 A. Dolgonos, T. O. Mason and K. R. Poeppelmeier, *J. Solid State Chem.*, 2016, **240**, 43–48.
83 G. Gal, Y. Mastai, G. Hodes and L. Kronik, *J. Appl. Phys.*, 1999, **86**, 5573–5577.
84 E. O. Filatova and A. S. Konashuk, *J. Phys. Chem. C*, 2015, **119**, 20755–20761.
85 K. Chen, N. Qiu, Q. Deng, M. H. Kang, H. Yang, J. U. Baek, Y. H. Koh, S. Du, Q. Huang and H. E. Kim, *ACS Biomater. Sci. Eng.*, 2017, **3**, 2293–2301.
86 S. Myhra, J. A. A. Crossley and M. W. Barsoum, *J. Phys. Chem. Solids*, 2001, **62**, 811–817.
87 R. Khaledialidusti, M. Khazaei, S. Khazaei and K. Ohno, *Nanoscale*, 2021, **13**, 7294–7307.

Part 2: 3D printing for the development of functional electrodes for photoelectrochemical applications

8. Heterolayered carbon allotrope architectonics via multi-material 3D printing for advanced electrochemical devices

Published paper included in this chapter:

Palacios-Corella, M.; **Sanna, M.**; Muñoz, J.; Ghosh, K.; Wert, S.; Pumera, M., Heterolayered carbon allotrope architectonics via multi-material 3D printing for advanced electrochemical devices, *Virtual and Physical Prototyping*, **2023**, 18:1.

8.1. Motivation for the study

Despite the remarkable strides made in 3D printing technology, the insulating nature of commonly employed polymer-based filaments poses a challenge for electronic applications. Carbon allotropes embedded in polymer matrices have been developed to enhance filament conductivity, leading to the advent of 3D-printed carbon electrodes to address this limitation. Carbon nanomaterials, renowned for their exceptional properties at the nanoscale, have garnered significant attention for electrochemical sensing applications. This work explores the potential of multi-material 3D printing for engineering heterolayered structures, particularly focusing on carbon allotropes. By leveraging a print-pause-print approach, we seek to integrate diverse carbon filaments in a time-efficient manner, paving the way for the precise engineering of 3D-printed carbon electrodes with enhanced functionalities. The incorporation of heterolayers holds promise for augmenting electrochemical performance, with implications for energy conversion and chemical sensing applications.

8.2. Paper conclusion

In this study, we present the fabrication of heterolayered 3D-printed carbon electrodes for the first time, employing multi-material 3D printing. These electrodes are composed of alternating commercially available CNT/PLA and CB/PLA conductive nanocomposite filaments. Following chemical activation, morphological characterization unveiled an asymmetric surface exposing both 1D and 3D nanocarbon allotropes. Electrochemical analysis revealed that the electrodes exhibit intermediate electrochemical properties compared to electrodes made solely of individual carbon allotropes, although statistical analysis did not show significant differences between the electrodes. However, in applications such as the HER or the detection of ascorbic acid AA, multimaterial 3D-printed carbon electrodes outperformed electrodes made solely from a single carbon allotrope. This improvement is attributed to the heterolayered structure of the electrodes, facilitating the presence of metallic impurities in multimaterial 3D-printed carbon electrodes compared to CB electrodes, as well as the larger active area of multimaterial 3D-printed carbon electrodes compared to CNT electrodes. Thus, the multimaterial printing approach presented here, based on alternating layers of different carbon filaments, offers a convenient, rapid, and scalable method for producing carbon electrodes with enhanced performance. Furthermore, this strategy lays the groundwork for developing a new generation of heterolayered 3D-printed electrodes incorporating various electroactive materials, such as 2D materials, which holds promise for creating heterolayered structures applicable in supercapacitors, batteries, or biosensors.

8.3. Author contribution

In this work, I performed the electrochemical measurements and the statistical study related to the obtained result. I participated to the data analysis and plotted the significance findings obtained from the electrochemical measurements.

VIRTUAL AND PHYSICAL PROTOTYPING
2023, VOL. 18, NO. 1, e2276260 (14 pages)
https://doi.org/10.1080/17452759.2023.2276260

Taylor & Francis
Taylor & Francis Group

Heterolayered carbon allotrope architectonics *via* multi-material 3D printing for advanced electrochemical devices

Mario Palacios-Corella[a], Michela Sanna[a], José Muñoz[a], Kalyan Ghosh[a], Stefan Wert[a] and Martin Pumera[a,b,c]

[a]Future Energy and Innovation Laboratory, Central European Institute of Technology, Brno University of Technology, Brno, Czech Republic; [b]Faculty of Electrical Engineering and Computer Science, VSB – Technical University of Ostrava, Ostrava, Czech Republic; [c]Department of Medical Research, China Medical University Hospital, China Medical University, Taichung, Taiwan

ABSTRACT

3D printing has become a powerful technique in electrochemistry for fabricating electrodes, thanks to readily available conductive nanocomposite filaments, such as those based on carbon fillers (i.e., carbon nanotubes (CNTs) or carbon black (CB)) within an insulating polymeric matrix like polylactic acid (PLA). Inspired by inorganic heterostructures that enhance the functional characteristics of nanomaterials, we fabricated hetero-layered 3D printed devices based on carbon allotropes using a layer-by-layer assembly approach. The heterolayers were customised through the alternate integration of different carbon allotrope filaments via a multi-material 3D printing technique, allowing for a time-effective method to enhance electrochemical performance. As a first demonstration of applicability, CNT/PLA and CB/PLA filaments were utilised to construct ordered hetero-layered carbon-based electrodes. This contrasts with conventional methods where various carbon species are mixed in the same composite-based filament used for building electrochemical devices. Multi-material 3D-printed carbon electrodes exhibit improved electrochemical performance in energy conversion (e.g., hydrogen evolution reaction or HER) and sensing applications (e.g., ascorbic acid detection) compared to single-material electrodes. This work paves the way for manufacturing advanced 3D-printed heterolayered electrodes with enhanced electrochemical activity through multi-material 3D printing technology.

ARTICLE HISTORY
Received 28 February 2023
Accepted 19 October 2023

KEYWORDS
Additive manufacturing; fused deposition modelling; electrocatalysis; electrochemistry; carbon allotropes

1. Introduction

3D printing (also termed additive manufacturing) is probably one of the most revolutionary technologies developed during the twentieth century [1]. By following a bottom-up approach, 3D printing has gathered increasing interest in recent years as it allows for the fast production of structures by taking advantage of a layer-by-layer deposition of the desired material. The increasing amount of users has facilitated its fast development and implementation in many manufacturing processes [2]. Complex geometries, a very low amount of waste, and cost-effective production of structuralised materials are the principal benefits [3] of this technique that hasn't gone unnoticed by the scientific community. In this line, during the last decade, 3D printing has been exploited in the fabrication of structures employed in a wealth of scientific fields [4] and applications, such as (bio)sensing [5–14], (electro)catalysis [15–20], or microrobotics [21–24]. The high applicability of 3D printing has also reached the attention of the electrochemistry community due to its potential applicability for the printing of 3D electrodes [25], preparation of logic gates [26], processors [27], or devising of electrochemical energy storage devices [28–32]. Particularly, for electronics manufacturing, fused deposition modelling (FDM) is one of the most appealing 3D printing methods because of its versatility and fast preparation of products [33]. In FDM, polymer-based filaments are molten in a movable nozzle to create the individual layers that compose the final object. Within the extensive library of polymers employed to prepare filaments, polylactic acid (PLA), acrylonitrile butadiene styrene (ABS), or Nylon could be highlighted as the most recurrent. However, the insulating nature of these polymers hinders their direct use for electronic applications.

CONTACT Martin Pumera martin.pumera@gmail.com Future Energy and Innovation Laboratory, Central European Institute of Technology, Brno University of Technology, Purkyňova 123, Brno 61200, Czech Republic; Faculty of Electrical Engineering and Computer Science, VSB – Technical University of Ostrava, 17. listopadu 2172/15, Ostrava 70800, Czech Republic; Department of Medical Research, China Medical University Hospital, China Medical University, No. 91 Hsueh-Shih Road, Taichung 40402, Taiwan

Supplemental data for this article can be accessed online at https://doi.org/10.1080/17452759.2023.2276260.

To increase their conductivity, filaments consisting of mixtures of carbon allotropes embedded in a polymer matrix have been developed and commercialised, such as graphite/ABS [34,35], carbon nanotubes (CNTs)/PLA [36,37], or carbon black (CB)/PLA [38–40], which in turn have paved the way for the advance in the electrochemistry field through the preparation of 3D-printed carbon electrodes (3D-PCEs) [40,41].

Carbon nanomaterials have emerged as strong candidates for electrochemical sensing due to their extraordinary properties on the nanoscale [42,43]. On the one hand, the diversity of chemical bonds displayed by carbon atoms, which can range from sp^3 to sp^1 hybridised states, give rise to different allotropic forms (e.g. CNTs, carbon fibres, fullerenes, etc.) that show distinct physicochemical properties and, additionally, exhibit different electrochemical surface area, conductivity or structure hybridisation [44]. However, besides these very interesting characteristics, carbon materials present intrinsic constraints that the materials science community has been minimising by merging them in harmoniously built heterostructures that consist of a layer-by-layer assembly of different 2D materials such as graphene/h-BN [45] or MoS_2/graphene [46]. The final heterostructures exhibit remarkable properties due to the synergistic effect of the parent single layers. These important results motivate even more the development of heterolayered 3D printed structures that could combine several functionalities. Indeed, since the first 3D printed structure was built, the technique has advanced considerably within the electrochemistry community, which has enabled the preparation of carbon composite filaments or inks [47] that can be further chemically modified [48], leading to improved or tunable properties of the final carbon electrode [49,50]. In addition, a combination of functionalities could easily be achieved in the future by integrating materials with very different properties. However, the development of heterostructures by 3D printing is nowadays an unmatured field.

Thus, 3D printing, through Multi-material 3D printing, can enable the precise engineering of heterolayers *via* a print-pause-print approach in which a second functional material can be integrated with the first material by temporal disruption of the printing process in a time-effective robotic controlled manner [51]. The multi-material 3D printing approach could be considered the FDM alternative to the electrochemical double nozzle approach [52,53], and reveals itself as a strong candidate for combining different carbon allotropes since it allows for combining different filaments at the user's demand contrasting with conventional 3D printing, where only one filament can be used for the printing of a single structure. Mechanically, in multi-material 3D printing, a robotic body with a rotating pulley barrel and a single extruder motor pull up different filaments when they must be loaded, allowing for a fast and fully automatised process. Thus, multi-material 3D printing would be a potential strategy to combine different carbon allotropes in 3D-PCEs *via* the formation of heterolayers. Importantly, the exploration of such heterolayered materials as 3D printed devices for electrochemical applications such as energy conversion (hydrogen evolution reaction, HER) or sensing of chemical species is an unexplored field and their study could pave the way towards more efficient sensors or energy devices.

Herein, the prototype of a heterolayered multi-material 3D-printed carbon electrode (MM 3D-PCE) has been devised *via* multi-material 3D printing technology by alternating the deposition of two different commercially available carbon filaments (i.e. PLA/CNT and PLA/CB). In the first section of the work, morphological and structural characterisation performed on all the electrodes show that an asymmetry is achieved in the MM 3D-PCE, exposing both carbon allotropes on the different surfaces of the electrode, contrary to that observed in the pure material electrodes. Electrochemical characterisation of the electrodes using cyclic voltammetry performed on a conventional ferrocenemethanol (FcMeOH) redox marker reveals that MM 3D-PCEs present hybrid features between those of 3D-PCEs purely based on CNT or CB filaments, giving rise to calculated electrochemical parameters between those of the pure materials, although statistical analysis reveals no significant differences between electrodes. In the second and third sections of the work, it is demonstrated that this intermediate behaviour turns into a superior electroactivity when the hydrogen evolution reaction (HER) is investigated, as the MM 3D-PCEs show an improved performance of around 40% compared to the closest pure material electrode. Similarly, when the detection of ascorbic acid (AA) is the object of study, the MM 3D-PCEs show improved response giving rise to a sensibility 1.2 times better than that of the pure material electrodes. Thus, this work offers a novel strategy for the development of MM 3D-PCEs *via* multi-material 3D printing for the preparation of advanced 3D-PCEs exhibiting improved electrochemical performances for task-specific applications.

2. Experimental

2.1. Materials and chemicals

The CB/PLA and CNT/PLA (brand name 'Black Magic') filaments used herein were commercially available and

purchased from Proto-Pasta, USA, and Graphene Laboratories Inc., USA, respectively. N,N-Dimethylformamide (DMF) used for the chemical activation of printed electrodes was purchased from Sigma-Aldrich, Germany. The electrochemical activity of the electrodes was studied in a 1.5 mM aqueous solution of ferrocenemethanol (FcMeOH, 99%, ABCR GmbH, Germany) and 0.2 M in potassium nitrate (KNO_3, analytical grade, Merck KGaA, Germany). For studying their activity for the HER, 0.5 M sulfuric acid (H_2SO_4, 96%, analytical grade, Penta, Czech Republic) was used. Deionised water with a resistivity >18.2 MΩ cm (Milli-Q Advantage A10 system, Germany) was used to prepare solutions. Ascorbic acid was purchased from Merck and used without further purification.

2.2. Apparatus and software

Modelling of the 3D-PCE was done using Autodesk Fusion 360 software. The slicing of the designed models was done using the PrusaSlicer 2.4.0 software. The electrodes were printed using a Prusa i3 MK3s printer which was upgraded with an MMU2s multi-material unit (Prusa Research, Czech Republic). A ruby-tipped 0.6 mm diameter nozzle (Olsson, 3DVerkstan, Sweden) was used for filament extrusion. The electrodes' morphology was assessed by scanning electron microscopy (SEM) using a LYRA 3 SEM (Tescan, Czech Republic). The surface composition of the materials was analysed by high-resolution X-ray photoelectron spectroscopy (XPS) using a Kratos (Axis Supra, UK), and Raman spectroscopy using an Alpha 300R (Witec, Oxford). Structural information was acquired by powder X-ray diffraction (PXRD) using a Rigaku Smartlab 3 kW (Rigaku, Japan). Electrochemical studies were carried out using a potentiostat (PGSTAT 204, Autolab, Netherlands). A Pt rod and an Ag/AgCl (saturated KCl) were used as counter and reference electrodes.

2.3. Electrode preparation

MM 3D-PCEs were printed *via* multi-material 3D printing technology and had a lollipop-like shape consisting of 4 alternating horizontal layers of CNT/CB materials as shown in Figure 1(B). The base layer was printed with CNT filament, while the second layer was printed with CB filament, and so on with the filament being automatically changed after each layer deposition to integrate CNT/CB heterolayers. Specifically, each layer was set to a thickness of 0.15 mm. The circular head of the electrodes had a radius of 3 mm (6mm diameter), and the electrode rod had a width of 3.5 and 15 mm in length. For all the electrodes in this work, a 0.6 mm nozzle heated to 220°C was employed to melt the filaments. The infill pattern was set to 15%, and the bed printing temperature was fixed to 60°C to ensure the best adhesion of

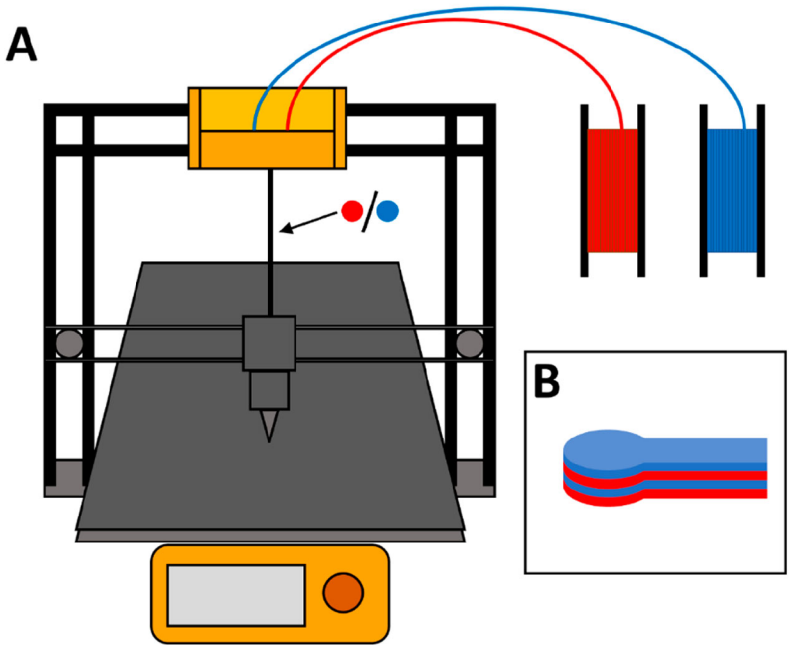

Figure 1. (A) Schematic representation of the multi-material 3D printer setup used to fabricate the heterolayered electrode by combining CNT (blue) and CB (red) filaments. (B) Schematic structure of the printed multi-material electrode with a total of four layers. Dimensions are not for scale.

the printed filament. For reference purposes, single material 3D-PCEs were printed solely using either CNT/PLA or CB/PLA filaments. All the electrodes used throughout the work were printed using the aforementioned parameters. Activation of 3D-PCEs was performed by wet-chemical activation in DMF for 1 h to partially remove the PLA and increase their conductivity [54]. In short, glass vials were filled with DMF, and the 3D-PCEs electrodes were introduced individually in each vial in a standing position. After one hour immersed in the DMF, the solvent was removed, and the electrodes were successively washed three times with abundant water and three times with ethanol followed by an overnight drying process under the air.

2.4. Electrochemical measurements

For electrochemical characterisation of the electrodes, cyclic voltammograms were recorded using a 1.5 mM FcMeOH redox marker solution containing 0.5 M KNO_3 as a supporting electrolyte. CVs were run three times between −0.4 and 1 V at a scan rate of 50 mV s^{-1}. For investigating the electrodes' activity towards the hydrogen evolution reaction (HER), linear sweep voltammograms (LSVs) were recorded in a 1 M H_2SO_4 aqueous solution. A linearly decreasing potential ranging from 0.0 V to −1.4 V was applied to the 3D-printed electrodes, with a scan rate of 5 mV s^{-1}. For sensing approaches, ascorbic acid (AA) was used as a model analyte. Different concentrations of analyte (2.5, 5, 10, 25, 50, 100, and 200 μM) were recorded by differential pulse voltammetry (DPV) using a 0.1 M HNO_3/KNO_3 electrolyte solution (scan rate: 50 mV s^{-1}).

2.5. Statistical analysis

Unless otherwise stated, every electrochemical experiment was carried out three times for each type of electrode. For the calculation of electrochemical parameters and statistical values, the average of the three electrodes was calculated with the corresponding standard deviation expressed as the error of the value. For the data contained in Table 1, one-way ANOVA statistical analyses were carried out using Origin Pro software. For all the analyses carried out, the significance level was set to 0.05.

3. Results and discussion

The materials characterisation of multi-material 3D-printed electrodes was carried out after their fabrication and activation with DMF for 1 h, which allowed to partially remove the PLA from the surface of the printed structures. The morphology of the electrodes was analyzed using SEM (Figure 2). Both reference carbon electrodes (CNT and CB 3D-PCEs) showed their characteristic morphology observed previously after chemical activation [40,41,55]. Entangled carbon nanotubes (1D) (Figure 2(A)) for CNT 3D-PCEs or aggregates of very small nanosphere-shaped carbon particles (3D) (Figure 2(B)) for CB 3D-PCEs are observed and allow to distinguish between both materials easily under the electronic microscope. To better understand the hetero-layered structure of the MM 3D-PCEs, two different SEM images were captured (Figure 2(C–D)), one from the bottom side and one from the top side, as the asymmetric nature of the electrode should render two sides with a very distinct morphology. SEM images of the bottom side of MM 3D-PCE reveal the typical morphology of CNT 3D-PCEs (Figure 2(C)) again. On the other hand, the pictures obtained for the top side (Figure 2(D)) stand out as it combines the presence of both carbon allotropes on the surface, similar to that observed in the 3D-printed electrodes from the commercial hybrid CNT/CB filament [50]. The presence of these CNTs on the top side of the MM-3DPCEs could be explained by the activation procedure with DMF. Upon removal of the outer layers of PLA of the electrode's surface, CNTs are released from the bottom side of the MM-3DPCEs and stay in suspension in the DMF until the solvent is removed, when some of the CNTs transfer and deposit onto the top side of the electrode.

After assessing the morphology of the 3D-PCEs, the physicochemical properties of the different electrodes were studied by XPS, RAMAN spectroscopy, and PXRD, which allowed the differentiation of structural characteristics of the carbon allotropes. XPS was used to analyze the different contributions resulting from the carbon allotropes. In the XPS measurements, the sample is irradiated with X-rays, which leads to the photoemission of electrons with a given kinetic energy recorded in a detector. It should be noted that every element of the periodic table photoemits electrons with characteristic kinetic energy, allowing their identification in the

Table 1. Principal electrochemical parameters calculated from CV data (average values from 3 electrodes).

3D-PCE	I_{pa}/I_{pc}	i_0 (μA)	ΔEp (mV)	k^0 ($cm{\cdot}s^{-1}$)	A (cm^2)	R_{ct} ($k\Omega$)
MM	0.91 (±0.03)	23.5 (±0.5)	258 (±29)	3.95×10^{-4} ($\pm 1.7 \times 10^{-4}$)	0.40 (±0.03)	1.10 (±0.03)
CNT	0.94 (±0.02)	25.1 (±0.5)	320 (±35)	1.7×10^{-4} ($\pm 0.9 \times 10^{-4}$)	0.43 (±0.04)	1.02 (±0.02)
CB	0.88 (±0.03)	19.5 (±0.9)	204 (±10)	7.77×10^{-4} ($\pm 0.9 \times 10^{-4}$)	0.45 (±0.03)	1.32 (±0.06)

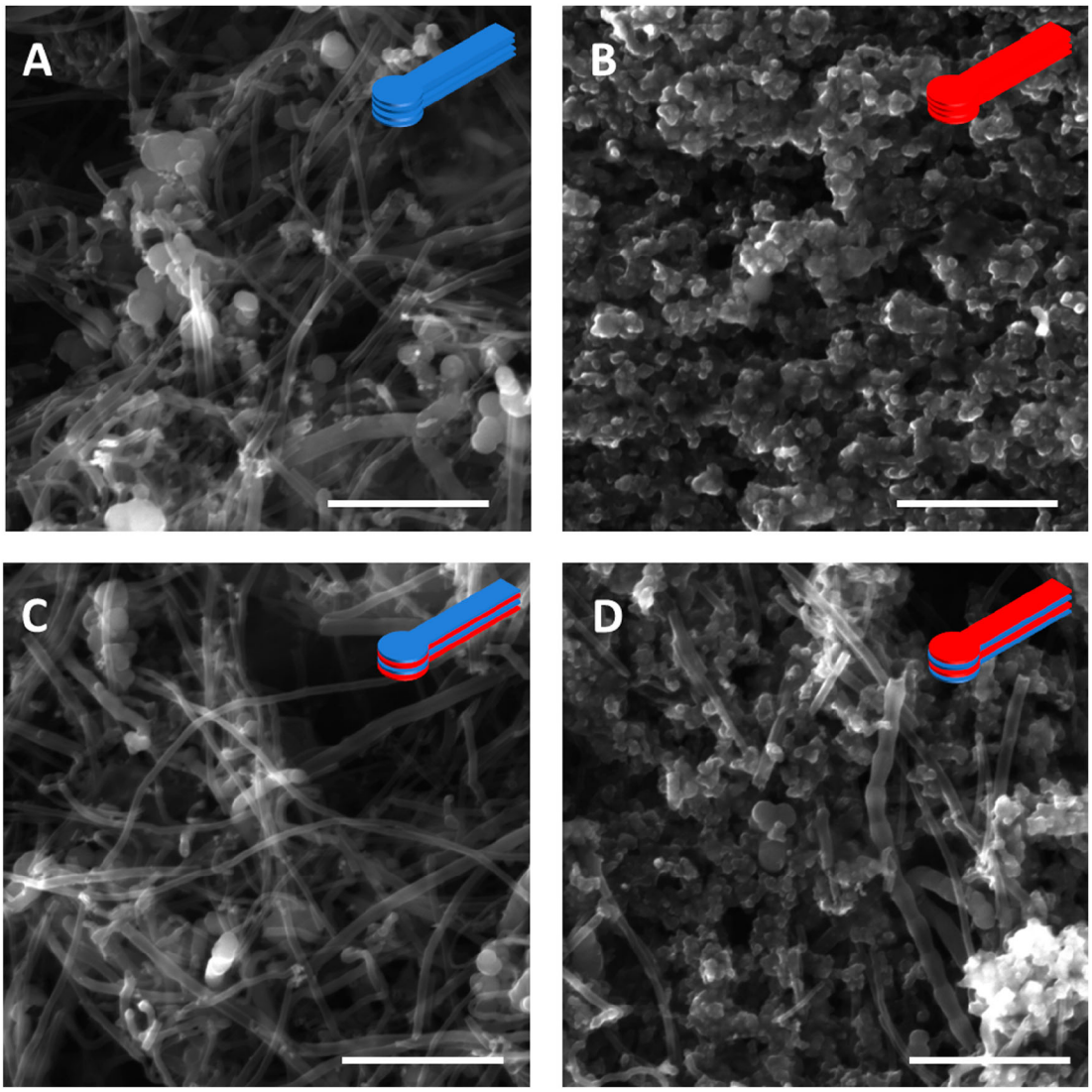

Figure 2. SEM images of DMF-activated CNT 3D-PCE (A), CB 3D-PCE (B), MM 3D-PCE bottom side (C), MM 3D-PCE top side (D). Scale bars: 2 μm.

sample. Thus, the C 1s core level signal detected for CNT and CB 3D-PCEs was deconvoluted into different components that have been assigned to C 1s (sp^2), C 1s (sp^3), C 1s (C–O), C 1s (C = O), and C 1s (O = C–O) from lower to higher binding energy and are in good agreement with previous findings for these 3D-PCEs (Figure 3(A–B)) [55]. The latter three and the sp^3 components are usually associated with the PLA matrix, while the sp^2 component corresponds to the C = C bonds present in the graphitic carbon [41,56]. In addition, the presence of C = O and C–O groups can also be associated with the oxidised form of graphitic carbon, especially in the case of the carbon black filament, and this oxidation has been demonstrated to have important effects in the roughness and different electrochemical parameters [57–59]. Furthermore, the significant C–O peak in the C1s spectrum of CB 3D-PCEs (shown in Figure 3(B)) suggests the presence of a substantial amount of PLA that was not eliminated during DMF activation [60]. Thus, the bottom side of the MM-3DPCEs gave rise to very similar C 1s contributions to those observed for CNT 3D-PCEs, as expected, due to their similar composition. When compared with the pure CB 3D-PCE, the top side of the MM 3D-PCE showed a decreased contribution from C 1s (C–O) and C 1s (C = O) with respect to the C 1s (sp^2) and C 1s (sp^3) peaks, whose origin is associated with the deposition of CNTs on the top side of the electrode (Figures 3(C–D)). XPS was additionally employed to evaluate the presence of metal impurities in all the electrodes. Metallic impurities are common metallic contamination is common in CNT filaments, and the origin of the metals can be found in

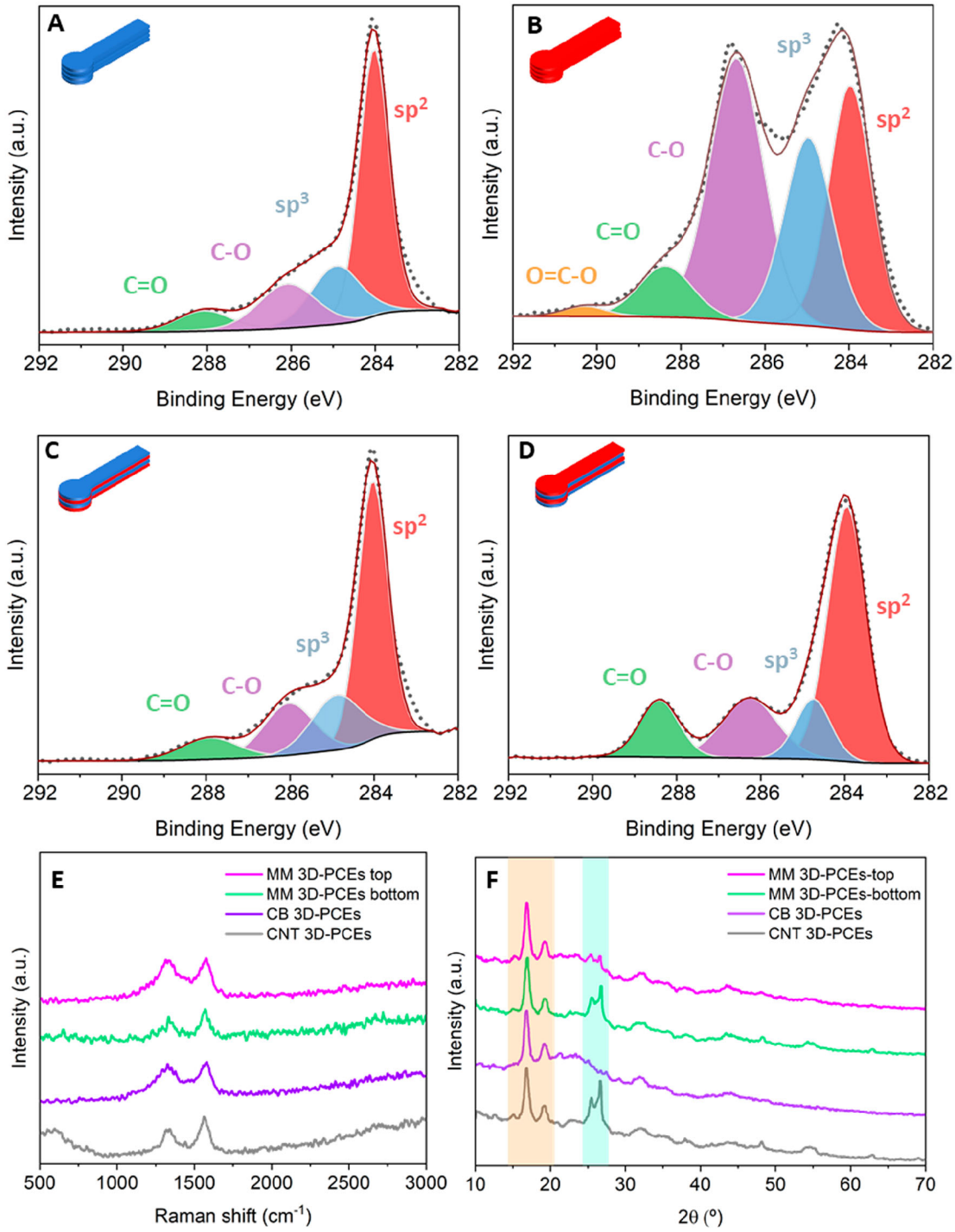

Figure 3. XPS analysis of CNT 3D-PCE. (A) CB 3D-PCE. (B) MM 3D-PCE bottom side. (C) MM 3D-PCE top side; PXRD of all the electrodes. (E) and Raman spectroscopy of all the electrodes (F).

the experimental preparation of the nanotubes [17,61]. On the other hand CB filaments have not been widely studied and the presence of impurities is uncertain. Thus, wide spectra were collected for all the electrodes (Figure S1) corroborating the presence of Ti (0.2% at.) and Fe (0.06% at.) impurities on CNT 3D-PCEs and the bottom side of MM 3D-PCEs. Contrarily, metal impurities were not detected either on CB 3D-PCEs or the top side of MM 3D-PCEs. To get more insight into the nature of the carbon present in all the electrodes, Raman spectroscopy was employed as an important technique. In the Raman technique, the sample is irradiated with

light of a fixed monochromatic wavelength. Following, the interaction of the light with the bonds of the chemical species present in the sample provokes a shift of the monochromatic light towards higher or lower wavenumbers through scattering and is registered in the detector. The Raman scattering allows the assessment of the D and G bands ratio, which is commonly used as a metric to characterise the density of defects in the carbon allotropes [62]. In this regard, both bands were found in the Raman spectra acquired for pure material CNT and CB 3D-PCEs around 1300 and 1600 cm^{-1}, respectively. The spectra for both electrodes show marked differences between them with calculated I_D/I_G band ratios of 0.69 and 0.94, respectively (Figure 3(E)), allowing us to conclude that there is a higher degree of disorder in the carbon particles found in CB 3D-PCEs compared to the nanotubes that comprise CNTs-based electrodes [63]. The spectrum collected for the bottom side of MM 3D-PCEs reveals, again, an important similarity to that recorded for CNT 3D-PCEs, with a calculated I_D/I_G band ratio of 0.73. As expected, the same spectrum measured for the top side of MM 3D-PCEs gives rise to a calculated I_D/I_G band ratio of 0.95, corroborating the strong presence of highly disordered CB black particles.

To conclude the physicochemical characterisation, PXRD was used as a powerful technique to analyse the structure of the carbon species present on the surface of the carbon electrodes. In this technique, X-rays are focused on the sample with the constant movement of the generator and or detector theta angles with respect to the sample, and the diffracted X-rays by the sample are collected in the detector, allowing to obtain diffraction patterns characteristic of each sample, which further allow obtaining atomic and plane positions. Scans run for all 3D-PCEs (Figure 3(F)) showed two main peaks at 2θ of 17 and 19.3° which, according to previous reports, arise from the crystalline PLA polymer present in the electrode [64]. When CNT and CB 3D-PCEs diffraction patterns are compared at higher 2θ values, two important diffraction peaks can be found at 2θ 25.3 and 26.7° for CNT 3D-PCEs, but not for CB 3D-PCEs. These peaks correspond to the interlayer spacing between layers of CNTs and are closely related to the diameter of the CNTs, which further corroborates the high dispersity of CNTs in our electrodes [65,66]. The bottom side of the MM 3D-PCEs inherits the diffraction pattern observed for CNT 3D-PCEs, whilst the top side diffraction pattern shares an important similarity with the diffraction pattern observed for CB 3D-PCEs with the additional contribution of the CNTs deposited on the top layer during the activation procedure (see above). Finally, the surface conductivity of all the electrodes was determined by using a conventional 2-probe system. By measuring the surface resistance between two points separated by 1 cm in 4 different electrodes of each type, we obtained the conductivity of the surface of the 3D-PCEs. Thus, CNT and CB 3D-PCEs show conductivities of 44.0 ± 0.4 and 86.8 ± 0.8 mS/m, respectively. MM 3D-PCEs' bottom and top sides had 35.8 ± 0.3 and 86.6 ± 3.1 S/m, respectively. These results further confirm the asymmetric conductivity of the electrodes MM 3D-PCEs, which matches the physicochemical properties characterised above.

After assessing the physicochemical characteristics of the 3D-PCEs, their electrochemical properties were evaluated. We focused on three important reactions: outer sphere heterogeneous electron transfer rate (using ferrocene methanol, FcMeOH), adsorption/desorption-driven hydrogen evolution, and oxidation of an important biomolecule. We first studied the heterogeneous electron transfer rate using cyclic voltammetry. Before getting into the analysis of the electrochemical data, it should be pointed out that the different filaments employed in this work present different carbon contents (e.g. CNT filament is advertised by the manufacturer to contain less than 20% carbon, while CB filament is 21.4%). To avoid any misleading conclusion as a consequence of the difference in carbon content and to add cost-efficiency dimensionality, the CV data presented below has also been normalised per gram of carbon and can be found in the supporting information (Figures S2 and S3 and Table S1). In addition, the prototypical $Fe(CN)_6^{4-}$/ $Fe(CN)_6^{3-}$ redox marker was also tested (Figure S4), delivering suboptimum results, as has been observed in these 3D-printed carbon electrodes previously [67,68]. Unless otherwise stated, the data presented for MM 3D-PCEs always corresponds to the electrode with both faces exposed to the electrolyte.

Cyclic voltammograms of all the 3D-PCEs (Figure 4(A–C)) show well-defined oxidation and reduction peaks for the FcMeOH redox marker. In terms of width, CNT 3D-PCEs show wider oxidation and reduction peaks, while both MM and CB 3D-PCEs presented narrower peaks. Table 1 shows the most relevant parameters calculated from CV data for the different 3D-PCEs (information on the calculations can be found on the SI). The calculated anodic-to-cathodic peak current ratios (I_{pa}/I_{pc}) remain below 1 in all cases. In addition, these peak current ratios make it clear that the reversibility of oxidation or reduction reactions is higher on the surface of the CNT 3D-PCEs followed closely by MM 3D-PCEs and finally by CB 3D-PCEs. In this line, the highest exchange current intensity, i_0, calculated by the Tafel extrapolation of scans registered at 5 mV s^{-1} (Figure S5), is also displayed by the CNT 3D-PCEs followed by MM and CB

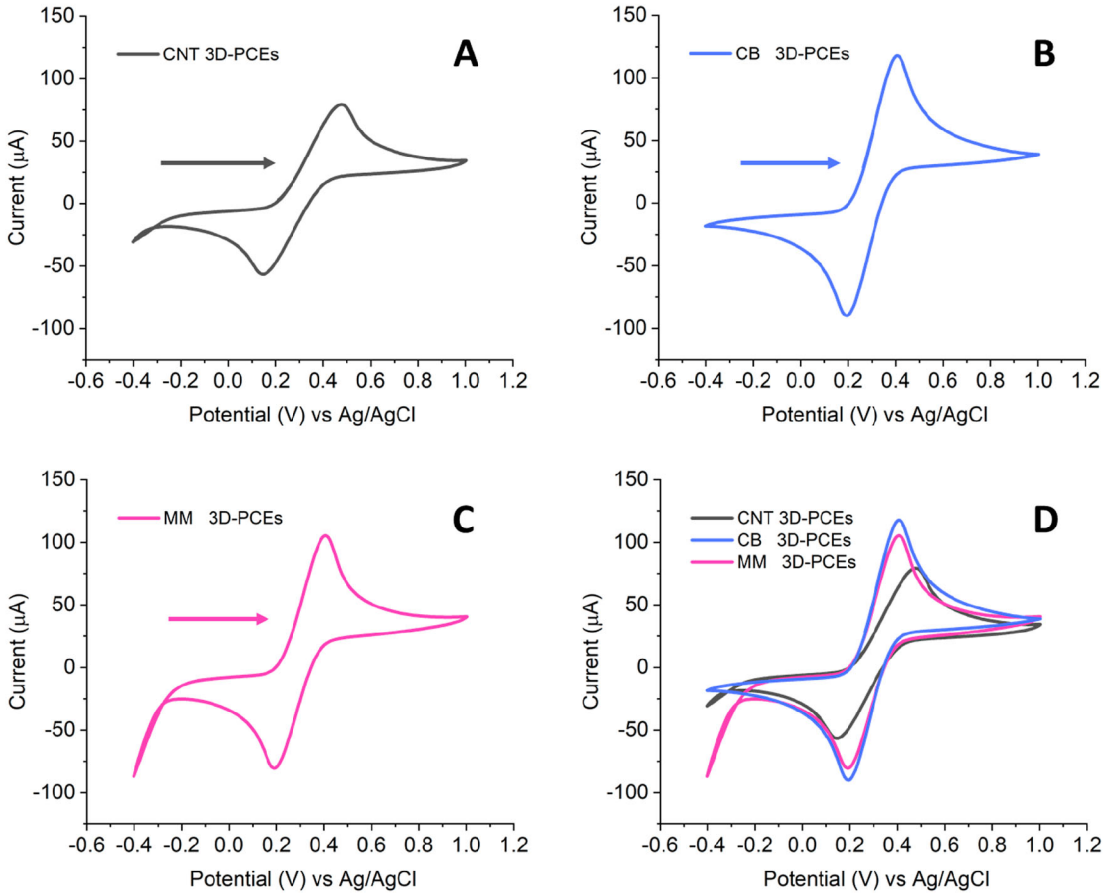

Figure 4. (A–C) Cyclic voltammograms (CVs) of CNT 3D-PCEs (A), CB 3D-PCEs (B), and MM 3D-PCEs (C) and comparison of the CV of the different 3D-PCEs (same colour scheme) (D). $n = 3$ electrodes of each kind were investigated. CVs were recorded in 1.5 mM FcMeOH using a scan rate of 50 mV s^{-1}. The arrow represents the initial scan direction.

3D-PCEs, which have very similar calculated values. In turn, this higher exchange current intensity leads to a smaller charge transfer resistance for the CNT 3D-PCEs compared to the other two.

Contrarily, peak-to-peak separation measurements (ΔE) reveal smaller separations for CB and MM 3D-PCEs compared to the larger separation observed in CNT 3D-PCEs. Furthermore, we calculated the electron transfer rate constant, k^0. The obtained values are supported by the literature data. It was reported that the heterogeneous electron transfer (HET) rates between the electrode surface and a redox marker such as the electrolyte $Fe[(CN)_6]^{4-/3-}$ varied depending on the carbon allotrope used to carry out the electrochemical experiments owing to their structure, hybridisation, and surface area [43]. Therefore, 1D CNTs with their nanometre range diameter provide a high surface area to volume ratio, which makes the material ideal for sensing applications. However, the HET of CNTs is slower than that observed for pyrolytic graphite species and amorphous carbon black, which usually show higher carrier mobility [69–71]. Thus, CNT 3D-PCEs show lower k^0 values than CB 3D-PCEs, as it would be expected. Moreover, the MM 3D-PCEs show faster HET than CNT 3D-PCEs and slower HET than CB 3D-PCEs, showing a closer behaviour to the latter with high HET while only exposing one face of each carbon species. The electroactive area (A) was calculated from CV data using the modified Randles-Sevčik equation (more information in the SI): [72]

$$Ip = (2.69 \times 10^5) n^{3/2} (D \cdot v)^{1/2} A \cdot C$$

In this equation, 'n' is the number of electrons involved in the process (1 electron for the reduction/oxidation of ferrocenemethanol), 'v' is the scan speed, 'C' is the concentration of the electroactive species (1.5 mM), and 'D' the diffusion coefficient (6.3E-6 cm^2 s^{-1}). The calculated electroactive areas from the Ip vs $v^{1/2}$ plot (Figure S4) were in good agreement with the calculated geometrical area for all the electrodes (0.57 cm^2), presenting negative deviations. Such deviations have been observed before and can be related to the

presence of residual superficial PLA filler left after the chemical activation or to the chosen printing parameters, which have been studied, revealing important effects in the calculation of the electroactive area [73]. In short, these results suggest that CB 3D-PCEs allow for the fastest electron transfer rate, followed by MM and CNT 3D-PCEs while showing an opposite tendency for the reversibility of the redox process on their surface [74]. Importantly, one-way ANOVA statistical analysis performed on the different calculated parameters revealed some relevant information. For all the parameters calculated from the recorded current in each of the electrodes (i_0, R_{ct}, and A), the statistical analysis reveals no significant differences between types of electrodes, always giving rise to F values between 0.01 and 0.09. On the other hand, the parameters calculated from data recorded from the potential (ΔE, K^0) showed significant differences between all the electrodes with F values always beyond 5.

All in all, it may seem that the electrochemical data analysis should be complete at this point. Nonetheless, a closer look at the CV plots reveals some unexpected features that might go unnoticed if the data is analyzed just from a mathematical point of view. Thus, the focus should now be on the lower potential region, where the water splitting occurs. On the one hand, when CNT 3D-PCEs (Figure 4(A)) are cycled from −0.3 to −0.4 V a current decrease can be observed, typically associated with the water splitting process due to the inherent impurities of the carbon filament [17]. On the other hand, this current decrease is not observed for CB 3D-PCEs (Figure 4(B)). Curiously, and contrarily to the CB-3DPCEs, in the same region, MM 3D-PCEs show a sharper current decrease to that observed in CNT 3D-PCEs (Figure 4(C)**)**, reaching lower current values and demonstrating a higher activity towards the water splitting. For the sake of comparison, all the CVs have been plotted in Figure 4(D), which shows that while CB 3D-PCEs do not show a current decrease, in the same region there is a current decrease for CNT and MM 3D-PCEs, with the latter affording lower intensity values. This behaviour for the MM 3D-PCEs is unexpected, as the water splitting phenomenon in carbon 3D-printed electrodes, as mentioned above, has been associated with metallic impurities. Thus, the higher activity towards the water splitting could be explained by the increased electroactive area of MM-3DPCEs compared to CNT 3D-PCEs, since CNT 3D-PCEs should inherently expose more impurities to the electrolyte than MM 3D-PCEs (2 pure faces of CNT vs 1 CNT face and 1 CB face with CNTs on top). In this regard, the porous nature of the bottom CNT layer of the MM 3D-PCEs might allow the partial diffusion of the electrolyte into the inner layers of the electrode (2nd layer being CB-based), therefore allowing the MM 3D-PCEs to reach higher currents and improved electrochemical response. This phenomenon of diffusion of the electrolyte into the inner layers of the MM-3DPCE is confirmed by the asymmetric measurements performed covering one side of the electrode at a time and measuring the CV (Figure S6). The CVs obtained for each side of the electrode do not reveal a big difference between both sides, mostly showing very similar behaviour to that of the CB 3D-PCEs. In this sense, it could be concluded that the role of the CNT side in the MM 3D-PCEs is that of providing metallic impurities, enhancing the activity towards catalytic reactions, while the CB side provides the compact packing of graphitic carbon particles that give rise to a significant increase in the measured currents.

In light of these results, HER by means of LSV was studied on all the electrodes to determine if this improved performance for water splitting showed by MM 3D-PCEs can be observed when the HER is studied.

3.1. Hydrogen evolution reaction

HER is nowadays one of the most investigated electrochemical reactions for energy conversion due to the ongoing energetic crisis and is usually employed as a benchmark to determine the electrocatalytic performance of modified electrodes [75]. The linear sweep voltammetry studies carried out herein reveal (Figure 5) a similar trend to that already observed for the small water splitting observed during the CV measurements of the redox marker. In the low potential region (from

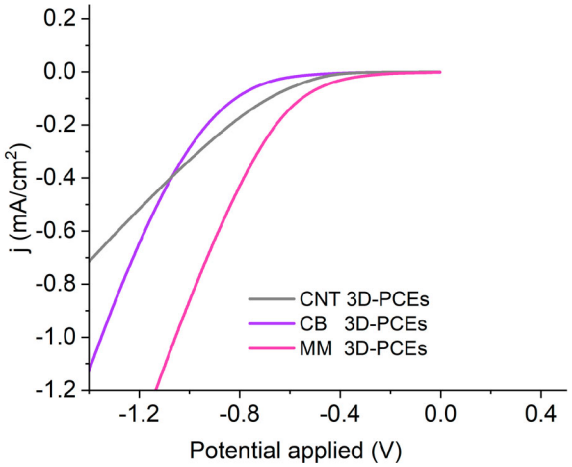

Figure 5. LSV measurements for the HER of MM (pink), CB (purple), and CNT (grey) 3D-PCEs. Conditions: electrolyte, H_2SO_4 (1 M); scan rate, 5mV·s^{-1}. $n = 3$ electrodes of each kind were investigated (the best result is plotted for each type of electrode).

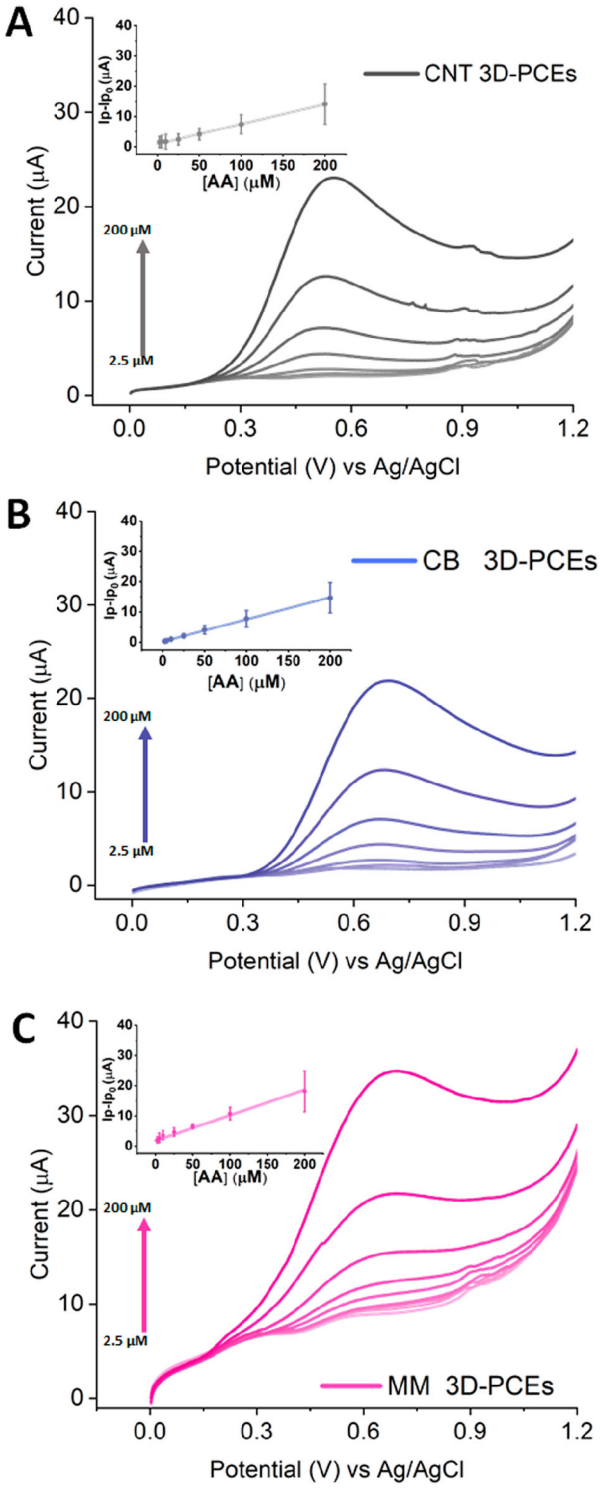

Figure 6. DPV measurements performed for the determination of AA on MM (pink), CB (purple), and CNT (grey) 3D-PCEs. Experiments were carried out in a 0.1 M HNO_3/KNO_3 electrolyte (scan rate: 50 mV·s^{-1}). $n = 3$ electrodes of each kind were investigated.

–0.1 to –0.4 V), CNT and CB 3D-PCEs show linearly decreasing currents with values close to 0 mA, while, in the same region, slightly more negative currents are already recorded for MM 3D-PCEs. Additionally, MM 3D-PCEs are the first electrodes to show a change in slope for the decreasing current at –0.21 V, therefore abandoning the linearity of the current decrease, while CNT and CB 3D-PCEs show their respective change in slope of the recorded current at –0.39 V and –0.51 V. Importantly, although CB 3D-PCEs' current decrease remains linear until lower potentials compared to CNT 3D-PCEs, its slope is much steeper, which leads to the crossing of the currents recorded for both pure material electrodes at –1.07 V in the plot, leading to the final higher activity displayed by CB 3D-PCEs. On the other end, MM 3D-PCEs show a much steeper slope, compared to the other two, demonstrating its higher efficiency for the HER at all times. Translated to overpotential terms, at a current density of –1 mA·cm^{-2}, MM 3D-PCEs display the lowest overpotential of –1.05 V, followed by CB 3D PCEs with –1.35 V and CNT 3D-PCEs, which do not reach those low current density values. In the end, MM 3D-PCEs reach the lowest currents and the lowest overpotential at –1 mA·cm^{-2} of all the 3D-printed materials, followed by CB and CNT 3D-PCEs, which demonstrates the superiority of MM 3D-PCEs towards the HER compared to the pure material electrodes. The origin of this improved performance is associated with two main factors: first, the carbon black-based top side of the MM-3DPCEs leads to a higher active area compared to CNT 3D-PCEs, which translates into higher currents at lower applied potentials; second, the presence of catalytically active metal impurities on the bottom side of MM 3D-PCEs compared to the non-presence of impurities in CB 3D-PCEs enables them towards HER at lower overpotentials. In short, the heterolayered structure of the MM-3DPCEs integrates the best properties of each of their components, giving rise to improved HER efficiency.

To summarise, these results demonstrate an improved performance of the MM 3D-PCEs compared to pristine materials for HER, which was anticipated by the results obtained in the CV measurements of the redox marker. Nonetheless, and even with these interesting results, it should be pointed out that it is hard to foresee the use of these PLA-based electrodes for HER since the conditions employed for this reaction at an industrial scale (NaOH 9 M, 80°C) would inevitably degrade the PLA matrix and deteriorate the electrodes. In light of this outcome, and in order to find a more suitable application for the electrodes, the capability of the MM 3D-PCEs for the detection of ascorbic acid as an analyte in water was also interrogated.

3.2. Ascorbic acid determination

The use of electrochemical techniques for the detection of analytes in water is an appealing strategy since it

allows for a fast, reliable, and cost-effective determination of impurities usually with low limits of detection [8,50,76]. For this purpose, the ability of the different electrodes to detect AA has been explored by performing a calibration experiment by adding different amounts of AA and recording the signal associated with the oxidation of AA (Figure 6(A–C), more information in the experimental section).

For all the electrodes, the addition of successive aliquots of AA results in an increase in the signal recorded for the oxidation of the AA process (Figure 6(A–C)). In terms of potential, CNT 3D-PCEs require the lowest applied potential (0.55 V) for the oxidation of AA, followed by MM and CB 3D-PCEs, which share very similar oxidation potentials (0.69 and 0.70 V). This fact contrasts heavily with the tendency observed during the CV measurements, where CNT 3D-PCEs showed the highest required potential for the oxidation of the redox marker. It should be noted that residual current is recorded for all the electrodes when no AA is added to the media. To avoid an overestimation of the electrode's sensibility, the background signal 'Ip_0' has not been considered by deducting it from the peak current 'Ip' in all cases. In this way, the signals recorded for all the electrodes become comparable (independently of their composition). In general terms, all the calibration curves (Figure 6(A–C) **insets**) can be fitted linearly with the formula $y = a + bx$, where 'a' and 'b' represent the intercept and the slope of the equation, respectively, while 'y' and 'x' refer to the Ip-Ip_0 (in μA) and the final concentration of AA in the solution (in μM), in respective order. All in all, the calculated equations were $y = 0.064x + 1.109$ for CNT 3D-PCEs, $y = 0.072x + 0.309$ for CB 3D-PCEs, and $y = 0.080x + 2.481$ for MM 3D-PCEs. In all cases, the R^2 obtained for the fitting is equal to or above 0.99, which demonstrates the suitability of all the electrodes for the AA determination in the range of concentrations from 2.5 μM to 200 μM. In terms of performance, the best sensibility is displayed by the MM 3D PCEs with a slope of 0.080 (±0.002) μA μM^{-1}, followed by CB and CNT 3D-PCEs with slopes of 0.072 (±0.001) $\mu A \cdot \mu M^{-1}$ and 0.064 (±0.001) μA μM^{-1}, respectively. Therefore, the current registered for the MM 3D-PCEs is, at least, 1.1 times higher than that recorded at the same AA concentration for the pure material electrodes, demonstrating its superior capabilities for the sensing of the analyte.

4. Conclusions

Herein, heterolayered 3D-printed carbon electrodes (3D-PCEs) consisting of two alternating commercially available CNT/PLA and CB/PLA conductive nanocomposite filaments were fabricated for the first time (MM 3D-PCEs) *via* multi-material 3D printing. After their chemical activation, the morphological characterisation revealed the asymmetric surface with the exposed 1D and 3D nanocarbon allotropes. The electrochemical characterisation demonstrates that MM 3D-PCEs' electrochemical properties are between those of the pure material electrodes, although statistical analysis reveals no significant differences between electrodes. Contrarily, when applications such as hydrogen evolution reaction (HER) or detection of ascorbic acid (AA) are the subject of study, MM 3D-PCEs show an improved performance compared to the electrodes purely built with one single allotrope of carbon. The origin of this improvement has been associated with the heterolayered structure of the electrodes, which enables the presence of metallic impurities in MM 3D-PCEs compared to CB 3D-PCEs; and to the higher active area of MM 3D-PCEs compared to CNT 3D-PCEs. Thus, the multi-material printing strategy followed herein, based on alternating layers of different carbon filaments, allows for easy, fast, and scalable preparation of carbon electrodes with improved performance. At the same time, this strategy lays the foundation for the development of a new generation of heterolayered MM-3DPCEs with different electroactive materials such as 2D materials, an appealing strategy for the preparation of heterolayered structures for supercapacitors, batteries, or bio-sensors.

Acknowledgment

The authors gratefully acknowledge the CzechNanoLab project LM2018110 funded by MEYS CR for the financial support of the measurements/sample fabrication at CEITEC Nano Research Infrastructure. This research was co-funded by the European Union under the REFRESH -Research Excellence For Region Sustainability and High-tech Industries project number CZ.10.03.01/00/22_003/0000048 via the Operational Programme Just Transition.

Disclosure statement

No potential conflict of interest was reported by the author(s).

Funding

The work was supported by ERDF/ESF project TECHSCALE (No. CZ.02.01.01/00/22_008/0004587).

Author contributions

M.P.-C activated the electrodes and recorded SEM images. J.M. and M.S. performed electrochemical measurements. K.G carried out XRD, Raman Spectroscopy and conductivity measurements. S.W. performed electrochemical

measurements and printed the electrodes. M.P.-C and M.P. conceptualised the work. M.P. supervised this work. All authors have contributed to the writing and have given approval to the final version of the manuscript.

References

[1] Chua CK, Leong KF. *3D printing and additive manufacturing: principles and applications: the 5th edition of rapid prototyping: principles and applications*; 2017. 1–426. doi: 10.1142/10200

[2] Tofail SAM, Koumoulos EP, Bandyopadhyay A, et al. Additive manufacturing: scientific and technological challenges, market uptake and opportunities. Mater Today. 2018;21(1):22–37. doi: 10.1016/j.mattod.2017.07.001

[3] Ambrosi A, Pumera M. 3D-Printing technologies for electrochemical applications. Chem Soc Rev. 2016;45(10):2740–2755. doi: 10.1039/C5CS00714C

[4] Shahrubudin N, Lee TC, Ramlan R. An overview on 3D printing technology: technological, materials, and applications. Procedia Manuf. 2019;35:1286–1296. doi: 10.1016/j.promfg.2019.06.089

[5] Stefano JS, Guterres e Silva LR, Rocha RG, et al. New conductive filament ready-to-use for 3D-printing electrochemical (Bio)sensors: towards the detection of SARS-CoV-2. Anal Chim Acta. 2022;1191:339372. doi: 10.1016/j.aca.2021.339372

[6] Muñoz J, Pumera M. 3D-Printed COVID-19 immunosensors with electronic readout. Chem Eng J. 2021;425:131433. doi: 10.1016/j.cej.2021.131433

[7] Redondo E, Pumera M. Fully metallic copper 3D-printed electrodes via sintering for electrocatalytic biosensing. Appl Mater Today. 2021;25:101253. doi: 10.1016/j.apmt.2021.101253

[8] Walters JG, Ahmed S, Terrero Rodríguez IM, et al. Trace analysis of heavy metals (Cd, Pb, Hg) using native and modified 3D printed graphene/poly(lactic acid) composite electrodes (Cd, Pb, Hg) using native and modified 3D printed graphene/poly(lactic acid) composite electrodes. Electroanalysis. 2020;32(4):859–866. doi: 10.1002/elan.201900658

[9] Cardoso RM, Silva PRL, Lima AP, et al. 3D-Printed graphene/polylactic acid electrode for bioanalysis: biosensing of glucose and simultaneous determination of uric acid and nitrite in biological fluids. Sensors Actuators, B Chem. 2020;307:127621. doi: 10.1016/j.snb.2019.127621

[10] Hamzah HH, Keattch O, Yeoman MS, et al. Three-dimensional-printed electrochemical sensor for simultaneous dual monitoring of serotonin overflow and circular muscle contraction. Anal Chem. 2019;91(18):12014–12020. doi: 10.1021/acs.analchem.9b02958

[11] Richter EM, Rocha DP, Cardoso RM, et al. Complete additively manufactured (3D-printed). electrochemical sensing platform. Anal Chem. 2019;91(20):12844–12851. doi: 10.1021/acs.analchem.9b02573

[12] Katic V, Dos Santos PL, Dos Santos MF, et al. 3D printed graphene electrodes modified with prussian blue: emerging electrochemical sensing platform for peroxide detection. ACS Appl Mater Interfaces. 2019;11(38):35068–35078. doi: 10.1021/acsami.9b09305

[13] Manzanares Palenzuela CL, Novotný F, Krupička P, et al. 3D-Printed graphene/polylactic acid electrodes promise high sensitivity in electroanalysis. Anal Chem. 2018;90(9):5753–5757. doi: 10.1021/acs.analchem.8b00083

[14] Jyoti, Redondo E, Alduhaish O, et al. 3D-Printed nanocarbon sensors for the detection of chlorophenols and nitrophenols: towards environmental applications of additive manufacturing. Electrochem Commun. 2021;125:106984. doi: 10.1016/j.elecom.2021.106984

[15] Muñoz J, Redondo E, Pumera M. Versatile design of functional organic–inorganic 3D-printed (Opto) electronic interfaces with custom catalytic activity. 2021;17(41):2103189. doi: 10.1002/smll.202103189

[16] Urbanová V, Plutnar J, Pumera M. Atomic layer deposition of electrocatalytic layer of MoS2 onto metal-based 3D-printed electrode toward tailoring hydrogen evolution efficiency. Appl Mater Today. 2021;24:101131. doi: 10.1016/j.apmt.2021.101131

[17] Browne MP, Urbanova V, Plutnar J, et al. Inherent impurities in 3D-printed electrodes are responsible for catalysis towards water splitting. J Mater Chem A. 2020;8(3):1120–1126. doi: 10.1039/C9TA11949C

[18] Hughes JP, Dos Santos PL, Down MP, et al. Single step additive manufacturing (3D printing) of electrocatalytic anodes and cathodes for efficient water splitting. Sustain Energy Fuels. 2020;4(1):302–311. doi: 10.1039/C9SE00679F

[19] Iffelsberger C, Ng S, Pumera M. Catalyst coating of 3D printed structures via electrochemical deposition: case of the transition metal chalcogenide MoSx for hydrogen evolution reaction. Appl Mater Today. 2020;20:100654. doi: 10.1016/j.apmt.2020.100654

[20] Parra-Cabrera C, Achille C, Kuhn S, et al. 3D printing in chemical engineering and catalytic technology: structured catalysts, mixers and reactors. Chem Soc Rev. 2018;47(1):209–230. doi: 10.1039/C7CS00631D

[21] Frederickson LD, Hausen DM. Infrared spectra-structure correlation study of vanadium-oxygen compounds. Anal Chem. 1963;35(7):818–827. doi: 10.1021/ac60200a018

[22] Ng S, Iffelsberger C, Michalička J, et al. Atomic layer deposition of electrocatalytic insulator Al2O3on three-dimensional printed nanocarbons. ACS Nano. 2021;15(1):686–697. doi: 10.1021/acsnano.0c06961

[23] Wang X, Chen XZ, Alcântara CCJ, et al. MOFBOTS: metal–organic-framework-based biomedical microrobots. Adv Mater. 2019;31(27):1901592. doi: 10.1002/adma.201901592

[24] Terzopoulou A, Wang X, Chen XZ, et al. Biodegradable metal–organic framework-based microrobots (MOFBOTs). Adv Healthc Mater. 2020;9(20):2001031. doi: 10.1002/adhm.202001031

[25] Browne MP, Redondo E, Pumera M. 3D printing for electrochemical energy applications. Chem Rev. 2020;120(5):2783–2810. doi: 10.1021/acs.chemrev.9b00783

[26] Muñoz J, Redondo E, Pumera M. Bistable (supra)molecular switches on 3D-printed responsive interfaces with electrical readout. ACS Appl Mater Interfaces. 2021;13(11):12649–12655. doi: 10.1021/acsami.0c14487

[27] Muñoz J, Palacios-Corella M, Pumera M. Electrically Reading a light-driven molecular switch on 2D-Ti3C2Tx MXene via molecular engineering: towards responsive MXetronics. J Mater Chem A. 2022;10(32):17001–17008. doi: 10.1039/D2TA03349F

[28] Acun A, Zhang L, Bampoulis P, et al. Germanene: the germanium analogue of graphene. J Phys Condens Matter. 2015;27(44):443002. doi: 10.1088/0953-8984/27/44/443002
[29] Maurel A, Courty M, Fleutot B, et al. Highly loaded graphite-polylactic acid composite-based filaments for lithium-Ion battery three-dimensional printing. Chem Mater. 2018;30(21):7484–7493. doi: 10.1021/acs.chemmater.8b02062
[30] Gao W, Pumera M. 3D printed nanocarbon frameworks for Li-Ion battery cathodes. Adv Funct Mater. 2021;31(11):2007285. doi: 10.1002/adfm.202007285
[31] Gao W, Michalička J, Pumera M. Hierarchical atomic layer deposited V2O5 on 3D printed nanocarbon electrodes for high-performance aqueous zinc-ion batteries. 2022;18(1):e2105572. doi: 10.1002/smll.202105572
[32] Palacios-Corella M, Ghosh K, Redondo E, et al. Polyoxometalate-enhanced 3D-printed supercapacitors. ChemSusChem. 2022;15(23):e202201490. doi: 10.1002/cssc.202201490
[33] Omar MH, Razak KA, Ab Wahab MN, et al. Recent progress of conductive 3D-printed electrodes based upon polymers/carbon nanomaterials using a fused deposition modelling (FDM) method as emerging electrochemical sensing devices. RSC Adv. 2021;11(27):16557–16571. doi: 10.1039/D1RA01987B
[34] Honeychurch KC, Rymansaib Z, Iravani P. Anodic stripping voltammetric determination of zinc at a 3-D printed carbon nanofiber–graphite–polystyrene electrode using a carbon pseudo-reference electrode. Sensors Actuators, B Chem. 2018;267:476–482. doi: 10.1016/j.snb.2018.04.054
[35] Iffelsberger C, Jellett CW, Pumera M. 3D printing temperature tailors electrical and electrochemical properties through changing inner distribution of graphite/polymer. 2021;17(24):2101233. doi: 10.1002/smll.202101233
[36] Gonzalez G, Chiappone A, Roppolo I, et al. Development of 3D printable formulations containing CNT with enhanced electrical properties. Polymer (Guildf). 2017;109:246–253. doi: 10.1016/j.polymer.2016.12.051
[37] Vernardou D, Vasilopoulos KC, Kenanakis G. 3D printed graphene-based electrodes with high electrochemical performance. Appl Phys A Mater Sci Process. 2017;123(10):doi: 10.1007/s00339-017-1238-1
[38] Vaněčková E, Bouša M, Nováková Lachmanová Š, et al. 3D printed polylactic acid/carbon black electrodes with nearly ideal electrochemical behaviour. J Electroanal Chem. 2020;857:113745. doi: 10.1016/j.jelechem.2019.113745
[39] Kalinke C, de Oliveira PR, Neumsteir NV, et al. Influence of filament aging and conductive additive in 3D printed sensors. Anal Chim Acta. 2022;1191:339228. doi: 10.1016/j.aca.2021.339228
[40] Vaněčková E, Bouša M, Nováková Lachmanová Š, et al. 3D printed polylactic acid/carbon black electrodes with nearly ideal electrochemical behaviour. J Electroanal Chem. 2020;857:113745. doi: 10.1016/j.jelechem.2019.113745
[41] Kalinke C, Neumsteir NV, Aparecido GDO, et al. Comparison of activation processes for 3D printed PLA-graphene electrodes: electrochemical properties and application for sensing of dopamine. Analyst. 2020;145(4):1207–1218. doi: 10.1039/C9AN01926J
[42] Laurila T, Sainio S, Caro M. Hybrid carbon based nanomaterials for electrochemical detection of biomolecules. Prog Mater Sci. 2017;88:499–594. doi: 10.1016/j.pmatsci.2017.04.012
[43] Villarreal CC, Pham T, Ramnani P, et al. Carbon allotropes as sensors for environmental monitoring. Curr Opin Electrochem. 2017;3(1):106–113. doi: 10.1016/j.coelec.2017.07.004
[44] Baptista FR, Belhout SA, Giordani S, et al. Recent developments in carbon nanomaterial sensors. Chem Soc Rev. 2015;44(13):4433–4453. doi: 10.1039/C4CS00379A
[45] Lopes JMJ, Vignaud D. Molecular beam epitaxy. Mol Beam Ep. 2018: 487–513. doi: 10.1016/B978-0-12-812136-8.00023-2
[46] Jiang JW, Park HS. Mechanical properties of MoS2/graphene heterostructures. Appl Phys Lett. 2014;105(3):033108. doi: 10.1063/1.4891342
[47] Wythers MC. Advances in materials science research. Adv Mater Sci Res. 2011;3:1–338.
[48] Rocha DP, Albuquerque RBA, Oliveira GP, et al. Encyclopedia of sensors and biosensors. Encycl Sensors Biosens. 2023: 73–88. doi: 10.1016/B978-0-12-822548-6.00021-2
[49] Laurila T, Sainio S, Caro M. Hybrid carbon based nanomaterials for electrochemical detection of biomolecules. Prog Mater Sci. 2017;88:499–594. doi: 10.1016/j.pmatsci.2017.04.012
[50] Contreras-Naranjo JE, Perez-Gonzalez VH, Mata-Gómez MA, et al. 3D-printed hybrid-carbon-based electrodes for electroanalytical sensing applications. Electrochem Commun. 2021;130:107098. doi: 10.1016/j.elecom.2021.107098
[51] Li F, Macdonald NP, Guijt RM, et al. Increasing the functionalities of 3D printed microchemical devices by single material, multimaterial, and print-pause-print 3D printing. Lab Chip. 2019;19(1):35–49. doi: 10.1039/C8LC00826D
[52] Guo Y, Liu P, Jiang P, et al. A flow-rate-controlled double-nozzles approach for electrochemical additive manufacturing. Virtual Phys Prototyp. 2022;17(1):52–68. doi: 10.1080/17452759.2021.1989751
[53] Zheng H, Lu X, Jiang P, et al. Numerical simulation of 3D double-nozzles printing by considering a stabilized localized radial basis function collocation method. Addit Manuf. 2022;58:103040. doi: 10.1016/J.ADDMA.2022.103040
[54] Gusmão R, Browne MP, Sofer Z, et al. The capacitance and electron transfer of 3D-printed graphene electrodes are dramatically influenced by the type of solvent used for pre-treatment. Electrochem Commun. 2019;102:83–88. doi: 10.1016/j.elecom.2019.04.004
[55] Browne MP, Novotný F, Sofer Z, et al. 3D printed graphene electrodes' electrochemical activation. ACS Appl Mater Interfaces. 2018;10(46):40294–40301. doi: 10.1021/acsami.8b14701
[56] Redondo E, Ng S, Muñoz J, et al. Tailoring capacitance of 3D-printed graphene electrodes by carbonisation temperature. Nanoscale. 2020;12(38):19673–19680. doi: 10.1039/D0NR04864J
[57] Amorim PHO, Oliveira FQ, dos Santos HC, et al. Smart innovation, systems and technologies. Smart Innov Syst

Technol. 2022;255:249–258. doi: 10.1007/978-981-16-4884-7_20
[58] Rocha Á, Paredes-Calderón M, Guarda T. Developments and advances in defense and security. Proc MICRADS 2020 Conf Proc. 2020;181:556. doi: 10.1007/978-981-16-4884-7
[59] da Silva FD, Rocha RG, Rocha DP, et al. In situ electrochemical exfoliation of embedded graphite to superficial graphene sheets for electroanalytical purposes. Electrochim Acta. 2020;354:136762. doi: 10.1016/j.electacta.2020.136762
[60] Muñoz J, Redondo E, Pumera M. Chiral 3D-printed bioelectrodes. Adv Funct Mater. 2021;31(16):2010608. doi: 10.1002/adfm.202010608
[61] Ghosh K, Ng S, Iffelsberger C, et al. Inherent impurities in graphene/polylactic acid filament strongly influence on the capacitive performance of 3D-printed electrode. Chem - A Eur J. 2020;26(67):15746–15753. doi: 10.1002/chem.202004250
[62] Saito R, Hofmann M, Dresselhaus G, et al. Raman spectroscopy of graphene and carbon nanotubes. Adv Phys. 2011;60(3):413–550. doi: 10.1080/00018732.2011.582251
[63] Foo CY, Lim HN, Mahdi MA, et al. Three-dimensional printed electrode and Its novel applications in electronic devices. Sci Reports. 2018;8(1):1–11. doi: 10.1038/s41598-018-25861-3
[64] Nanaki S, Barmpalexis P, Iatrou A, et al. Risperidone controlled release microspheres based on poly(lactic acid)-poly(propylene adipate) novel polymer blends appropriate for long acting injectable formulations. Pharmaceutics. 2018;10(3):130. doi: 10.3390/pharmaceutics10030130
[65] Singh DK, Iyer PK, Giri PK. Diameter dependence of interwall separation and strain in multiwalled carbon nanotubes probed by x-ray diffraction and Raman scattering studies. Diam Relat Mater. 2010;19(10):1281–1288. doi: 10.1016/j.diamond.2010.06.003
[66] Maniwa Y, Fujiwara R, Kira H, et al. Multiwalled carbon nanotubes grown in hydrogen atmosphere: an x-ray diffraction study. Phys Rev B. 2001;64(7):073105. doi: 10.1103/PhysRevB.64.073105
[67] Glowacki MJ, Cieslik M, Sawczak M, et al. Helium-assisted, helium-assisted, solvent-free electro-activation of 3D printed conductive carbon-polylactide electrodes by pulsed laser ablation. Appl Surf Sci. 2021;556:149788. doi: 10.1016/j.apsusc.2021.149788
[68] dos Santos PL, Katic V, Loureiro HC, et al. Enhanced performance of 3D printed graphene electrodes after electrochemical Pre-treatment: role of exposed graphene sheets. Sensors Actuators B Chem. 2019;281:837–848. doi: 10.1016/j.snb.2018.11.013
[69] Arduini F, Di Giorgio F, Amine A, et al. Electroanalytical characterization of carbon black nanomaterial paste electrode: development of highly sensitive tyrosinase biosensor for catechol detection. Anal Lett. 2010;43(10–11):1688–1702. doi: 10.1080/00032711003653932
[70] Silveri F, Della Pelle F, Scroccarello A, et al. Carbon black functionalized with naturally occurring compounds in water phase for electrochemical sensing of antioxidant compounds. Antioxidants. 2022;11(10):2008. doi: 10.3390/antiox11102008
[71] Deroco PB, Lourencao BC, Fatibello-Filho O. The use of modified electrode with carbon black as sensor to the electrochemical studies and voltammetric determination of pesticide mesotrione. Microchem J. 2017;133:188–194. doi: 10.1016/j.microc.2017.03.024
[72] Laoire CO, Mukerjee S, Abraham KM, et al. Elucidating the mechanism of oxygen reduction for lithium-air battery applications. J Phys Chem C. 2009;113(46):20127–20134. doi: 10.1021/jp908090s
[73] Barbosa JR, Amorim PHO, Mariana MC, et al. Smart innovation, systems and technologies. Smart Innov Syst Technol. 2020;152:425–435. doi: 10.1007/978-981-13-9155-2_34
[74] Heinze J. Cyclic voltammetry—"electrochemical spectroscopy". New analytical methods (25). Chemie Int Ed English. 1984;23(11):831–847. doi: 10.1002/anie.198408313
[75] Akshay Kumar KP, Ghosh K, Alduhaish O, et al. Dip-coating of MXene and transition metal dichalcogenides on 3D-printed nanocarbon electrodes for the hydrogen evolution reaction. Electrochem Commun. 2021;122:106890. doi: 10.1016/j.elecom.2020.106890
[76] Kumar KPA, Ghosh K, Alduhaish O, et al. Metal-plated 3D-printed electrode for electrochemical detection of carbohydrates. Electrochem Commun. 2020;120:106827. doi: 10.1016/j.elecom.2020.106827

9. Engineering 3D-printed carbon structures with atomic layer deposition coatings as photoelectrocatalysts for water splitting

Published paper included in this chapter:

Ng, S.; **Sanna, M.**; Redondo, E.; Pumera, M., Engineering 3D-printed carbon structures with atomic layer deposition coatings as photoelectrocatalysts for water splitting, ***J. Mater. Chem. A***, **2024**,**12**, 396-404.

9.1. Motivation for the study

The primary motivation of this work is optimizing the activation process for 3D-printed carbon electrodes to obtain functional platforms that can be further modified with deposition techniques, such as ALD. However, challenges arise when employing ALD to deposit functional materials onto 3D carbon electrodes due to constraints on reaction temperatures and the chemically inert nature of carbon surfaces. To overcome these limitations, surface treatments or functionalizations are necessary to introduce surface species and enhance nucleation sites for ALD processes. In this study, we address these challenges by presenting a novel method to tune carbon surfaces for ALD processes. We demonstrate the deposition of TiO_2, SiO_2, and $Al2O_3$ coatings on 3D-printed carbon electrodes for light-enhanced HER and OER. Furthermore, we extend this approach to electrodes of various geometries and sizes, showcasing the scalability of 3D-printed carbon electrodes for industrial applications. Our work underscores the versatility of ALD coatings on 3D carbon structures, offering a pathway for design flexibility and scalability across various applications.

9.2. Paper conclusion

A straightforward treatment method was demonstrated using aqueous NaOH to prime the surface of 3D-printed carbon electrodes for subsequent low-temperature ALD processes. Notably, the surface wettability of the carbon electrodes undergoes a significant change following treatment with various solvents. Our study showcases the application of three widely utilized ALD coatings, namely TiO_2, SiO_2, and Al_2O_3, on 3D-printed carbon electrodes for enhancing light-assisted HER and OER activities. Remarkably, all ALD-coated electrodes exhibit enhanced performance under blue light irradiation. Specifically, TiO_2-coated electrodes exhibit the lowest HER overpotentials at -10 mA cm^{-2}, registering 0.60 V (in the dark) and 0.31 V (under irradiation), and OER overpotentials at 10 mA cm^{-2}, with values of 1.86 V (in the dark) and 1.47 V (under irradiation). Furthermore, we have successfully applied ALD TiO_2 coating to 3D electrodes of varying shapes and sizes, including multiple rod structures and 2-inch diameter disks, demonstrating the versatility and scalability of FDM-based printing in 3D design. However, it is worth noting that, similar to other upscaled electrodes, the larger 3D electrodes exhibited a slight degradation in HER performance. Consequently, the engineering and design of efficient electrodes will be imperative for enabling large-scale electrochemical energy conversion in the foreseeable future. Our study presents an enhanced carbon surface conducive to diverse ALD coatings, thereby expanding the functionalities of 3D electrodes with unparalleled flexibility in design and scaling for various catalytic applications and beyond.

9.3. Author contribution

In this work, I contributed to the electrode preparation, post-printing treatment, and to the ALD of the functional oxides. I performed part of the electrochemical measurements and contributed to the data analysis and plotting. I carried out the XRD measurements and contributed to the final version of the manuscript.

Journal of Materials Chemistry A

ROYAL SOCIETY OF CHEMISTRY

PAPER

View Article Online
View Journal | View Issue

Cite this: J. Mater. Chem. A, 2024, 12, 396

Engineering 3D-printed carbon structures with atomic layer deposition coatings as photoelectrocatalysts for water splitting†

Siowwoon Ng, [a] Michela Sanna, [a] Edurne Redondo [a] and Martin Pumera *abcde

Three-dimensional (3D)-printing has evolved as a popular technique for producing customized parts and devices. 3D conductive structures made of metals or carbon-based materials are highly preferable in the field of electrochemistry. Compared to their metal counterparts, 3D carbon structures printed by the filament extrusion technique are readily available to end users, with the advantages of reduced electrode mass and broad compatibility with harsh environments that might be required for electrochemical applications. To elevate the applicability of 3D carbon electrodes in sensing, catalysis, energy storage, *etc.*, surface or chemical modifications and coating of functional layers are essential. Atomic layer deposition (ALD) is an ideal deposition tool for creating coatings on geometrically complicated structures, yet the surface chemistry of the inert 3D carbon electrodes critically affects the initial growth. We performed a straightforward surface treatment, also known as 'activation', to improve the surface wettability and promote the ALD of TiO_2, SiO_2, and Al_2O_3 at low deposition temperatures. We applied the ALD coated electrodes for light-enhanced water splitting hydrogen and oxygen evolution reactions (HER, OER). In addition, we showed that 3D electrodes can be prepared in different geometrical shapes and sizes, as their metal counterparts. This work presents the versatility of ALD coatings on 3D carbon platforms, tunable for many other applications.

Received 27th July 2023
Accepted 21st November 2023

DOI: 10.1039/d3ta04460b

rsc.li/materials-a

Introduction

The rise of additive manufacturing utilizing three-dimensional (3D)-printing technologies is closely associated with the rapid production of functional 3D objects based on individualized designs with minimal waste of materials. In alignment with the direction of Industry 4.0, 3D-printing directly increases the productivity in manufacturing processes, thereby offering an intelligent manufacturing solution across the vast spectrum of materials science and engineering.[1] In parallel, it is highly flexible to upscale the printing to the size of buildings[2,3] or miniaturize it to wearable electronic devices.[4] Altogether, 3D-printing offers absolute freedom from design to manufacturing for functional applications.

Transitioning from the traditional machining process to create 3D objects, initially powder bed fusion methods, for instance, electron beam melting (EBM) and selective laser melting (SLM) that fuse fine metal powders with a high-powered electron beam or laser, were employed to develop 3D-printed metal electrodes for electrochemical purposes.[5–8] The metal electrodes serve as a conductive platform for directly synthesizing or depositing active materials for electrochemical conversion and storage applications.[5,7–11] Several studies have utilized the core advantage of 3D-printing to manufacture tens to hundreds of hollow and solid cones on a flat surface[7,8] and centimeter-scaled tubular metal electrodes.[12] In recent years, the fused deposition modeling (FDM) technique has emerged as a captivating alternative to produce carbon-composite electrodes.[13,14] FDM simplifies the printing process with a benchtop printer or hand-held printing pen that is accessible in every research laboratory. Furthermore, the advantages of the FDM-printed carbon electrodes over SLM- or EBM-printed metal electrodes include using an abundant material, reduction in printing cost, decrease in electrode mass, and compatibility with a wide range of chemical or harsh environments.

To expand the functionalities of the as-printed 3D carbon-based electrode, post-treatments[13–17] and post-modifications

[a]Future Energy and Innovation Laboratory, Central European Institute of Technology, Brno University of Technology, Purkyňova 123, 61200 Brno, Czech Republic. E-mail: martin.pumera@ceitec.vutbr.cz

[b]Faculty of Electrical Engineering and Computer Science, VSB – Technical University of Ostrava, 17. Listopadu 2172/15, Ostrava 70800, Czech Republic

[c]Department of Medical Research, China Medical University Hospital, China Medical University, No. 91 Hsueh-Shih Road, Taichung 40402, Taiwan

[d]Department of Chemical and Biomolecular Engineering, Yonsei University, 50 Yonsei-ro, Seodaemun-gu, Seoul 03722, South Korea

[e]Department of Paediatrics and Inherited Metabolic Disorders, First Faculty of Medicine, Charles University, Ke Karlovu 2, 12808 Prague, Czech Republic

† Electronic supplementary information (ESI) available: Additional SEM image, XPS and XRD analyses, and LSV curves for the HER. See DOI: https://doi.org/10.1039/d3ta04460b

are carried out to cater to electrochemical applications such as sensing, energy storage and conversion.[18–25] Atomic layer deposition (ALD) that features conformal coating is presently the most feasible deposition technique to modify objects with geometrically complicated structures such as high porosity foams,[26,27] arrays of spheres,[28,29] tubes and channels.[30–32] Several studies have employed ALD to deposit an active material on 3D-printed metal[10–12] and carbon electrodes.[20–23] However, for 3D carbon electrodes, the restriction on reaction temperatures and chemically inert carbon surface critically influence the nucleation and initial growth of ALD processes,[20,23] posing limitations to depositing functional materials on carbon electrodes. To address these challenges, surface treatment or functionalization to introduce surface species or to increase defect, anchoring, and nucleation sites on the carbon surfaces are viewed as positive solutions.[33]

In this work, we provide a direct solution to tune the carbon surface for ALD processes. We demonstrate three universally used materials, TiO_2, SiO_2, and Al_2O_3,[31,34] coated on 3D-printed carbon electrodes for light-enhanced hydrogen and oxygen evolution reactions (HER, OER). We extend the optimized ALD TiO_2 coating on electrodes with different geometrical shapes and sizes up to a 2 inch-diameter disk (analogous to a small silicon wafer), as illustrated in Scheme 1, in contrast to many flat or simple 3D structures in the past. We show that the 3D-printed carbon electrodes can be potentially upscaled for industrial purposes similar to their metal counterparts. The present work demonstrates the versatility of ALD coatings on 3D carbon host structures in design, up-, and down-scaling to cater to the vast applications.

Experimental

3D-printed carbon electrodes

3D carbon electrodes were designed and printed following the settings in our previous work.[20] In brief, the graphene/polylactic acid (PLA) composite conductive filament (BlackMagic, Graphene Supermarket) was supplied to a Prusa i3 MK3 printer (Prusa Research) to print the 3D electrodes depicted in Scheme 1. The as-printed 3D electrodes underwent the activation steps following the literature with slight modifications as described below.

(i) Electrochemical oxidation + immersion in a reducing agent[15] – 2.5 $V_{Ag/AgCl}$ for 1000 s in phosphate-buffered saline (PBS, pH 7.2), followed by immersion in 1 M sodium borohydride ($NaBH_4$) for 24 h; denoted as $NaBH_4$.

(ii) Immersion in polar aprotic solvent + electrochemical oxidation[16] – immersion in *N*,*N*-dimethylformamide (DMF) for 3 h, followed by 2.5 $V_{Ag/AgCl}$ for 300 s; denoted as DMF.

(iii) Saponification[14] – immersion in 4 M sodium hydroxide (NaOH) for 4 h, where 4 h was the optimized condition and used for further studies; denoted as NaOH.

All electrodes were rinsed thoroughly with water and dried in air.

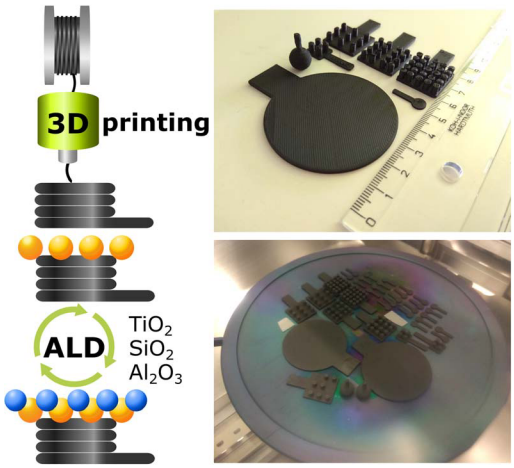

Scheme 1 Schematic representation of the workflow. (Top) Design and 3D-printing of electrodes with various sizes and shapes. (Bottom) ALD of Al_2O_3, SiO_2, or TiO_2 on the 3D electrodes. The electrodes are ready to be transferred to the ALD reactor, and the reflective pieces are silicon wafers for reference purposes.

Atomic layer deposition of TiO_2, Al_2O_3, and SiO_2

After the activation and surface treatment of 3D-printed carbon electrodes, an atomic layer deposition (ALD, Ultratech/CambridgeNanoTech Fiji 200) system was used for material deposition. Tetrakis(dimethylamino)titanium(IV) (TDMATi, Strem Chemicals), trimethylaluminum (TMA, Sigma-Aldrich), and tetrakis(dimethylamido)silane (TDMASi, Sigma-Aldrich) were used as Ti, Al, and Si precursors, respectively. TDMATi was heated to 75 °C to increase the vapor pressure, whereas TMA and TDMASi were not heated. For TiO_2 and Al_2O_3, deionized water (≈18 MΩ) was used as an O_2 precursor, and argon (Air Products, purity 99.999%) served as the carrier gas. The plasma for ALD SiO_2 was obtained by ionizing O_2 gas (Air Products, purity 99.999%). For all substrates temperature was 150 °C. The ALD growth cycle follows the sequence stated below.

(i) TiO_2 – 0.06 s H_2O pulse (Ar 60 sccm), 30 s Ar purge; 0.1 s TDMATi pulse (Ar 200 sccm), 30 s Ar purge.

(ii) Al_2O_3 – 0.06 s H_2O pulse (Ar 30 sccm), 30 s Ar purge; 0.06 s TMA pulse (Ar 100 sccm), 30 s Ar purge.

(iii) SiO_2 – 25 s O_2 purge (50 sccm), 20 s plasma (300 W), 5 s O_2 purge; 0.4 s TDMASi pulse (Ar 100 sccm), 5 s Ar purge.

Materials characterizations

Surface wettability of the activated 3D electrodes was observed using a surface energy evaluation system (See System, Advex Instruments) with proprietary analysis software v7.0. Compositional analyses were carried out by X-ray photoelectron spectroscopy (XPS, Kratos AXIS Supra). The X-ray excitation source was a monochromatic Al Kα (1486.7 eV) with 225 W power. The measured data were analyzed using CasaXPS software. The surface of the electrodes was assessed using a scanning electron microscope (SEM, FEI Verios 460L).

Photo- and electrochemical measurements

All electrochemical experiments were performed using a potentiostat (PGSTAT 204, Metrohm Autolab) operated by NOVA software v2.1 in a three-electrode configuration. The blank or

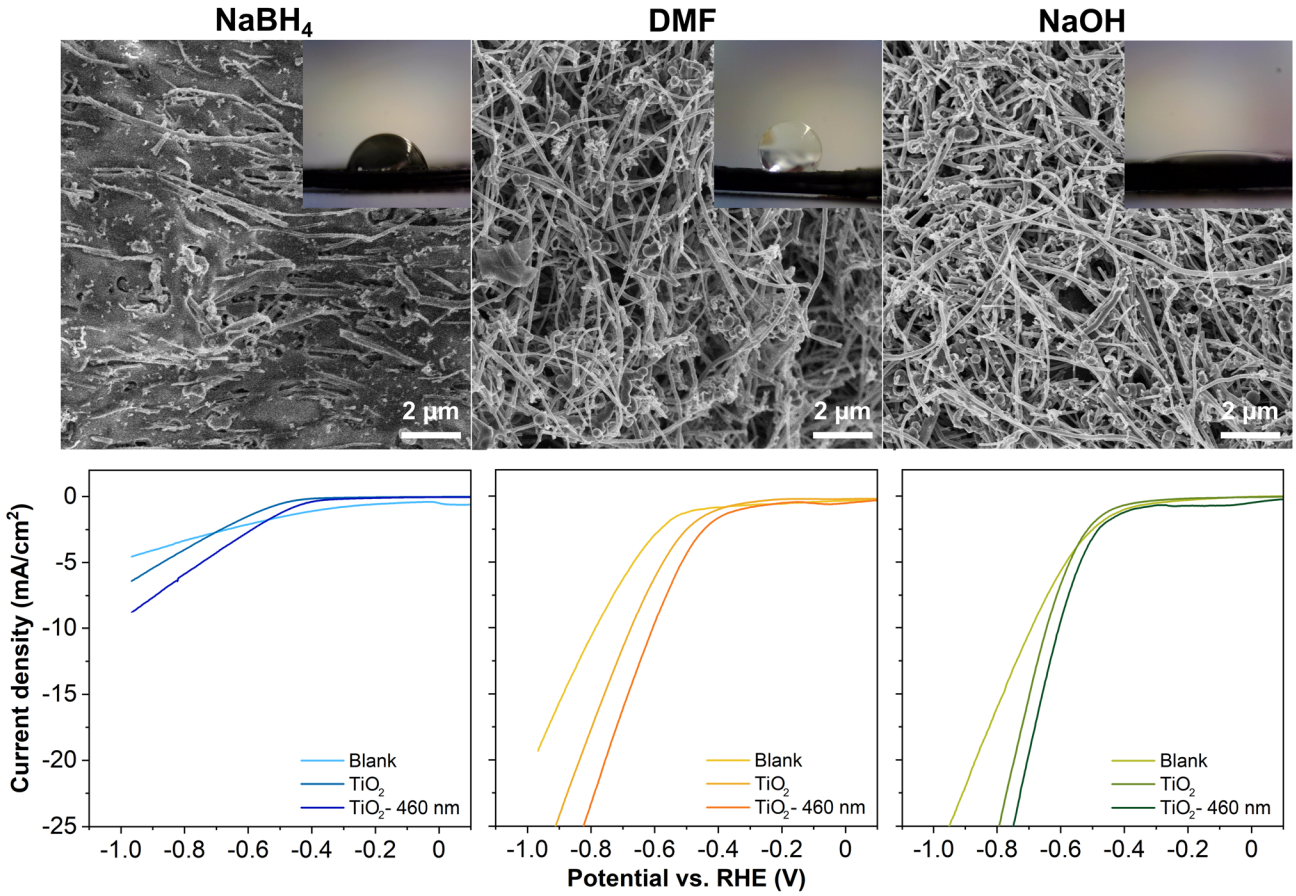

Fig. 1 3D-printed electrodes activated in different solvents, *i.e.*, $NaBH_4$, DMF, and NaOH. (Top) SEM images of the electrodes after the activation process. The insets present the contact angle of water with the surface of the electrodes. (Bottom) LSV curves show the HER of the blank and 500 ALD cycles TiO_2 coated electrodes in 0.5 M H_2SO_4 electrolyte, without and with blue light ($\lambda = 460$ nm) irradiation.

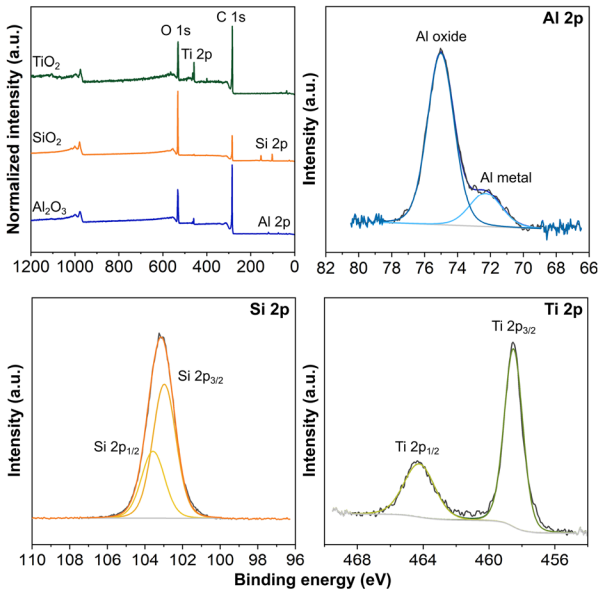

Fig. 2 ALD coated 3D-printed carbon electrodes activated by NaOH. XPS survey spectra and high-resolution Al 2p, Si 2p, and Ti 2p spectra for 50 cycles Al_2O_3, 50 cycles SiO_2, and 1500 cycles TiO_2 coated electrodes, respectively.

ALD TiO_2, Al_2O_3, or SiO_2 coated 3D-printed carbon, Ag/AgCl (1 M KCl), and graphite rod, were used as the working, reference, and counter electrodes, respectively. For both the HER and OER, linear sweep voltammetry (LSV) was carried out with a scan rate of 2 mV s^{-1} in 0.5 M H_2SO_4 and 1 M NaOH electrolyte, respectively, with and without irradiation. Chronoamperometry photoresponse was measured in the same electrolytes by alternating light on and off with applied potential ≈ -0.4 V_{RHE} for the HER and ≈ 1.8 V_{RHE} for the OER. The potential *vs.* Ag/AgCl ($V_{Ag/Ag}$) was converted to the potential *vs.* the reversible hydrogen electrode (V_{RHE}) according to the literature.[35] The blue light irradiation was provided by a customized light-emitting diode setup ($\lambda = 460$ nm, LZ4-40B208, LedEngin Inc.).

Results and discussion

We printed the 3D carbon electrodes with nanocarbon/PLA filament, one of the most used commercial-based conductive filaments. The as-printed 3D electrodes comprised carbon and PLA in a ratio of $\approx 1:9$.[13] We adopted three different activation procedures with minor modifications from the literature to partially remove the insulating PLA, which simultaneously

served as the treatment for the inert carbon surface for ALD purposes. The procedures are (i) electrochemical oxidation, followed by immersion in a reducing solution of $NaBH_4$ (denoted as $NaBH_4$),[15] (ii) a widely reported physical swelling by DMF, followed by electrochemical oxidation (denoted as DMF),[16] and (iii) the less explored saponification by NaOH (as compared to DMF activation, denoted as NaOH).[14]

Fig. 1 presents the surface of the as-activated electrodes observed by SEM. The electrode activated in $NaBH_4$ is less fibrous than the other electrodes, as the fibers are covered by the PLA. For reference, an image of the as-printed, non-activated electrode is given in Fig. S1 in the ESI,† where only several fibers are visible on the surface. Both electrodes activated in DMF and NaOH are similar from the microscopic point, where a substantial amount of PLA was removed, consistent with previous works.[16,23] However, the surface wettability of these electrodes is completely different, evidenced by the contact angle of a water droplet with the electrode surface in the insets in Fig. 1. Specifically, the contact angle with $NaBH_4$, DMF, and NaOH electrodes is 82.5°, 124.5°, and 17.1°, respectively, showing that the NaOH electrode possesses the highest hydrophilicity among the three electrodes. The NaOH treats the electrodes in two ways. For PLA, the hydroxides contribute to the saponification of the PLA as an aliphatic polyester, eventually breaking down the polymer chain into lactate monomers with oxygen-rich functionalities.[14] For carbon, the hydroxides form oxygen-rich functionalities on the carbon surface, altering the wettability of the surface. Transforming the hydrophobic surface to hydrophilic directly improves the accessibility of the electrolyte to the electrode, hence improving the charge transfer,[36–38] and lowering the adhesion forces of the produced bubbles on the electrode surfaces. These characteristics strongly influence the OER, HER and other electrochemical reactions.[37–40]

We carried out thermal ALD of TiO_2 for 500 cycles at 150 °C on the 3D-printed carbon electrodes activated by different solvents. We evaluated the TiO_2 coated electrodes for their HER performance in 0.5 M H_2SO_4 electrolyte. Comparing the LSV curves in Fig. 1, the TiO_2 coated electrodes possess a lower overpotential than the blank counterparts, with further reduced overpotentials by the irradiation of a blue light source. The potential required to drive the HER in descending sequence follows: TiO_2 coated $NaBH_4$, DMF, and NaOH electrodes. The nanometer-scale ALD TiO_2 coatings are not distinguishable from the fibers of a hundred nanometer diameter by SEM imaging (not shown). The XPS analysis confirms that the surface of the electrodes is composed of C, O, and Ti. The survey spectra of all three TiO_2 coated electrodes and atomic concentration of the three elements are given in Fig. S2 in the ESI.† In the high-resolution Ti 2p spectra, the spin–orbit split doublets

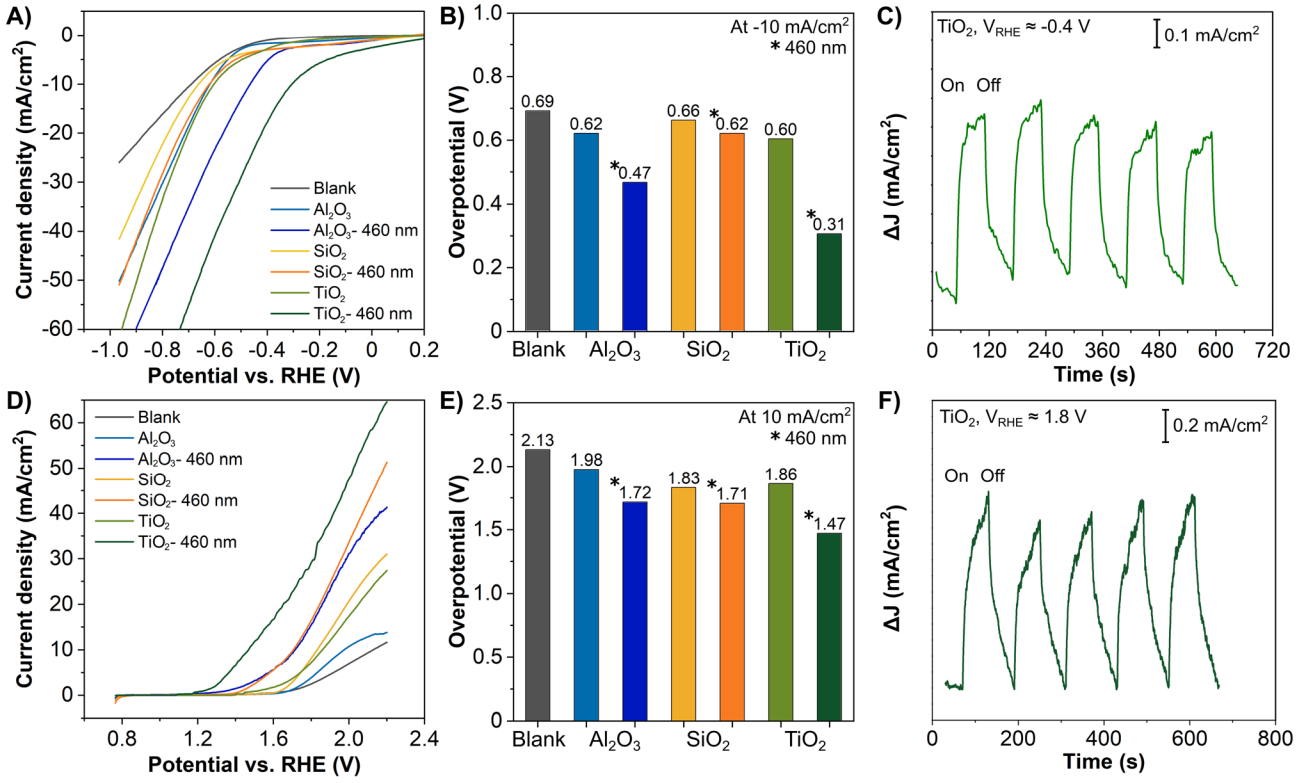

Fig. 3 ALD coated 3D-printed carbon electrodes: 50 cycles of Al_2O_3, 50 cycles of SiO_2, and 1500 cycles of TiO_2. (A and D) LSV of the HER measured in 0.5 M H_2SO_4 and OER measured in 1 M NaOH, with and without irradiation by blue light source ($\lambda = 460$ nm), (B and E) overpotential of the HER (at -10 mA cm^{-2}) and OER (at 10 mA cm^{-2}). Chronoamperometry of the photoresponses of 1500 ALD cycle TiO_2 coated electrodes irradiated by a blue light source with (C) applied potential ≈ -0.4 V_{RHE} in 0.5 M H_2SO_4 and (F) applied potential of ≈ 1.8 V_{RHE} in 1.0 M NaOH.

at ≈458–459 eV and ≈464–465 eV are assigned to Ti $2p_{3/2}$ and Ti $2p_{1/2}$, respectively,[41,42] verifying the formation of Ti^{4+}–O for the ALD TiO_2 coatings. Furthermore, the analysis of the survey spectra shows that the atomic concentrations of Ti in TiO_2 coated $NaBH_4$, DMF, and NaOH electrodes are ≈0.75, 0.50, and 1.85%, respectively, implying more deposition occurred on the surface of the NaOH electrode under the same ALD conditions. Based on the evaluation from different aspects, we conclude that the surface of NaOH electrodes favors the deposition of ALD coatings. In addition, between the DMF and NaOH electrodes, the latter has a higher mechanical stability, which is preferable for device applications.

With the NaOH electrodes, we moved forward with depositing 1500 cycles of TiO_2 and 50 cycles of Al_2O_3 by thermal ALD and 50 cycles of SiO_2 by plasma ALD. The XRD patterns in Fig. S3 in the ESI† present only the diffraction peaks of carbon and PLA,[43,44] with no sign of the peaks associated with the respective coatings. All ALD coatings were amorphous because of the 150 °C substrate temperature, consistent with the literature and our previous work.[22,23,34,45–47] In addition, the thicknesses of coatings in nanometers are rather thin to confirm the crystallinity.[34] We performed XPS analysis to verify the deposition on the 3D-printed carbon electrodes. The survey spectra in Fig. 2 confirm the presence of the expected elements, Al, Si, and Ti in their respective electrodes, along with C from the electrode and O from both the coating and electrode. In addition, Fig. 2 presents the high-resolution Al 2p, Si 2p, and Ti 2p spectra for the electrodes with ALD coatings. The Al 2p spectrum presents a dominant peak at 75.0 eV and a shoulder peak at 72.3 eV, associated with Al–O and Al metal,[46,48] respectively. In addition, the small amount of Al metal indicates the incomplete formation of the Al_2O_3.[22,23] The symmetric peak of Si 2p centered at 103.1 eV confirms the deposition of SiO_2,[49] whereas the spin–orbit split doublet of Ti 2p at 464.2 eV (Ti $2p_{1/2}$) and 458.5 eV (Ti $2p_{3/2}$) verifies the formation of TiO_2.[41,42]

We examined the functionalities of these ALD coated 3D-printed carbon electrodes for the HER. Fig. 3A presents the LSV curves of all Al_2O_3, SiO_2 and TiO_2 coated 3D-printed carbon electrodes for the HER with and without irradiation. For reference, the LSV curves comparing the blank and ALD coated electrodes are included in Fig. S4 in the ESI.† The HER was catalyzed by the ALD coatings and further enhanced by the irradiation, as reflected by the lower potential required to drive the reaction. This is particularly obvious for TiO_2, which has been widely used as a photocatalytic material. For a better overview of the electrodes' performance, we compiled the overpotential at −10 mA cm^{-2}, as a common comparison current density for electrocatalytic reactions in Fig. 3B. For the HER without irradiation, the overpotential for all three coatings is rather similar, between 0.60 and 0.66 V. With irradiation, the SiO_2 coated electrode shows a minor improvement to 0.62 V, followed by Al_2O_3 coating at 0.47 V, and the most significant improvement by TiO_2 coating at 0.31 V. In continuation, we tested the ALD Al_2O_3, SiO_2 and TiO_2 coated 3D-printed carbon electrodes for the OER with and without irradiation. Fig. 3D displays the corresponding LSV curves. Similar to the HER, the OER was catalyzed by the added coatings and improved by irradiation. Fig. 3E summarizes OER overpotentials at 10 mA cm^{-2} for all ALD coated electrodes. Without irradiation, the overpotentials were between 1.83 and 1.98 eV. With irradiation, the overpotentials of Al_2O_3, SiO_2, and TiO_2 were reduced to 1.72, 1.71, and 1.47 V, respectively.

Apparently, TiO_2 coatings as a photoactive material have demonstrated the most substantial light enhancement effect in both the HER and OER. While Al_2O_3 and SiO_2 are classified as insulators based on their electronic band structures, both have shown considerable enhancement. In fact, both insulating materials have served as the primary or co-catalytic material in many photo- and electrocatalytic reactions.[50–54] Although their contribution and exact role remain disputable, the plausible explanations include the photoactivity of defective Al_2O_3 phases,[50] the effective separation of the electron–hole pairs by the (hydroxylated-) Al_2O_3 or SiO_2,[51–53] and the fact that surface states of the insulators (Al_2O_3 and SiO_2) located between the conduction and valence bands act as electron acceptors.[54] Moreover, insulator photocatalysts have become increasingly popular in recent years.[55]

In ALD processes, the growth per cycle (GPC) varies for each material. It is largely influenced by various deposition conditions, including substrate temperature, the precursor (as well as co-reactant) dosing and purging time, or briefly, the interaction between the precursor and the substrate. Therefore, the number of cycles applied for different materials does not correspond to the same thickness. TiO_2 is an example material with much lower GPC as compared to Al_2O_3.[56–59] For example, Tupala *et al.* demonstrated that coating thickness of ≈ 5 nm for Al_2O_3, Ta_2O_5

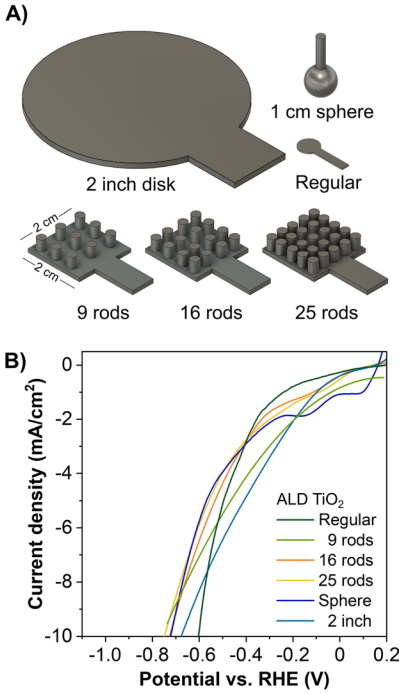

Fig. 4 Scaling-up 3D-printed carbon electrodes. (A) Models of 3D electrodes in different shapes and sizes. (B) LSV of the HER of 1500 ALD cycles TiO_2 coated on different 3D electrodes.

Table 1 Comparison of the HER and OER performance of this work with the literature. Selection criteria: either the catalyst material or 3D electrode is similar to the present work, and the best value(s) from each work is(are) reported[a]

Hydrogen evolution

Catalyst material	3D electrode	Electrolyte	Performance (overpotential *vs.* RHE)	Ref.
Anodized TiO_2	Ti electrode by EBM	0.5 M H_2SO_4	0.092 V at −10 mA cm^{-2}	73
Electrodeposition of Ni	Carbon electrode by FDM	1.0 M NaOH	0.60 V at −50 mA cm^{-2}	24
Electrodeposition of NiPt	Carbon electrode by FDM	1.0 M KOH	0.27 V at −10 mA cm^{-2}	25
ALD MoS_2	Carbon electrode by FDM	0.5 M H_2SO_4	0.49 V at −10 mA cm^{-2} 0.44 V at −10 mA cm^{-2} (irradiation)	20
ALD TiO_2	Carbon electrode by FDM	0.5 M H_2SO_4	0.60 V at −10 mA cm^{-2} 0.31 V at −10 mA cm^{-2} (irradiation)	This work

Oxygen evolution

Catalyst material	3D electrode	Electrolyte	Performance (overpotential *vs.* RHE or current density)	Ref.
Anodized and hydrogenated TiO_2	Ti electrode by SLM	1.0 M NaOH	≈0.3 mA cm^{-2} at 1.2 V (irradiation)	7
ALD TiO_2	Stainless steel electrode by SLM	1.0 M NaOH	≈0.9 mA cm^{-2} at 1.23 V (irradiation)	10
ALD Ir coating within anodized TiO_2	Ti_6Al_4V electrode by selective EBM	1.0 M H_2SO_4 at 60 °C	0.29 V at 10 mA cm^{-2} or 65.2 mA cm^{-2} at 0.5 V	12
Electrodeposition of NiFe-layered double hydroxide	Graphene electrode by DIW	1.0 M KOH	1.50 V at 10 mA cm^{-2}	74
Electrodeposition of Ni–Fe (oxy)hydroxide	Graphene electrode by FDM	0.1 M KOH	0.52 V at 10 mA cm^{-2}	75
Electrodeposition of Ni	Carbon electrode by FDM	1.0 M NaOH	1.80 V at 50 mA cm^{-2}	24
Electrodeposition ReS_2	Carbon electrode by FDM	1.0 M NaOH	≈7 μA cm^{-2} at 1.23 V (irradiation)	18
ALD TiO_2	Carbon electrode by FDM	1.0 M NaOH	1.86 V at 10 mA cm^{-2} 1.47 V at 10 mA cm^{-2} (irradiation)	This work

[a] Abbreviations: EBM = electron-beam melting, SLM = selective laser melting, DIW = direct-ink-writing, FDM = fused deposition modelling.

and TiO_2 required 50, 140, and 376 cycles, respectively.[56] In this work, the three ALD coatings served as the catalytic material. For Al_2O_3 and SiO_2 with an insulating nature, overly thick coatings will hinder the charge transfer to the carbon fibers.[23] On the other hand, TiO_2 is well known as a photoactive material, the thicker coatings hence provide higher photocatalytic and photoelectrochemical activities,[10,60] as long as the 1D carbon fibers are not completely clogged, as supported by the comparison in Fig. S5 in the ESI.†

The photoresponse of the ALD TiO_2 coated 3D-printed carbon electrodes irradiated by a blue light was exemplified by the chronoamperometry measurement in Fig. 3C and F. The measurement followed the electrolyte used in Fig. 3A and D. The applied potentials of ≈−0.4 V_{RHE} and ≈1.8 V_{RHE} were selected for cathodic and anodic region reactions, respectively, according to the LSV measurements, where the HER and OER were already initiated at these potentials. In both regions, the TiO_2 coated 3D electrode showed an immediate response toward irradiation, confirming a photoresponse similar to other TiO_2 photoelectrodes, favorable for solar energy harvesting.[7,10,61,62]

Based on the positive results attained by the 'regular' 3D-printed electrodes, we applied the ALD TiO_2 coatings to 3D electrodes of different dimensions and shapes, as shown in Fig. 4A. We tested these TiO_2 coated electrodes for the HER, where the LSV curves are given in Fig. 4B. Taking into consideration the different geometrical surface areas of the prepared 3D electrodes, at −10 mA cm^{-2}, the overpotential varies in between 0.70 and 0.75 V, with the 'regular' 3D electrode showing the lowest overpotential of 0.60 V. The results show that the electrode performance, in other words, its efficiency, does not increase linearly by scaling up the surface area of an electrode. In most cases, electrodes with surface area ≈ 1 cm^2 or smaller remain the most optimized photo- and electrocatalytic water splitting electrodes.[63–65]

For large scale electrodes, factors such as electrode homogeneity, distribution of current density, ohmic losses, electrolyte conductivity, and pH gradient might be more pronounced and thus influence the electrode performance, of which some of these factors are also supported by modelling and simulation.[63–67] These findings suggest that potential mitigation can be achieved by combining multiple smaller units to minimize the losses described above to achieve a large area device.[68] In other words, the scalability is achieved with the continuous repetition of a base unit to form arrays as a large unit. This approach has been demonstrated by many applications,[69] for example, photovoltaic cells, solar steam generation for CO_2 reduction,[70] fluidic batteries,[71] and aluminum–air microbatteries.[72] These works show that combining small base units to form a large unit retains the advantages such as a large surface-to-volume ratio, enhanced heat and mass transfer, and precise fluid control, all of which are fundamental aspects for solar and electrochemical applications. Overall, the design and geometry of the electrodes are a major challenge in scaling up

photo- and electrocatalytic devices to move from laboratory to industrial scale systems.

To evaluate the performance of the 3D-printed electrodes, we compile Table 1 for the HER and OER performance of other works from the literature. We selected TiO_2 as a catalytic material on 3D electrodes printed by other techniques (electrodes were made from other materials, typically metals) and similar carbon-based electrodes printed by the FDM technique with other catalytic materials. Evidently, our 3D electrodes documented comparable HER and OER overpotentials, showing that the carbon-based electrode is a feasible alternative as a 3D conductive platform.

Conclusions

We demonstrated a simple treatment step in aqueous NaOH to prepare the surface of 3D-printed carbon electrodes for subsequent low-temperature ALD processes. The surface wettability of the carbon electrodes is entirely different after treatment in different solvents. We showed three commonly used ALD coatings, TiO_2, SiO_2, and Al_2O_3 on 3D-printed carbon electrodes for light-enhanced HER and OER. All ALD coated electrodes presented improved performance with blue light irradiation. TiO_2 coated electrodes recorded the lowest HER overpotentials at -10 mA cm^{-2} at 0.60 V (dark) and 0.31 V (irradiation), and OER overpotentials at 10 mA cm^{-2} at 1.86 V (dark) and 1.47 V (irradiation). We applied the ALD TiO_2 coating on 3D electrodes with different shapes and sizes, such as multiple rod structures and 2 inch-diameter disks, to show the freedom of 3D design and scalability by FDM-based printing. Similar to other upscaled electrodes, the HER performance of the larger 3D electrodes suffered a slight degradation. Thus, engineering and designing efficient electrodes will be essential for large scale electrochemical energy conversion in the near future. The present work reports an improved carbon surface ready for diverse ALD coatings to increase the functionalities of 3D electrodes with absolute freedom in design and scaling for catalytic applications and beyond.

Author contributions

SN, MS, and ER prepared the electrodes. SN and MS carried out ALD, surface treatment, and electrochemical experiments. MS conducted XRD measurement. SN performed SEM and XPS measurements, and wrote the manuscript. MP acquired funding and supervised the work. All authors reviewed and edited the manuscript.

Conflicts of interest

There are no conflicts to declare.

Acknowledgements

MP acknowledges the support from ERDF/ESF project TECHSCALE (No. CZ.02.01.01/00/22_008/0004587). MS is thankful for the Brno PhD Talent Scholarship funded by the Brno City Municipality. This research was co-funded by the European Union under the REFRESH-Research Excellence For REgion Sustainability and High-tech Industries project number CZ.10.03.01/00/22_003/0000048 *via* the Operational Programme Just Transition. This work was supported by the Ministry of Health of Czech Republic, grant no. NU21-08-00407. Material deposition and characterizations were carried out at the CEITEC Nano Research Infrastructure supported by CzechNanoLab project LM2023051, MEYS CR. We thank Dr Josef Polčák and Dr Marek Eliáš for technical assistance for XPS and ALD, respectively.

References

1 S. Vaidya, P. Ambad and S. Bhosle, *Procedia Manuf.*, 2018, **20**, 233–238.
2 J. V. Vaghasiya, C. C. Mayorga-Martinez and M. Pumera, *Adv. Funct. Mater.*, 2021, **31**, 2106990.
3 3D-printed Houses, **https://all3dp.com/2/best-companies-building-3d-printed-houses/**, accessed 27.12.2022.
4 Y. Du, R. Wang, M. Zeng, S. Xu, M. Saeidi-Javash, W. Wu and Y. Zhang, *Nano Energy*, 2021, **90**, 106522.
5 Z.-S. Wu, A. Winter, L. Chen, Y. Sun, A. Turchanin, X. Feng and K. Müllen, *Adv. Mater.*, 2012, **24**, 5130–5135.
6 A. Ambrosi and M. Pumera, *Adv. Funct. Mater.*, 2018, **28**, 1700655.
7 C. Y. Lee, A. C. Taylor, S. Beirne and G. G. Wallace, *Adv. Energy Mater.*, 2017, **7**, 1701060.
8 S. Chang, X. Huang, C. Y. A. Ong, L. Zhao, L. Li, X. Wang and J. Ding, *J. Mater. Chem. A*, 2019, **7**, 18338–18347.
9 A. Ambrosi, J. G. S. Moo and M. Pumera, *Adv. Funct. Mater.*, 2016, **26**, 698–703.
10 M. P. Browne, J. Plutnar, A. M. Pourrahimi, Z. Sofer and M. Pumera, *Adv. Energy Mater.*, 2019, **9**, 1900994.
11 V. Urbanová, J. Plutnar and M. Pumera, *Appl. Mater. Today*, 2021, **24**, 101131.
12 A. Hofer, S. Wachter, D. Döhler, A. Laube, B. S. Batalla, Z. Fu, C. Weidlich, T. Struckmann, C. Körner and J. Bachmann, *Electrochim. Acta*, 2022, **417**, 140308.
13 C. W. Foster, M. P. Down, Y. Zhang, X. Ji, S. J. Rowley-Neale, G. C. Smith, P. J. Kelly and C. E. Banks, *Sci. Rep.*, 2017, **7**, 1–11.
14 D. M. Wirth, M. J. Sheaff, J. V. Waldman, M. P. Symcox, H. D. Whitehead, J. D. Sharp, J. R. Doerfler, A. A. Lamar and G. LeBlanc, *Anal. Chem.*, 2019, **91**, 5553–5557.
15 E. Redondo, J. Muñoz and M. Pumera, *Carbon*, 2021, **175**, 413–419.
16 M. P. Browne, F. Novotný, Z. Sofer and M. Pumera, *ACS Appl. Mater. Interfaces*, 2018, **10**, 40294–40301.
17 D. P. Rocha, R. G. Rocha, S. V. F. Castro, M. A. G. Trindade, R. A. A. Munoz, E. M. Richter and L. Angnes, *Electrochem. Sci. Adv.*, 2022, **2**, 202100136.
18 S. Ng, C. Iffelsberger, Z. Sofer and M. Pumera, *Adv. Funct. Mater.*, 2020, **30**, 1910193.
19 K. A. Novčić, C. Iffelsberger, S. Ng and M. Pumera, *Nanoscale*, 2021, **13**, 5324–5332.

20 S. Ng, R. Zazpe, J. Rodriguez-Pereira, J. Michalička, J. M. Macak and M. Pumera, *J. Mater. Chem. A*, 2021, **9**, 11405–11414.
21 W. Gao, J. Michalička and M. Pumera, *Small*, 2022, **18**, 1–13.
22 L. Wang, S. Ng, Jyoti and M. Pumera, *ACS Appl. Nano Mater.*, 2022, **5**, 9719–9727.
23 S. Ng, C. Iffelsberger, J. Michalička and M. Pumera, *ACS Nano*, 2021, **15**, 686–697.
24 J. C. Bui, J. T. Davis and D. V. Esposito, *Sustainable Energy Fuels*, 2020, **4**, 213–225.
25 B. Hüner, N. Demir and M. F. Kaya, *Fuel*, 2023, **331**, 125971.
26 I. Levchuk, C. Guillard, F. Dappozze, S. Parola, D. Leonard and M. Sillanpää, *J. Photochem. Photobiol., A*, 2016, **328**, 16–23.
27 L. Tian, A. Soum-Glaude, F. Volpi, L. Salvo, G. Berthomé, S. Coindeau, A. Mantoux, R. Boichot, S. Lay, V. Brizé, E. Blanquet, G. Giusti and D. Bellet, *J. Vac. Sci. Technol., A*, 2015, **33**, 01A141.
28 J. S. King, E. Graugnard, O. M. Roche, D. N. Sharp, J. Scrimgeour, R. G. Denning, A. J. Turberfield and C. J. Summers, *Adv. Mater.*, 2006, **18**, 1561–1565.
29 J. R. Oh, J. H. Moon, H. K. Park, J. H. Park, H. Chung, J. Jeong, W. Kim and Y. R. Do, *J. Mater. Chem.*, 2010, **20**, 5025–5029.
30 F. Dvorak, R. Zazpe, M. Krbal, H. Sopha, J. Prikryl, S. Ng, L. Hromadko, F. Bures and J. M. Macak, *Appl. Mater. Today*, 2019, **14**, 1–20.
31 A. Spende, N. Sobel, M. Lukas, R. Zierold, J. C. Riedl, L. Gura, I. Schubert, J. M. M. Moreno, K. Nielsch, B. Stühn, C. Hess, C. Trautmann and M. E. Toimil-Molares, *Nanotechnology*, 2015, **26**, 335301.
32 S. Ng, J. Prášek, R. Zazpe, Z. Pytlíček, Z. Spotz, J. R. Pereira, J. Michalička, J. Přikryl, M. Krbal, H. Sopha, J. Hubálek and J. M. Macák, *ACS Appl. Mater. Interfaces*, 2020, **12**, 33386–33396.
33 C. Marichy and N. Pinna, *Coord. Chem. Rev.*, 2013, **257**, 3232–3253.
34 J. Tupala, M. Kemell, E. Härkönen, M. Ritala and M. Leskelä, *Nanotechnology*, 2012, **23**, 125707.
35 R. van de Krol and M. Graetzel, *Photoelectrochemical Hydrogen Production*, Springer US, Boston, MA, 2012, vol. 102.
36 D. Mattia, M. P. Rossi, B. M. Kim, G. Korneva, H. H. Bau and Y. Gogotsi, *J. Phys. Chem. B*, 2006, **110**, 9850–9855.
37 C. Zhang, D. Long, B. Xing, W. Qiao, R. Zhang, L. Zhan, X. Liang and L. Ling, *Electrochem. Commun.*, 2008, **10**, 1809–1811.
38 Z. Zhang, J. Xi, H. Zhou and X. Qiu, *Electrochim. Acta*, 2016, **218**, 15–23.
39 Q. Zhang, T. Li, J. Liang, N. Wang, X. Kong, J. Wang, H. Qian, Y. Zhou, F. Liu, C. Wei, Y. Zhao and X. Zhang, *J. Mater. Chem. A*, 2018, **6**, 7509–7516.
40 C. Meng, B. Wang, Z. Gao, Z. Liu, Q. Zhang and J. Zhai, *Sci. Rep.*, 2017, **7**, 41825.
41 U. Diebold and T. E. Madey, *Surf. Sci. Spectra*, 1996, **4**, 227.
42 A. C. Bronneberg, C. Höhn and R. van de Krol, *J. Phys. Chem. C*, 2017, **121**, 5531–5538.
43 M. Kalani and R. Yunus, *Int. J. Nanomed.*, 2012, 2165–2172.
44 K. Ghosh and M. Pumera, *Nanoscale*, 2021, **13**, 5744–5756.
45 S. Ng, H. Sopha, R. Zazpe, Z. Spotz, V. Bijalwan, F. Dvorak, L. Hromadko, J. Prikryl and J. M. Macak, *Front. Chem.*, 2019, **7**, 38.
46 L. Zheng, X. Cheng and G. Wang, *ACS Appl. Mater. Interfaces*, 2014, **6**, 7014–7019.
47 M. Putkonen, M. Bosund, O. M. E. Ylivaara, R. L. Puurunen, L. Kilpi, H. Ronkainen, S. Sintonen, S. Ali, H. Lipsanen, X. Liu, E. Haimi, S.-P. Hannula, T. Sajavaara, I. Buchanan, E. Karwacki and M. Vähä-Nissi, *Thin Solid Films*, 2014, **558**, 93–98.
48 B. R. Strohmeier, *Surf. Interface Anal.*, 1990, **15**, 51–56.
49 N. Koshizaki, H. Umehara and T. Oyama, *Thin Solid Films*, 1998, **325**, 130–136.
50 F. Li, S. Liu, Y. Xue, X. Wang, Y. Hao, J. Zhao, R. Liu and D. Zhao, *Chem.–Eur. J.*, 2015, **21**, 10149–10159.
51 C.-S. Yang, Y.-J. Wang, M.-S. Shih, Y.-T. Chang and C.-C. Hon, *Appl. Catal., A*, 2009, **364**, 182–190.
52 F. Tzompantzi, Y. Piña, A. Mantilla, O. Aguilar-Martínez, F. Galindo-Hernández, X. Bokhimi and A. Barrera, *Catal. Today*, 2014, **220–222**, 49–55.
53 C. Iffelsberger, D. Rojas and M. Pumera, *J. Phys. Chem. C*, 2022, **126**, 9016–9026.
54 R. Li, X. Wang, S. Jin, X. Zhou, Z. Feng, Z. Li, J. Shi, Q. Zhang and C. Li, *Sci. Rep.*, 2015, **5**, 13475.
55 K. Li, S. Zhang, Q. Tan, X. Wu, Y. Li, Q. Li, J. Fan and K. Lv, *Chem. Eng. J.*, 2021, **426**, 130772.
56 J. Tupala, M. Kemell, E. Härkönen, M. Ritala, M. Leskelä, V. Pore, T. T. Isimjan, A. El Ruby, S. Rohani, J. Tupala, M. Kemell and H. Emma, *Nanotechnology*, 2012, **23**, 125707.
57 A. Szeghalmi, M. Helgert, R. Brunner, F. Heyroth, U. Gösele and M. Knez, *Appl. Opt.*, 2009, **48**, 1727–1732.
58 J. A. Kropp, Y. Cai, Z. Yao, W. Zhu and T. Gougousi, *J. Vac. Sci. Technol., A*, 2018, **36**, 06A101.
59 L.-S. Gao, Q.-Y. Cai, E.-T. Hu, Q.-Y. Zhang, Y.-T. Yang, Y.-B. Xiong, B.-J. Liu, W.-B. Duan, T.-Y. Yu and D.-Q. Liu, *Opt. Express*, 2023, **31**, 13503.
60 H. Sopha, M. Krbal, S. Ng, J. Prikryl, R. Zazpe, F. K. Yam and J. M. Macak, *Appl. Mater. Today*, 2017, **9**, 104–110.
61 S. Ng, F. K. Yam, S. N. Sohimee, K. P. Beh, S. S. Tneh, Y. L. Cheong and Z. Hassan, *Sens. Actuators, A*, 2018, **279**, 263–271.
62 C. Iffelsberger, S. Ng and M. Pumera, *Chem. Eng. J.*, 2022, **446**, 136995.
63 I. Y. Ahmet, Y. Ma, J.-W. W. Jang, T. Henschel, B. Stannowski, T. Lopes, A. Vilanova, A. Mendes, F. F. Abdi and R. van de Krol, *Sustainable Energy Fuels*, 2019, **3**, 2366–2379.
64 S. Dilger, M. Trottmann and S. Pokrant, *ChemSusChem*, 2019, **12**, 1931–1938.
65 H. Lu, V. Andrei, K. J. Jenkinson, A. Regoutz, N. Li, C. E. Creissen, A. E. H. Wheatley, H. Hao, E. Reisner, D. S. Wright and S. D. Pike, *Adv. Mater.*, 2018, **30**, 1804033.
66 S. Haussener, C. Xiang, J. M. Spurgeon, S. Ardo, N. S. Lewis and A. Z. Weber, *Energy Environ. Sci.*, 2012, **5**, 9922.

67 A. Hankin, F. E. Bedoya-Lora, C. K. Ong, J. C. Alexander, F. Petter and G. H. Kelsall, *Energy Environ. Sci.*, 2017, **10**, 346–360.
68 B. Turan, J.-P. Becker, F. Urbain, F. Finger, U. Rau and S. Haas, *Nat. Commun.*, 2016, **7**, 12681.
69 S. K. S. Cheng, T. Li, S. S. Meena, Q. Cao, B. Li, B. K. Kosgei, T. Cheng, P. Luo, Q. Liu, G. Zhu, Q. Liu and R. P. S. Han, *Adv. Energy Sustainability Res.*, 2022, **3**, 2200060.
70 H. Liu, H. Ye, M. Gao, Q. Li, Z. Liu, A. Xie, L. Zhu, G. W. Ho and S. Chen, *Adv. Sci.*, 2021, **8**, 2101232.
71 N. K. Thom, K. Yeung, M. B. Pillion and S. T. Phillips, *Lab Chip*, 2012, **12**, 1768.
72 L.-L. Shen, G.-R. Zhang, M. Biesalski and B. J. M. Etzold, *Lab Chip*, 2019, **19**, 3438–3447.
73 X. Li, Y. Xue, R. Dehoff, C. Tsouris and P. Taboada-Serrano, *Journal of Energy and Power Technology*, 2020, **2**, 1–16.
74 J. Ahn, Y. S. Park, S. Lee, J. Yang, J. Pyo, J. Lee, G. H. Kim, S. M. Choi and S. K. Seol, *Sci. Rep.*, 2022, **12**, 346.
75 P. L. Santos, S. J. Rowley-Neale, A. G. -M. Ferrari, J. A. Bonacin and C. E. Banks, *ChemElectroChem*, 2019, **6**, 5633–5641.

10. Conclusions

In summary, different compounds were investigated as photoelectrocatalysts for HER. Transition-metal selenophosphites crystals, $MnPSe_3$, $FePSe_3$ and $ZnPSe_3$, showed excellent photoelectrocatalytic response during illumination with visible light (660 nm). $ZnPSe_3$ was the one that exhibited the lowest overpotential for HER and the higher response to the light during photocurrent experiments in acidic media. For this reason, among the studied crystals, it is the most promising for the photocatalyzed production of hydrogen.

Moreover, the effect of the fluorination of different MAX, Ta_2AlC, Cr_2AlC, Ti_2AlC, and Ti_3AlC_2, on their structural and morphological properties was evaluated and the phases were then applied as photoelectrocatalysts for hydrogen generation. The morphology of the treated compounds changed as a consequence of the exposure to the fluorine gas, showing partial delamination between the layers and an extent formation of oxyfluoride species on their surface. As an exception, the analysis of F-Cr_2AlC showed a considerable amount of fluorine on the surface without significant change in its morphology. This difference can be related to the fact that Cr_2AlC is reported to be more resistant to oxidation and exfoliation than the other MAX phases in this work. All MAX and F-MAX, showed improved photoelectrocatalytic activity when exposed to the illumination by a 660 nm light source. The more pronounced improvement of the catalytic activity due to illumination was observed for F-Ti_2AlC and F-Ti_3AlC_2, which showed a reduction of the overpotential value of 178 mV and 119 mV respectively. The improved response of the two compounds can be attributed mainly to the presence of the photoactive oxyfluoride ($TiOF_2$) on their surface as a consequence of the fluorination process, as confirmed by the morphological and structural characterization. Cr_2AlC and F-Cr_2AlC presented the lowest overpotential and Tafel slope values in their respective category and, despite the absence of the corresponding oxyfluoride, the former showed better performances

and improved photoelectrocatalytic effect compared to Cr_2AlC. In this case, a better insight into the properties of this compound is necessary to explain the role of fluorine within its structure.

In particular, the photo-activity of MAX phases was an unexpected result, since they are reported to show a metallic behaviour. This fact inspired the last work presented in this thesis, in which three MAX, Nb_2AlC, Ta_2AlC, and Ti_3AlC_2, were studied in detail using theoretical and experimental approaches to investigate the origin of their photoactivity. The theoretical calculations concluded that the metals contribute dominantly to the DOS around the Fermi level, confirming the metallic nature of these compounds, with no band gap in the vicinity of the Fermi level. XPS and EDS analyses detected not only the presence of the respective transition metal oxides but also a relevant amount of Al_2O_3. In contrast to the theoretical calculation, it was experimentally estimated that for Nb_2AlC and Ta_2AlC, there are two fundamental absorptions at 2.2 eV, 3.1 eV, and 2.2 eV, 3.3 eV, respectively. Moreover, the estimated band gap for Ti_3AlC_2 was 2.4 eV. As a confirmation of the presence of photoactive material, all MAX showed an enhanced photocatalytic activity towards HER when exposed to illumination by different light sources. In particular, Nb_2AlC and Ta_2AlC performed better (758 mV and 760 mV of overpotential, respectively) when exposed to UV light, and Ti_3AlC_2 showed the lowest overpotential (680 mV) when exposed to the 460 nm light source, in accordance with the estimated optical band gaps. In general, the formation of oxides on MAX phases has been already reported, since contamination is unavoidable if the material comes in contact with the air or with oxidizing solvents[75,91]. The results obtained in this study showed how these impurities can play a crucial role in photoelectrochemical hydrogen generation, leading to better performances thanks to their intrinsic photoactivity. These findings can open the door for further implementation of MAX phases as photoelectrocatalysts. In addition to the three MAX investigated in this work, more than 150 other MAX phases[92] synthesized to date might observe similar photoactive properties, which are yet to be tested and possibly applied in this field. Even

if the performances obtained are not comparable with other materials, such as MoS_2 and MXene, a better understanding of these compounds and the effect of surface modification processes on their properties can lead to the development of new promising photoelectrocatalysts.

The implementation of the second objective of this thesis resulted in the fabrication of heterolayered 3D-printed carbon electrodes using multi-material 3D printing for the first time. These electrodes consisted of alternating commercially available CNT/PLA and CB/PLA conductive nanocomposite filaments. After chemical activation, morphological analysis revealed an asymmetric surface exposing both 1D and 3D nanocarbon allotropes. Electrochemical tests showed that the electrodes display intermediate properties compared to those made solely of individual carbon allotropes, with no significant differences observed between them statistically. However, in applications such as the HER or the detection of ascorbic acid AA, multimaterial 3D-printed carbon electrodes demonstrated superior performance compared to single carbon allotrope electrodes. This enhancement is attributed to the heterolayered structure, facilitating the presence of metallic impurities and a larger active area. Thus, the multimaterial printing approach offers a convenient, rapid, and scalable method for producing carbon electrodes with improved performance. Additionally, this strategy sets the stage for developing advanced heterolayered 3D-printed electrodes incorporating various electroactive materials, promising applications in supercapacitors, batteries, or biosensors.

Moreover, a simple treatment method was implemented using aqueous NaOH to prepare the surface of 3D-printed carbon electrodes for subsequent ALD processes at low temperatures. Interestingly, the surface properties of the carbon electrodes change significantly after treatment with different solvents. Our research highlights the effectiveness of three common ALD coatings, such as TiO_2, SiO_2, and Al_2O_3, on 3D-printed carbon electrodes, enhancing their light-assisted HER and OER activities. Notably, all ALD-coated electrodes show improved

performance under blue light irradiation. Particularly, TiO_2-coated electrodes demonstrate the lowest overpotentials for HER and OER under both dark and irradiation conditions. Additionally, ALD TiO_2 coating to 3D electrodes of various shapes and sizes was successfully applied, showcasing the adaptability and scalability of FDM-based printing in 3D design. However, larger 3D electrodes experienced a slight degradation in HER performance, highlighting the need for efficient electrode engineering and design for large-scale electrochemical energy conversion. Our study presents an enhanced carbon surface suitable for diverse ALD coatings, expanding the capabilities of 3D electrodes with unmatched design flexibility and scalability for various catalytic applications and beyond.

In conclusion, the content of this thesis will contribute to a better understanding of 2D materials like $MPCh_3$ and their potential application as photoelectrocatalysts capable of absorbing visible light to promote hydrogen production from water-based electrolytes. Moreover, the fundamental study of MAX and the role of impurities and chemical modification on their optical properties open new insights about this class of materials and their possible application in photoelectrochemistry. The combination of this knowledge and the use of 3D-printed conductive platforms discussed in this thesis can lead to the fabrication of performing electrodes that combine the mechanical strength of the 3D electrode and the catalytic properties of functional materials that can be combined with this technology. Further studies in this direction will contribute to the development of photoelectroactive electrodes that can be used under the influence of visible light, guaranteeing solid performance in the field of the photoelectrochemical production of hydrogen from water.

11. References

(1) Novoselov, K. S.; Geim, A. K.; Morozov, S. V.; Jiang, D.; Zhang, Y.; Dubonos, S. V.; Grigorieva, I. V.; Firsov, A. A. Electric Field in Atomically Thin Carbon Films. *Science* **2004**, *306* (5696), 666–669. https://doi.org/10.1126/science.1102896.

(2) Jiao, Y.; Zheng, Y.; Davey, K.; Qiao, S. Z. Activity Origin and Catalyst Design Principles for Electrocatalytic Hydrogen Evolution on Heteroatom-Doped Graphene. *Nat. Energy* **2016**, *1* (10). https://doi.org/10.1038/nenergy.2016.130.

(3) Qu, L.; Liu, Y.; Baek, J. B.; Dai, L. Nitrogen-Doped Graphene as Efficient Metal-Free Electrocatalyst for Oxygen Reduction in Fuel Cells. *ACS Nano* **2010**, *4* (3), 1321–1326. https://doi.org/10.1021/nn901850u.

(4) Zhao, Y.; Zhang, J.; Qu, L. Graphitic Carbon Nitride/Graphene Hybrids as New Active Materials for Energy Conversion and Storage. *ChemNanoMat* **2015**, *1* (5), 298–318. https://doi.org/10.1002/cnma.201500060.

(5) Gong, Y.; Li, M.; Wang, Y. Carbon Nitride in Energy Conversion and Storage: Recent Advances and Future Prospects. *ChemSusChem* **2015**, *8* (6), 931–946. https://doi.org/10.1002/cssc.201403287.

(6) Jaramillo, T. F.; Jørgensen, K. P.; Bonde, J.; Nielsen, J. H.; Horch, S.; Chorkendorff, I. Identification of Active Edge Sites for Electrochemical H_2 Evolution from MoS_2 Nanocatalysts. *Science* **2007**, *317* (5834), 100–102. https://doi.org/10.1126/science.1141483.

(7) Gusmão, R.; Sofer, Z.; Pumera, M. Metal Phosphorous Trichalcogenides ($MPCh_3$): From Synthesis to Contemporary Energy Challenges. *Angew. Chemie - Int. Ed.* **2019**, *58* (28),

9326–9337. https://doi.org/10.1002/anie.201810309.

(8) Yang, F.; Elnabawy, A. O.; Schimmenti, R.; Song, P.; Wang, J.; Peng, Z.; Yao, S.; Deng, R.; Song, S.; Lin, Y.; Mavrikakis, M.; Xu, W. Bismuthene for Highly Efficient Carbon Dioxide Electroreduction Reaction. *Nat. Commun.* **2020**, *11* (1). https://doi.org/10.1038/s41467-020-14914-9.

(9) Dinh, K. N.; Zhang, Y.; Zhu, J.; Sun, W. Phosphorene-Based Electrocatalysts. *Chem. - A Eur. J.* **2020**, *26* (29), 6437–6446. https://doi.org/10.1002/chem.202000211.

(10) Ng, S.; Sturala, J.; Vyskocil, J.; Lazar, P.; Martincova, J.; Plutnar, J.; Pumera, M. Two-Dimensional Functionalized Germananes as Photoelectrocatalysts. *ACS Nano* **2021**, *15* (7), 11681–11693. https://doi.org/10.1021/acsnano.1c02327.

(11) Nicolosi, V.; Chhowalla, M.; Kanatzidis, M. G.; Strano, M. S.; Coleman, J. N. Liquid Exfoliation of Layered Materials. *Science* **2013**, *340* (6139), 72–75. https://doi.org/10.1126/science.1226419.

(12) Mashtalir, O.; Lukatskaya, M. R.; Zhao, M. Q.; Barsoum, M. W.; Gogotsi, Y. Amine-Assisted Delamination of Nb_2C MXene for Li-Ion Energy Storage Devices. *Adv. Mater.* **2015**, *27* (23), 3501–3506. https://doi.org/10.1002/adma.201500604.

(13) Yu, Z.; Peng, J.; Liu, Y.; Liu, W.; Liu, H.; Guo, Y. Amine-Assisted Exfoliation and Electrical Conductivity Modulation toward Few-Layer FePS3 Nanosheets for Efficient Hydrogen Evolution. *J. Mater. Chem. A* **2019**, *7* (23), 13928–13934. https://doi.org/10.1039/c9ta03256h.

(14) Mashtalir, O.; Naguib, M.; Mochalin, V. N.; Dall'Agnese, Y.; Heon, M.; Barsoum, M. W.; Gogotsi, Y. Intercalation and Delamination of Layered Carbides and Carbonitrides. *Nat. Commun.* **2013**, *4*, 1–7. https://doi.org/10.1038/ncomms2664.

(15) Chia, H. L.; Mayorga-Martinez, C. C.; Pumera, M. Doping and Decorating 2D Materials for Biosensing: Benefits and Drawbacks. *Adv. Funct. Mater.* **2021**, *31* (46), 1–31. https://doi.org/10.1002/adfm.202102555.

(16) Wang, X.; Wang, W.; Xu, D.; Liu, Y.; Lai, W.; Liu, X. Activation Effect of Porous Structure on Fluorination of Graphene Based Materials with Large Specific Surface Area at Mild Condition. *Carbon N. Y.* **2017**, *124*, 288–295. https://doi.org/10.1016/j.carbon.2017.08.076.

(17) Kim, Y. H.; Park, J. S.; Choi, Y. R.; Park, S. Y.; Lee, S. Y.; Sohn, W.; Shim, Y. S.; Lee, J. H.; Park, C. R.; Choi, Y. S.; Hong, B. H.; Lee, J. H.; Lee, W. H.; Lee, D.; Jang, H. W. Chemically Fluorinated Graphene Oxide for Room Temperature Ammonia Detection at Ppb Levels. *J. Mater. Chem. A* **2017**, *5* (36), 19116–19125. https://doi.org/10.1039/c7ta05766k.

(18) Hsieh, Y. L.; Su, W. H.; Huang, C. C.; Su, C. Y. In Situ Cleaning and Fluorination of Black Phosphorus for Enhanced Performance of Transistors with High Stability. *ACS Appl. Mater. Interfaces* **2020**, *12* (33), 37375–37383. https://doi.org/10.1021/acsami.0c11129.

(19) Ma, F.; Sun, C.; Shao, Y.; Wu, Y.; Huang, B.; Hao, X. One-Step Exfoliation and Fluorination of g-C_3N_4 Nanosheets with Enhanced Photocatalytic Activities. *New J. Chem.* **2017**, *41* (8), 3061–3067. https://doi.org/10.1039/c7nj00035a.

(20) Mayorga-Martinez, C. C.; Sofer, Z.; Sedmidubský, D.; Huber, Š.; Eng, A. Y. S.; Pumera, M. Layered Metal Thiophosphite Materials: Magnetic, Electrochemical, and Electronic Properties. *ACS Appl. Mater. Interfaces* **2017**, *9* (14), 12563–12573. https://doi.org/10.1021/acsami.6b16553.

(21) Gusmão, R.; Sofer, Z.; Sedmidubský, D.; Huber, Š.; Pumera, M. The Role of the Metal Element in Layered Metal Phosphorus Triselenides upon Their Electrochemical Sensing and Energy Applications. *ACS Catal.* **2017**, *7* (12), 8159–8170. https://doi.org/10.1021/acscatal.7b02134.

(22) Sen, P.; Alam, K.; Das, T.; Banerjee, R.; Chakraborty, S. Combinatorial Design and Computational Screening of Two-Dimensional Transition Metal Trichalcogenide Monolayers: Toward Efficient Catalysts for Hydrogen Evolution Reaction. *J. Phys. Chem. Lett.* **2020**, *11* (9), 3192–3197. https://doi.org/10.1021/acs.jpclett.0c00710.

(23) Mukherjee, D.; Austeria, P. M.; Sampath, S. Two-Dimensional, Few-Layer Phosphochalcogenide, $FePS_3$: A New Catalyst for Electrochemical Hydrogen Evolution over Wide PH Range. *ACS Energy Lett.* **2016**, *1* (2), 367–372. https://doi.org/10.1021/acsenergylett.6b00184.

(24) Shifa, T. A.; Wang, F.; Cheng, Z.; He, P.; Liu, Y.; Jiang, C.; Wang, Z.; He, J. High Crystal Quality 2D Manganese Phosphorus Trichalcogenide Nanosheets and Their Photocatalytic Activity. *Adv. Funct. Mater.* **2018**, *28* (18), 1–8. https://doi.org/10.1002/adfm.201800548.

(25) Susner, M. A.; Chyasnavichyus, M.; McGuire, M. A.; Ganesh, P.; Maksymovych, P. Metal Thio- and Selenophosphates as Multifunctional van Der Waals Layered Materials. *Adv. Mater.* **2017**, *29* (38), 1–39. https://doi.org/10.1002/adma.201602852.

(26) Goossens, D. J.; Brazier-Hollins, S.; James, D. R.; Hutchison, W. D.; Hester, J. R. Magnetic Structure and Glassiness in $Fe_{0.5}Ni_{0.5}PS_3$. *J. Magn. Magn. Mater.* **2013**, *334*, 82–86. https://doi.org/10.1016/j.jmmm.2013.01.023.

(27) Long, G.; Zhang, T.; Cai, X.; Hu, J.; Cho, C. W.; Xu, S.; Shen, J.; Wu, Z.; Han, T.; Lin,

J.; Wang, J.; Cai, Y.; Lortz, R.; Mao, Z.; Wang, N. Isolation and Characterization of Few-Layer Manganese Thiophosphite. *ACS Nano* **2017**, *11* (11), 11330–11336. https://doi.org/10.1021/acsnano.7b05856.

(28) Masubuchi, T.; Hoya, H.; Watanabe, T.; Takahashi, Y.; Ban, S.; Ohkubo, N.; Takase, K.; Takano, Y. Phase Diagram, Magnetic Properties and Specific Heat of $Mn_{1-x}Fe_xPS_3$. *J. Alloys Compd.* **2008**, *460* (1–2), 668–674. https://doi.org/10.1016/j.jallcom.2007.06.063.

(29) Wang, F.; Shifa, T. A.; Yu, P.; He, P.; Liu, Y.; Wang, F.; Wang, Z.; Zhan, X.; Lou, X.; Xia, F.; He, J. New Frontiers on van Der Waals Layered Metal Phosphorous Trichalcogenides. *Adv. Funct. Mater.* **2018**, *28* (37), 1–24. https://doi.org/10.1002/adfm.201802151.

(30) Kumar, R.; Jenjeti, R. N.; Austeria, M. P.; Sampath, S. Bulk and Few-Layer $MnPS_3$: A New Candidate for Field Effect Transistors and UV Photodetectors. *J. Mater. Chem. C* **2019**, *7* (2), 324–329. https://doi.org/10.1039/c8tc05011b.

(31) VahidMohammadi, A.; Rosen, J.; Gogotsi, Y. The World of Two-Dimensional Carbides and Nitrides (MXenes). *Science* **2021**, *372* (6547), eabf1581. https://doi.org/10.1126/science.abf1581.

(32) Naguib, M.; Mashtalir, O.; Carle, J.; Presser, V.; Lu, J.; Hultman, L.; Gogotsi, Y.; Barsoum, M. W. Two-Dimensional Transition Metal Carbides. *ACS Nano* **2012**, *6* (2), 1322–1331. https://doi.org/10.1021/nn204153h.

(33) Lei, J. C.; Zhang, X.; Zhou, Z. Recent Advances in MXene: Preparation, Properties, and Applications. *Front. Phys.* **2015**, *10* (3), 276–286. https://doi.org/10.1007/s11467-015-0493-x.

(34) Sokol, M.; Natu, V.; Kota, S.; Barsoum, M. W. On the Chemical Diversity of the MAX Phases. *Trends Chem.* **2019**, *1* (2), 210–223. https://doi.org/10.1016/j.trechm.2019.02.016.

(35) Rosli, N. F.; Nasir, M. Z. M.; Antonatos, N.; Sofer, Z.; Dash, A.; Gonzalez-Julian, J.; Fisher, A. C.; Webster, R. D.; Pumera, M. MAX and MAB Phases: Two-Dimensional Layered Carbide and Boride Nanomaterials for Electrochemical Applications. *ACS Appl. Nano Mater.* **2019**, 6010–6021. https://doi.org/10.1021/acsanm.9b01526.

(36) Malaki, M.; Maleki, A.; Varma, R. S. MXenes and Ultrasonication. *J. Mater. Chem. A* **2019**, *7* (18), 10843–10857. https://doi.org/10.1039/c9ta01850f.

(37) Cheng, Y.; Wang, L.; Song, Y.; Zhang, Y. Deep Insights into the Exfoliation Properties of MAX to MXenes and the Hydrogen Evolution Performances of 2D MXenes. *J. Mater. Chem. A* **2019**, *7* (26), 15862–15870. https://doi.org/10.1039/c9ta03859k.

(38) MacDonald, E.; Wicker, R. Multiprocess 3D Printing for Increasing Component Functionality. *Science* **2016**, *353* (6307), aaf2093.

(39) Gebhardt, A. Understanding Additive Manufacturing; Gebhardt, A. B. T.-U. A. M., Ed.; Hanser, 2011; pp I–IX. https://doi.org/https://doi.org/10.3139/9783446431621.fm.

(40) Davim, J. P. Machining: Fundamentals and Recent Advances. **2008**.

(41) Salvo, P.; Raedt, R.; Carrette, E.; Schaubroeck, D.; Vanfleteren, J.; Cardon, L. A 3D Printed Dry Electrode for ECG/EEG Recording. *Sensors Actuators A Phys.* **2012**, *174*, 96–102. https://doi.org/https://doi.org/10.1016/j.sna.2011.12.017.

(42) Wei, X.; Li, D.; Jiang, W.; Gu, Z.; Wang, X.; Zhang, Z.; Sun, Z. 3D Printable Graphene Composite. *Sci. Rep.* **2015**, *5* (1), 11181. https://doi.org/10.1038/srep11181.

(43) Chisholm, G.; Kitson, P. J.; Kirkaldy, N. D.; Bloor, L. G.; Cronin, L. 3D Printed Flow Plates for the Electrolysis of Water: An Economic and Adaptable Approach to Device Manufacture. *Energy Environ. Sci.* **2014**, *7* (9), 3026–3032. https://doi.org/10.1039/C4EE01426J.

(44) Izumi, A.; Sanada, M.; Furuichi, K.; Teraki, K.; Matsuda, T.; Hiramatsu, K.; Munakata, H.; Kanamura, K. Development of High Capacity Lithium-Ion Battery Applying Three-Dimensionally Patterned Electrode. *Electrochim. Acta* **2012**, *79*, 218–222. https://doi.org/https://doi.org/10.1016/j.electacta.2012.07.001.

(45) *Solar Hydrogen Generation - Toward a Renewable Energy Future*; Licht, S., McConnell, R., Rajeshwar, K., Eds.; Springer US, 2008; Vol. 15.

(46) IEA. The Future of Hydrogen for G20. Seizing Today's Opportunities. *Rep. Prep. by IEA G20, Japan* **2019**, *6* (June), 246–256.

(47) Cavaliere, P. Fundamentals of Water Electrolysis BT - Water Electrolysis for Hydrogen Production; Cavaliere, P., Ed.; Springer International Publishing: Cham, 2023; pp 1–60. https://doi.org/10.1007/978-3-031-37780-8_1.

(48) Zeng, M.; Li, Y. Recent Advances in Heterogeneous Electrocatalysts for the Hydrogen Evolution Reaction. *J. Mater. Chem. A* **2015**, *3* (29), 14942–14962. https://doi.org/10.1039/c5ta02974k.

(49) Morales-Guio, C. G.; Stern, L. A.; Hu, X. Nanostructured Hydrotreating Catalysts for Electrochemical Hydrogen Evolution. *Chem. Soc. Rev.* **2014**, *43* (18), 6555–6569. https://doi.org/10.1039/c3cs60468c.

(50) Brett, C. *Fundamentals of Electrochemistry*; 2008. https://doi.org/10.1007/978-3-540-77508-9_8.

(51) Zhebo Chen Eric Miller; Dinh, H. N. *Photoelectrochemical Water Splitting: Standards, Experimental Methods, and Protocols*; 2013.

(52) Hisatomi, T.; Kubota, J.; Domen, K. Recent Advances in Semiconductors for Photocatalytic and Photoelectrochemical Water Splitting. *Chem. Soc. Rev.* **2014**, *43* (22), 7520–7535. https://doi.org/10.1039/c3cs60378d.

(53) Yu, X.; Prévot, M. S.; Guijarro, N.; Sivula, K. Self-Assembled 2D WSe2 Thin Films for Photoelectrochemical Hydrogen Production. *Nat. Commun.* **2015**, *6* (1), 7596. https://doi.org/10.1038/ncomms8596.

(54) Koumi Ngoh, S.; Njomo, D. An Overview of Hydrogen Gas Production from Solar Energy. *Renew. Sustain. Energy Rev.* **2012**, *16* (9), 6782–6792. https://doi.org/10.1016/j.rser.2012.07.027.

(55) Van De Krol, R.; Liang, Y.; Schoonman, J. Solar Hydrogen Production with Nanostructured Metal Oxides. *J. Mater. Chem.* **2008**, *18* (20), 2311–2320. https://doi.org/10.1039/b718969a.

(56) Li, F.; Fan, K.; Xu, B.; Gabrielsson, E.; Daniel, Q.; Li, L.; Sun, L. Organic Dye-Sensitized Tandem Photoelectrochemical Cell for Light Driven Total Water Splitting. *J. Am. Chem. Soc.* **2015**, *137* (28), 9153–9159. https://doi.org/10.1021/jacs.5b04856.

(57) Geim, A. K.; Novoselov, K. S. The Rise of Graphene. *Nat. Mater.* **2007**, *6* (3), 183–191. https://doi.org/10.1038/nmat1849.

(58) Huang, C.; Li, C.; Shi, G. Graphene Based Catalysts. *Energy Environ. Sci.* **2012**, *5* (10), 8848–8868. https://doi.org/10.1039/C2EE22238H.

(59) Hinnemann, B.; Moses, P. G.; Bonde, J.; Jørgensen, K. P.; Nielsen, J. H.; Horch, S.;

Chorkendorff, I.; Nørskov, J. K. Biomimetic Hydrogen Evolution: MoS_2 Nanoparticles as Catalyst for Hydrogen Evolution. *J. Am. Chem. Soc.* **2005**, *127* (15), 5308–5309. https://doi.org/10.1021/ja0504690.

(60) Yin, Y.; Han, J.; Zhang, Y.; Zhang, X.; Xu, P.; Yuan, Q.; Samad, L.; Wang, X.; Wang, Y.; Zhang, Z.; Zhang, P.; Cao, X.; Song, B.; Jin, S. Contributions of Phase, Sulfur Vacancies, and Edges to the Hydrogen Evolution Reaction Catalytic Activity of Porous Molybdenum Disulfide Nanosheets. *J. Am. Chem. Soc.* **2016**, *138* (25), 7965–7972. https://doi.org/10.1021/jacs.6b03714.

(61) Kong, D.; Wang, H.; Cha, J. J.; Pasta, M.; Koski, K. J.; Yao, J.; Cui, Y. Synthesis of MoS2 and MoSe2 Films with Vertically Aligned Layers. *Nano Lett.* **2013**, *13* (3), 1341–1347. https://doi.org/10.1021/nl400258t.

(62) Li, G.; Zhang, D.; Qiao, Q.; Yu, Y.; Peterson, D.; Zafar, A.; Kumar, R.; Curtarolo, S.; Hunte, F.; Shannon, S.; Zhu, Y.; Yang, W.; Cao, L. All The Catalytic Active Sites of MoS2 for Hydrogen Evolution. *J. Am. Chem. Soc.* **2016**, *138* (51), 16632–16638. https://doi.org/10.1021/jacs.6b05940.

(63) Voiry, D.; Salehi, M.; Silva, R.; Fujita, T.; Chen, M.; Asefa, T.; Shenoy, V. B.; Eda, G.; Chhowalla, M. Conducting MoS2 Nanosheets as Catalysts for Hydrogen Evolution Reaction. *Nano Lett.* **2013**, *13* (12), 6222–6227. https://doi.org/10.1021/nl403661s.

(64) Lukowski, M. A.; Daniel, A. S.; Meng, F.; Forticaux, A.; Li, L.; Jin, S. Enhanced Hydrogen Evolution Catalysis from Chemically Exfoliated Metallic MoS2 Nanosheets. *J. Am. Chem. Soc.* **2013**, *135* (28), 10274–10277. https://doi.org/10.1021/ja404523s.

(65) Tang, Q.; Jiang, D. Mechanism of Hydrogen Evolution Reaction on 1T-MoS2 from First Principles. *ACS Catal.* **2016**, *6* (8), 4953–4961.

https://doi.org/10.1021/acscatal.6b01211.

(66) M. C. Friedel. No Title. *Compt. Rend.* **1894**, *119* (260).

(67) Mukherjee, D.; Muthu Austeria, P.; Sampath, S. Few-Layer Iron Selenophosphate, FePSe3: Efficient Electrocatalyst toward Water Splitting and Oxygen Reduction Reactions. *ACS Appl. Energy Mater.* **2018**, *1* (1), 220–231. https://doi.org/10.1021/acsaem.7b00101.

(68) Li, K.; Rakov, D.; Zhang, W.; Xu, P. Improving the Intrinsic Electrocatalytic Hydrogen Evolution Activity of Few-Layer NiPS3 by Cobalt Doping. *Chem. Commun.* **2017**, *53* (58), 8199–8202. https://doi.org/10.1039/c7cc03173d.

(69) Barsoum, M. W. The MN+1AXN Phases: A New Class of Solids. *Prog. Solid State Chem.* **2000**, *28* (1–4), 201–281. https://doi.org/10.1016/s0079-6786(00)00006-6.

(70) Nowotny, V. H. Strukturchemie Einiger Verbindungen Der Übergangsmetalle Mit Den Elementen C, Si, Ge, Sn. *Prog. Solid State Chem.* **1971**, *5* (C), 27–70. https://doi.org/10.1016/0079-6786(71)90016-1.

(71) Nowotny, H.; Rogl, P.; Schuster, J. C. Structural Chemistry of Complex Carbides and Related Compounds. *J. Solid State Chem.* **1982**, *44* (1), 126–133. https://doi.org/10.1016/0022-4596(82)90409-1.

(72) Barsoum, M. W.; El-raghy, T. Synthesis and Characterization of a Remarkable Ceramic: Ti_3SiC_2. J. Am. Ceram. Soc. 1996, pp 1953–1956.

(73) Barsoum, M. W.; Brodkin, D.; El-raghy, T. 1-S2.0-S1359646296004186-Main.Pdf. *Scr. Mater.* **1997**, *36* (5), 535–541.

(74) Sun, Z.; Music, D.; Ahuja, R.; Li, S.; Schneider, J. M. Bonding and Classification of

Nanolayered Ternary Carbides. *Phys. Rev. B - Condens. Matter Mater. Phys.* **2004**, *70* (9), 1–3. https://doi.org/10.1103/PhysRevB.70.092102.

(75) Chen, K.; Qiu, N.; Deng, Q.; Kang, M. H.; Yang, H.; Baek, J. U.; Koh, Y. H.; Du, S.; Huang, Q.; Kim, H. E. Cytocompatibility of Ti_3AlC_2, Ti_3SiC_2, and Ti_2AlN: In Vitro Tests and First-Principles Calculations. *ACS Biomater. Sci. Eng.* **2017**, *3* (10), 2293–2301. https://doi.org/10.1021/acsbiomaterials.7b00432.

(76) Akshay Kumar, K. P.; Alduhaish, O.; Pumera, M. Electrocatalytic Activity of Layered MAX Phases for the Hydrogen Evolution Reaction. *Electrochem. Commun.* **2021**, *125* (January), 106977. https://doi.org/10.1016/j.elecom.2021.106977.

(77) Anasori, B.; Xie, Y.; Beidaghi, M.; Lu, J.; Hosler, B. C.; Hultman, L.; Kent, P. R. C.; Gogotsi, Y.; Barsoum, M. W. Two-Dimensional, Ordered, Double Transition Metals Carbides (MXenes). *ACS Nano* **2015**, *9* (10), 9507–9516. https://doi.org/10.1021/acsnano.5b03591.

(78) Novčić, K. A.; Iffelsberger, C.; Pumera, M. Layered MAX Phase Electrocatalyst Activity Is Driven by Only a Few Hot Spots. *J. Mater. Chem. A* **2022**, *10* (6), 3206–3215. https://doi.org/10.1039/d1ta06419c.

(79) Magnuson, M.; Mattesini, M. Chemical Bonding and Electronic-Structure in MAX Phases as Viewed by X-Ray Spectroscopy and Density Functional Theory. *Thin Solid Films* **2017**, *621*, 108–130. https://doi.org/https://doi.org/10.1016/j.tsf.2016.11.005.

(80) Shah, A. K.; Sahu, T. K.; Banik, A.; Gogoi, D.; Peela, N. R.; Qureshi, M. Reduced Graphene Oxide Modified CuBi2O4 as an Efficient and Noble Metal Free Photocathode for Superior Photoelectrochemical Hydrogen Production. *Sustain. Energy Fuels* **2019**, *3* (6), 1554–1561. https://doi.org/10.1039/C9SE00129H.

(81) Sim, U.; Moon, J.; An, J.; Kang, J. H.; Jerng, S. E.; Moon, J.; Cho, S.-P.; Hong, B. H.; Nam, K. T. N-Doped Graphene Quantum Sheets on Silicon Nanowire Photocathodes for Hydrogen Production. *Energy Environ. Sci.* **2015**, *8* (4), 1329–1338. https://doi.org/10.1039/C4EE03607G.

(82) Oh, S.; Kim, J. B.; Song, J. T.; Oh, J.; Kim, S.-H. Atomic Layer Deposited Molybdenum Disulfide on Si Photocathodes for Highly Efficient Photoelectrochemical Water Reduction Reaction. *J. Mater. Chem. A* **2017**, *5* (7), 3304–3310. https://doi.org/10.1039/C6TA10707A.

(83) Dong, Y.; Chen, Y.; Jiang, P.; Wang, G.; Wu, X.; Wu, R.; Zhang, C. Efficient and Stable MoS2/CdSe/NiO Photocathode for Photoelectrochemical Hydrogen Generation from Water. *Chem. - An Asian J.* **2015**, *10* (8), 1660–1667. https://doi.org/10.1002/asia.201500374.

(84) Ambrosi, A.; Pumera, M. 3D-Printing Technologies for Electrochemical Applications. *Chem. Soc. Rev.* **2016**, *45* (10), 2740–2755. https://doi.org/10.1039/C5CS00714C.

(85) Ritala, M. *Atomic Layer Deposition*; 2003; Vol. 1. https://doi.org/10.1002/vipr.201200502.

(86) George, S. M. Atomic Layer Deposition: An Overview. *Chem. Rev.* **2010**, *110* (1), 111–131. https://doi.org/10.1021/cr900056b.

(87) Kubelka, P.; Munk, F. An Article on Optics of Paint Layers. *Z. Tech. Phys.* **1931**, *12* (1930), 593–601.

(88) Tauc, J. Optical Properties and Electronic Structure of Amorphous Ge and Si. *Mat. Res. Bull.* **1968**, *3* (1), 37–46.

(89) Makuła, P.; Pacia, M.; Macyk, W. How To Correctly Determine the Band Gap Energy of Modified Semiconductor Photocatalysts Based on UV-Vis Spectra. *J. Phys. Chem. Lett.* **2018**, *9* (23), 6814–6817. https://doi.org/10.1021/acs.jpclett.8b02892.

(90) Kahlert, H. Reference Electrodes BT - Electroanalytical Methods: Guide to Experiments and Applications; Scholz, F., Bond, A. M., Compton, R. G., Fiedler, D. A., Inzelt, G., Kahlert, H., Komorsky-Lovrić, Š., Lohse, H., Lovrić, M., Marken, F., Neudeck, A., Retter, U., Scholz, F., Stojek, Z., Eds.; Springer Berlin Heidelberg: Berlin, Heidelberg, 2010; pp 291–308. https://doi.org/10.1007/978-3-642-02915-8_15.

(91) Myhra, S.; Crossley, J. A. A.; Barsoum, M. W. Crystal-Chemistry of the Ti_3AlC_2 and Ti_4AlN_3 Layered Carbide/Nitride Phases - Characterization by XPS. *J. Phys. Chem. Solids* **2001**, *62* (4), 811–817. https://doi.org/10.1016/S0022-3697(00)00268-7.

(92) Khaledialidusti, R.; Khazaei, M.; Khazaei, S.; Ohno, K. High-Throughput Computational Discovery of Ternary-Layered MAX Phases and Prediction of Their Exfoliation for Formation of 2D MXenes. *Nanoscale* **2021**, *13* (15), 7294–7307. https://doi.org/10.1039/d0nr08791b.